

**INFLUENCE OF HYDROGENATED AMORPHOUS CARBON
UNDERLAYER FILM ON THE FORMATION OF
CARBON NITRIDE NANOSTRUCTURES**

NOOR HAMIZAH BINTI KHANIS

**DISSERTATION SUBMITTED IN FULFILLMENT OF
THE REQUIREMENTS FOR THE DEGREE OF
MASTER OF SCIENCE**

**DEPARTMENT OF PHYSICS
FACULTY OF SCIENCE
UNIVERSITY OF MALAYA
KUALA LUMPUR**

2013

UNIVERSITI MALAYA

ORIGINAL LITERARY WORK DECLARATION

Name of Candidate: NOOR HAMIZAH BINTI KHANIS (I.C/Passport No: 860104-085206)

Registration/Matric No: SGR090097

Name of Degree: MASTER OF SCIENCE (DISSERTATION)

Title of Project Paper/Research Report/Dissertation/Thesis ("this Work"):

INFLUENCE OF HYDROGENATED AMORPHOUS CARBON UNDERLAYER FILM ON
THE FORMATION OF CARBON NITRIDE NANOSTRUCTURES

Field of Study: THIN FILMS

I do solemnly and sincerely declare that:

- (1) I am the sole author/writer of this Work;
- (2) This Work is original;
- (3) Any use of any work in which copyright exists was done by way of fair dealing and for permitted purposes and any excerpt or extract from, or reference to or reproduction of any copyright work has been disclosed expressly and sufficiently and the title of the Work and its authorship have been acknowledged in this Work;
- (4) I do not have any actual knowledge nor do I ought reasonably to know that the making of this work constitutes an infringement of any copyright work;
- (5) I hereby assign all and every rights in the copyright to this Work to the University of Malaya ("UM"), who henceforth shall be owner of the copyright in this Work and that any reproduction or use in any form or by any means whatsoever is prohibited without the written consent of UM having been first had and obtained;
- (6) I am fully aware that if in the course of making this Work I have infringed any copyright whether intentionally or otherwise, I may be subject to legal action or any other action as may be determined by UM.

Candidate's Signature:

Date:

Subscribed and solemnly declared before,

Witness's Signature:

Date:

Name:

Designation:

Abstract

This study is focused on the effects of the structural properties of the hydrogenated amorphous carbon (a-C:H) underlayer on the subsequent formation of carbon nitride nanostructures (ns-CN_x). Both layers were prepared sequentially using radio-frequency plasma enhanced chemical vapour deposition (RFPECVD). The a-C:H underlayers and ns-CN_x were deposited from pure methane and a mixture of pure methane and nitrogen gases, respectively. The deposition parameters of the ns-CN_x were fixed while the parameters relating to the deposition of a-C:H underlayers were varied. Three sets of ns-CN_x deposited using fixed deposition parameters on a-C:H underlayer were studied. The first two sets of ns-CN_x samples were deposited on a-C:H underlayers grown at different deposition time duration and RF power. The H₂ plasma treatment time duration done on a-C:H underlayers were varied for the third set of ns-CN_x samples. The structural properties of the a-C:H underlayers studied were characterized using atomic force microscopy (AFM), Fourier transform infrared spectroscopy (FTIR) and Raman spectroscopy while the structural properties of ns-CN_x samples were characterized using field emission scanning electron microscopy (FESEM), FTIR spectroscopy, Raman spectroscopy and Auger electron spectroscopy.

It was determined that the a-C:H underlayer with highest surface roughness of 6 nm results in the formation of rigid vertically aligned CN_x nanorods. The a-C:H underlayer with highest surface roughness which induced the formation of cone-like structures was shown to have an ordered structure of sp² clusters and the optimized deposition time duration for the growth of the underlayer was established to be 10 minutes. By varying the applied RF power at 30-80 W, ion bombardment was shown to play an important role in changing the surface morphology of a-C:H underlayer. From the FTIR analysis, the a-C:H underlayer with highest surface roughness shows low CH_n band associated with low H content, and dominant sp² clustering. These properties induced the formation of the said rigid vertically aligned CN_x nanorods. It was also found that by tuning the RF power, unique flower-like ns-CN_x structure was formed. The treatment of H₂ plasma at different time at 3, 5 and 10 minutes on these a-C:H underlayers showed that H bombardment could be used effectively to modify the surface morphology of the underlayer films. In contrast to the high surface roughness requirement for the growth of nanorods, CN_x nanotips were formed on smooth a-C:H underlayer film surface.

These results showed the effects of changes in structural properties of a-C:H underlayers on the formation of different ns-CN_x. The ns-CN_x formed were rigid vertically aligned nanorods, nanotip and the rare flower-like structures. Both layers were able to be fabricated in the same system at low deposition temperature of 100 °C without the use of catalyst. High N content and preferential formation of -N≡C bonds are crucial aspects in the formation of rigid and vertically aligned nanorods.

Abstrak

Kajian ini ditumpukan kepada kesan sifat struktur filem nipis amorfus karbon berhidrogen (a-C:H) yang digunakan sebagai substrat dasar bagi pembentukan karbon nitrida bernanostruktur (ns-CN_x). Kedua-dua lapisan ini dihasilkan berturutan menggunakan pemendapan frekuensi radio wap kimia secara peningkatan plasma (RFPECVD). Lapisan dasar a-C:H dan berikutnya ns-CN_x, masing-masing dimendapkan daripada metana tulen dan campuran gas metana tulen dan nitrogen. Parameter bagi pemendapan ns-CN_x ditetapkan manakala bagi lapisan a-C:H, parameter yang digunakan diubah. Tiga set ns-CN_x yang dimendapkan menggunakan parameter pemendapan yang tetap dimendapkan di atas lapisan dasar a-C:H telah dikaji. Dua set pertama terdiri dari sampel ns-CN_x yang dimendapkan di atas lapisan dasar a-C:H yang dimendapkan pada tempoh masa dan kuasa RF yang berbeza-beza. Lapisan dasar a-C:H yang dirawat dalam plasma H₂ pada tempoh masa berbeza-beza digunakan sebagai lapisan dasar untuk sampel ns-CN_x bagi set ketiga. Sifat struktur bagi lapisan dasar a-C:H telah dikaji menggunakan mikroskopi daya atom (AFM), spektroskop inframerah transformasi Fourier (FTIR) dan spektroskopi Raman manakala sifat struktur bagi ns-CN_x dikaji menggunakan mikroskopi pancaran medan pengimbasan elektron (FESEM), spektroskopi FTIR dan spektroskopi elektron Auger.

Lapisan dasar yang mempunyai kekasaran permukaan yang paling tinggi iaitu 6 nm menyebabkan pembentukan CN_x rod-nano yang tegar dan secara menegak. Kekasaran permukaan lapisan dasar a-C:H yang tinggi mendorong pembentukan struktur menyerupai kon yang mengandungi kelompok sp² yang tertib dan ini dioptimumkan pada tempoh pemendapan lapisan dasar sebanyak 10 minit. Dengan mengubah kuasa frekuensi radio (RF) yang dikenakan daripada 30-80 W, hentaman ion memainkan peranan penting dalam mengubah morfologi permukaan lapisan dasar a-C:H. Daripada analisis FTIR, lapisan dasar a-C:H yang mempunyai kekasaran paling tinggi menunjukkan jalur CH_n yang rendah yang dikaitkan dengan kandungan H rendah, dan pengkelompokan sp². Sifat-sifat yang dominan ini mendorong pembentukan rod-nano CN_x yang tegar dan menjajar secara menegak. Pembentukan struktur unik menyerupai bunga juga diperolehi dengan mengubah kuasa RF. Rawatan plasma H₂ pada 3, 5 dan 10 minit ke atas lapisan dasar a-C:H menunjukkan bahawa hentaman H₂ boleh digunakan secara berkesan dalam mengubah morfologi permukaan lapisan filem dasar. Berbeza dengan rod-nano yang memerlukan permukaan yang kasar, tip-nano CN_x telah dihasilkan di atas lapisan dasar a-C:H yang rata.

Keputusan ini menunjukkan kesan perubahan dalam sifat struktur lapisan dasar a-C:H berpotensi terhadap pembentukan ns-CN_x yang berbeza. ns-CN_x terbentuk adalah rod-nano yang tegar dan menjajar secara tegak, tip-nano dan struktur menyerupai bunga yang jarang ditemui. Kedua-dua lapisan boleh disediakan dalam sistem yang sama pada suhu yang rendah iaitu 100 °C tanpa penggunaan bahan pemangkin. Kandungan N yang tinggi dan pembentukan -N≡C adalah aspek penting dalam pembentukan rod-nano yang tegar dan menjajar secara tegak.

Acknowledgment

In the name of Allah, Most Gracious, Most Merciful.

All Praise to Allah for His blessing and strength to make completion of this dissertation a reality. I would like to express my sincere gratitude to my supervisor, Associate Professor Dr. Siti Meriam Ab. Gani for valuable guidance and endless support throughout my MSc work. Not forgotten are all the lecturers of Low Dimensional Materials Research Centre, especially to Professor Datin Dr. Saadah Abd. Rahman for her constructive advice and guidance. I would also like to thank the science officer, Pn. Zurina Marzuki, the assistant science officers Pn. Norlela Mohamed Shahardin and En. Mohamad Aruf; and all members of the Physics Department for their kindness.

Million thanks to Dr. Richard Ritikos for endless guidance, supportive comment and encouragement during my MSc work. I would like to express my appreciation to my colleagues Ms. Maisara Othman and Ms. Nur Maisarah Abdul Rashid for being kind and supportive and going through this hardship together. My gratitude also goes to Siti Hajar, Nor Khairiah, Mohd. Ragib, Chong Su Kong, Chan Kee Wah, Dr Goh Boon Tong and all the members of Low Dimensional Materials Research Centre.

I would like to thank University of Malaya for SBUM scholarship scheme to support my MSc. I would also like to acknowledge the financial support given, including University Research Grant RG064-09AFR, Fundamental Research Grants FP016/2008C and FP052/2010B and short term grant PS308/2009C.

Last but not least, my deepest gratitude to my families (in-laws included) especially to my beloved parents Tn. Hj. Khanis Khayon and Pn. Hjh. Homsinah Mohamad for the love, support and endless prayers. My gratitude also goes to my sibling Noor Rashidah and Nadzri Amini. My special thanks also to my beloved husband, Fakrul Hakimi Osman for his understanding, care and love.

To those who indirectly contribute to this work, your kindness means a lot to me.

Thank you.

Table of Content

Abstract	ii
Abstrak	iii
Acknowledgment	iv
Table of Content	v
LIST OF FIGURES	ix
LIST OF TABLES	xiv
LIST OF PUBLICATIONS	xv
LIST OF ABBREVIATIONS	xvi
CHAPTER 1: INTRODUCTION	1
1.1 Development on Carbon Nitride	1
1.2 Properties of Carbon Nitride and Application	3
1.3 Related Works, Motivation and Objectives for This Study	4
1.4 Thesis Outline	6
CHAPTER 2: LITERATURE REVIEW	8
2.1 Introduction	8
2.2 Carbon Nitride Nanostructures	8
2.2.1 Nanorods.....	8
2.2.2 Nanotubes.....	9
2.2.3 Nanotips.....	10
2.2.4 Other ns-CN _x	11
2.3 Review on Preparation of Carbon Nitride Nanostructures	15
2.3.1 Sputtering.....	16
2.3.2 Arc Discharge.....	17

2.3.3	Laser Ablation.....	18
2.3.4	Chemical Vapour Deposition.....	19
2.3.4.1	Hot filament plasma enhanced CVD.....	19
2.3.4.2	Electron cyclotron resonance CVD.....	20
2.3.4.3	Radio frequency plasma enhanced CVD.....	21
2.3.4.4	Microwave plasma CVD.....	22
2.3.4.5	Floating catalyst CVD.....	23
2.4	Substrate Condition.....	24
2.4.1	Bare Substrate.....	24
2.4.2	Catalyst.....	25
2.4.3	Template and Underlayer.....	26
2.5	Review of Analytical Methods.....	27
2.5.1	Fourier Transform Infrared Spectroscopy.....	27
2.5.2	Raman Spectroscopy.....	31
CHAPTER 3:	EXPERIMENTAL AND ANALYTICAL TECHNIQUES.....	34
3.1	Introduction.....	34
3.2	Radio Frequency Plasma Enhanced Chemical Vapour Deposition System.....	34
3.3	Sample Preparation.....	38
3.3.1	Substrate Cleaning Procedures.....	38
3.3.2	Pre-deposition Process.....	38
3.3.3	Deposition Process.....	40
3.3.4	Post-deposition Process.....	44
3.4	Analytical Technique.....	44
3.4.1	Atomic Force Microscopy.....	44
3.4.2	Profilometer.....	47
3.4.3	Scanning Electron Microscopy.....	48

3.4.4	Fourier Transmission Infrared Spectroscopy Measurement.....	50
3.4.5	Raman Spectroscopy.....	56
3.4.6	Auger Electron Spectroscopy.....	58
CHAPTER 4: EFFECTS OF HYDROGENATED AMORPHOUS CARBON UNDERLAYER ON THE FORMATION OF CARBON NITRIDE NANOSTRUCTURES: RESULTS, ANALYSIS AND DISCUSSION.....		
	4.1 Introduction.....	61
	4.2 Effects of Deposition Time Duration of a-C:H Underlayer and Resulting CN_x/ a-C:H Formation.....	64
4.2.1	Effects of Deposition Time Duration on a-C:H Underlayers.....	64
4.2.1.1	Growth rate of a-C:H underlayers.....	64
4.2.1.2	Surface roughness and surface morphology of a-C:H underlayers.....	66
4.2.1.3	Chemical bonding properties of a-C:H underlayers.....	68
4.2.1.4	Raman Analysis.....	72
4.2.2	Effect on Resulting ns-CN _x /a-C:H Formation.....	76
4.2.2.1	Surface and cross-sectional images.....	76
4.2.2.2	Auger electron spectroscopy measurement of ns-CN _x	79
4.2.2.3	FTIR spectra of ns-CN _x	80
4.2.3	Summary.....	85
	4.3 Effects of RF Power on a-C:H Underlayer and Resulting CN_x/a-C:H Formation.....	86
4.3.1	Effects of RF Power on a-C:H Underlayer.....	86
4.3.1.1	Growth rate of a-C:H underlayers.....	86
4.3.1.2	Surface roughness and surface morphology of a-C:H underlayers.....	87
4.3.1.3	FTIR spectra of a-C:H underlayers.....	90
4.3.1.4	Raman scattering analysis.....	92
4.3.2	Effect of RF Power on Resulting CN _x /a-C:H Formation.....	97
4.3.2.1	Surface and cross-sectional images.....	97

4.3.2.2	Auger electron spectroscopy measurement of CN_x nanostructures.....	100
4.3.2.3	FTIR spectra of CN_x nanostructures.....	102
4.3.3	Summary.....	107
4.4	Effects of Hydrogen Treatment on the a-C:H Underlayer and the Resulting CN_x/ a-C:H Film.....	108
4.4.1	Effect of H_2 Treatment Time Duration on a-C:H Underlayers.....	109
4.4.1.1	Surface roughness and surface morphology of a-C:H underlayers.....	109
4.4.1.2	Chemical bonding properties of a-C:H underlayers.....	111
4.4.1.3	Raman analysis.....	114
4.4.2	Effect on Resulting CN_x /a-C:H Formation.....	119
4.4.2.1	Surface and cross-sectional images.....	119
4.4.2.2	Auger electron spectroscopy measurement of ns- CN_x	121
4.4.2.3	FTIR spectra of ns- CN_x	122
4.4.3	Summary.....	127
CHAPTER 5:	CONCLUSION AND FUTURE WORKS.....	129
5.1	Conclusion.....	129
5.2	Future Works.....	131
REFERENCES	132

LIST OF FIGURES

Figure 1.1: Progression chart of ns-CN _x .	2
Figure 2.1: Example of FESEM images CN _x nanorods.	9
Figure 2.2: Example SEM images of various CN _x nanotubes structure.	10
Figure 2.3: FESEM images of CN _x nanotips.	11
Figure 2.4: HRTEM image of CN _x nanobell.	12
Figure 2.5: SEM images of carbon nitride (a) aligned nanoribbons and (b) microsphere nanoribbons.	13
Figure 2.6: TEM image of the CN _x nanospheres.	13
Figure 2.7: SEM image the formation of (a) nano-petals and (b) flower-like CN _x structure.	14
Figure 2.8: The TEM image of CN _x leaf-like structures.	15
Figure 2.9: The example of schematic diagram of magnetron sputtering system.	16
Figure 2.10: Example of schematic diagram of arc discharge system.	17
Figure 2.11: Example of schematic diagram of pulsed laser ablation system.	18
Figure 2.12: Example of schematic diagram of HFPECVD system.	20
Figure 2.13: The example of schematic diagram ECRCVD system.	21
Figure 2.14: The schematic diagram of RFPECVD system.	22
Figure 2.15: Example of schematic diagram of MWPECVD system.	23
Figure 2.16: Example of typical schematic diagram of floating catalyst CVD system.	24
Figure 2.17: The example of template used in CN _x nanotubes fabrication.	26
Figure 2.18: Type of vibration mode in FTIR analysis.	28
Figure 2.19: Example of typical FTIR spectra of a-C:H film.	29
Figure 2.20: Example of typical FTIR spectra of CN _x film.	29
Figure 2.21: Typical Raman spectra for carbon based materials.	32
Figure 3.1: Schematic diagram of RFPECVD system.	35

Figure 3.2: Schematic diagram of RFPECVD system reaction chamber.	37
Figure 3.3: Top view mask of substrate holder.	39
Figure 3.4: Single a-C:H underlayer deposited on Si substrate and CN _x film deposited on a-C:H underlayer prepared by RFPECVD.	40
Figure 3.5: Chart of sample preparation.	42
Figure 3.6: Plasma discharge during deposition process.	43
Figure 3.7: Schematic diagram of AFM.	45
Figure 3.8: VEECO Dimension 3000 atomic force microscope.	45
Figure 3.9: Surface morphological (a) and roughness analysis (b) of a-C:H underlayer deposited by RFPECVD at 10 minutes.	46
Figure 3.10: KLA TENCO P-6 profilometer.	47
Figure 3.11: Data observed from profilometer for film deposited at 100 W RF power with 3 minutes hydrogen treatment process.	48
Figure 3.12: FEI Quanta 200 field emission scanning electron microscope.	49
Figure 3.13: Surface (a) and cross section (b) images of CN _x film deposited on a-C:H underlayer prepared at RF power of 50 W.	50
Figure 3.14: Schematic diagram of Fourier Transform Infrared Spectrometer.	51
Figure 3.15: The Perkin Elmer System 2000 FTIR spectrometer.	52
Figure 3.16: FTIR spectrum of a-C:H underlayer.	53
Figure 3.17: FTIR spectrum of CN _x nanostructures.	53
Figure 3.18: Example of deconvolution FTIR absorption peaks of a-C:H underlayer and CN _x nanostructures in wavenumber region of 2000-2300 cm ⁻¹ .	55
Figure 3.19: The Renishaw inVia Raman Microscope.	56
Figure 3.20: Raman spectra with the baseline (a) and corrected Raman spectra with the Gaussian fitting D and G bands (b)	57
Figure 3.21: Schematic diagram of Auger electron process.	58
Figure 3.22: JAMP-9500F Field Emission Auger Microprobe.	60
Figure 3.23: AES spectra variation of CN _x prepared on different deposition duration of a-C:H underlayer and bare c-Si substrate.	60

Figure 4.1: Summary of the methodology and variations in film preparation parameters	63
Figure 4.2: Thickness (■) and growth rate (◆) of a-C:H underlayer deposited by RFPECVD for different deposition time duration. The line is only an eye-guide.	65
Figure 4.3: AFM surface morphology of (a) bare c-Si, a-C:H underlayers deposited for t_D of (b) 5, (c) 10, (d) 15 and (e) 30 minutes.	66
Figure 4.4: Variation of surface roughness of bare c-Si and a-C:H underlayers deposited at 5, 10, 15 and 30 minutes.	67
Figure 4.5: The FTIR spectra of a-C:H underlayer deposited for varied deposition duration.	68
Figure 4.6: Variation of FTIR spectra for a-C:H underlayers deposited at different duration of 5, 10, 15 and 30 minutes.	71
Figure 4.7: The raw Raman spectra with strong background (a) and the Raman spectra after the background extraction (b) for a-C:H underlayers prepared at different deposition duration of 5, 10, 15 and 30 min.	73
Figure 4.8: Raman analysis of a-C:H underlayers prepared at t_D of 5, 10, 15 and 30 minutes. Line is guide to the eyes.	75
Figure 4.9: Surface and cross-sectional images of ns- CN_x deposited on a-C:H underlayer prepared at different t_D .	76
Figure 4.10: Variation of FESEM cross-sectional images for ns- CN_x deposited on bare c-Si and 10 minutes a-C:H underlayer.	78
Figure 4.11: Variation of nitrogen to carbon N/C ratio of ns- CN_x deposited on c-Si, a-C:H underlayers at t_D of 5, 10, 15 and 30 minutes.	79
Figure 4.12: Variation in FTIR absorbance spectra of ns- CN_x as a function of deposition duration of a-C:H underlayers.	81
Figure 4.13: The FTIR spectra for ns- CN_x deposited at different t_D of a-C:H underlayers in the range of (a) sp^2 , (b) sp^1 and (c) sp^3 phases.	82
Figure 4.14: The FTIR spectra in the wavenumber range of $1900-2300\text{ cm}^{-1}$ of CN_x nanostructures as a function of t_D a-C:H underlayers.	83
Figure 4.15: Gaussian fitting profiles for FTIR spectra in wavenumber region of $2000-2300\text{ cm}^{-1}$ for a-C:H underlayer at t_D 10, 30 minutes and c-Si.	84
Figure 4.16: Growth rate of a-C:H underlayers deposited by RFPECVD at different RF power. The line is only an eye-guide.	87

Figure 4.17: AFM surface morphology of a-C:H underlayers deposited for RF power of 30, 40, 50, 60, 80 and 100 W.	88
Figure 4.18: Variation of surface roughness of a-C:H underlayers deposited at RF power of 30, 40, 50, 60, 80 and 100 W.	89
Figure 4.19: The FTIR spectra of a-C:H underlayer at different RF power of 30, 40, 50, 60, 80 and 100 W.	91
Figure 4.20: Variation of FTIR spectra for a-C:H underlayers deposited at different RF power in the range of 1400-2000 cm^{-1} and 2600-4000 cm^{-1} .	92
Figure 4.21: Raw Raman spectra (a) and corrected Raman spectra (b) of a-C:H underlayers as a function of RF power.	94
Figure 4.22: Raman analysis of a-C:H underlayers prepared at different RF power.	96
Figure 4.23: Surface and cross-section images of ns:CN _x deposited by RFPECVD at different RF power of a-C:H underlayer.	98
Figure 4.24: FESEM cross section image for ns-CN _x deposited on pre-deposited a-C:H underlayer with surface roughness of 5.956.	100
Figure 4.25: FESEM surface image for ns-CN _x deposited on pre-deposited a-C:H underlayer with surface roughness of 2.783.	100
Figure 4.26: Variation of nitrogen to carbon N/C ratio of ns-CN _x films as a function of surface roughness of a-C:H underlayers.	101
Figure 4.27: Variation in FTIR absorbance spectra as a function surface roughness of a-C:H underlayers.	103
Figure 4.28: The FTIR spectra for CN _x nanostructures deposited on a-C:H underlayers with different roughness in the range of (a) sp ² , (b) sp ¹ and (c) sp ³ phases.	104
Figure 4.29: The FTIR spectra in the range of 1900-2300 cm^{-1} of ns-CN _x as a function of R _{UL} a-C:H underlayers.	106
Figure 4.30: Gaussian fitting profiles for FTIR spectra in the region 2000-2300 cm^{-1} for a-C:H underlayers with surface roughness 5.596 and 3.262.	107
Figure 4.31: AFM surface morphology of a-C:H underlayers at various time duration of H ₂ plasma treatment.	109
Figure 4.32: Variation of surface roughness of a-C:H underlayer as a function of t _H . Line is a guide to the eyes.	110
Figure 4.33: FTIR spectra of a-C:H underlayers as a function of t _H .	112

Figure 4.34: Variation of FTIR spectra for a-C:H underlayers prepared by RFPECVD as a function of t_H in regions of (a) 1300-1900 cm^{-1} and (b) 2700-3200 cm^{-1} .	113
Figure 4.35: The raw Raman spectra with strong background (a) and the Raman spectra after the background extraction (b) for a-C:H underlayers as a function of t_H .	117
Figure 4.36: Raman analysis of a-C:H underlayers prepared as a function of hydrogen treatment duration. Line is guide to the eyes.	118
Figure 4.37: The surface and cross-section images of ns-CN _x subsequently deposited on different t_H a-C:H underlayers.	120
Figure 4.38: Variation of nitrogen to carbon, N/C ratio of ns-CN _x deposited on different t_H a-C:H underlayers.	122
Figure 4.39: Variation in FTIR absorbance spectra of ns-CN _x as a function of H ₂ treatment time of a-C:H underlayers.	123
Figure 4.40: The FTIR spectra for ns-CN _x deposited on different t_H of a-C:H underlayers in the range of (a) sp ² , (b) sp ¹ and (c) sp ³ phases.	124
Figure 4.41: The FTIR spectra in the wavenumber range of 1900-2300 cm^{-1} of ns-CN _x as a function of t_H a-C:H underlayers.	125
Figure 4.42: Gaussian fitting profiles for FTIR spectra in wavenumber region of 1900-2400 cm^{-1} for a-C:H underlayer at t_H of 3, 5, 10 minutes and a-C:H underlayer without H ₂ treatment.	127

LIST OF TABLES

Table 2.1: The assignments FTIR vibrational frequencies of a-C:H underlayer and nanostructured CN _x films prepared by RFPECVD.....	30
Table 3.1: Deposition parameter of a-C:H layer and CN _x nanostructures.....	43

LIST OF PUBLICATIONS

Reviewed paper

1. Effect of pre-deposited carbon layer on the formation of carbon nitride nanostructures prepared by radio-frequency plasma enhanced chemical vapour deposition.

Materials Chemistry and Physics 130 (2011) 218–222

Noor Hamizah Khanis, Richard Ritikos, Maisara Othman, Nur Maisarah Abdul Rashid, Siti Meriam Ab Gani, Muhamad Rasat Muhamad, Saadah Abdul Rahman

Impact factor: 2.353 Category: Q1

2. Catalyst free carbon nitride nanostructures prepared by rf-pecvd technique on hydrogenated amorphous carbon template.

Materials Chemistry and Physics

Noor Hamizah Khanis, Richard Ritikos, Maisara Othman, Nur Maisarah Abdul Rashid, Siti Meriam Ab. Gani and Saadah Abdul Rahman

Impact factor: 2.353 Category: Q1

Other related papers

1. Effect of N₂ flow rate on the properties of CN_x thin films prepared by radio frequency plasma enhanced chemical vapor deposition from ethane and nitrogen.

Thin Solid Films (2012)

Maisara Othman, Richard Ritikos, Noor Hamizah Khanis, Nur Maisarah Abdul Rashid, Siti Meriam Ab Gani, Saadah Abdul Rahman

Impact factor: 1.909 Category: Q1

2. Effects of rf power on the structural properties of carbon nitride thin films prepared by plasma enhanced chemical vapour deposition.

Thin Solid Films 519 (2011) 4981–4986

Maisara Othman, Richard Ritikos, Noor Hamizah Khanis, Nur Maisarah Abdul Rashid, Saadah Abdul Rahman, Siti Meriam Ab Gani, Muhamad Rasat Muhamad

Impact factor: 1.909 Category: Q1

LIST OF ABBREVIATIONS

a-C:H	Hydrogenated amorphous carbon
CH ₄	Methane
CN _x	Carbon nitride
DC	Direct current
FWHM	Full width half maximum
H ₂	Hydrogen
MFC	Mass flow controller
N ₂	Nitrogen
ns-CN _x	Carbon nitride nanostructures
P _{UL}	Power of underlayer
RF	Radio frequency
RFPECVD	Radio frequency plasma enhanced chemical vapour deposition
R _{UL}	Surface roughness of underlayer
sccm	Standard cubic centimeter per minute
Si	Silicon
t _D	Deposition time duration
t _H	Hydrogen treatment time duration

CHAPTER 1 : INTRODUCTION

1.1 Development on Carbon Nitride

Studies on carbon nitride (CN_x) films have received considerable attention in recent years particularly after 1979 following the work by Cuomo et al. In their work, CN_x films were prepared by reactive RF sputtering of carbon in nitrogen (Cuomo et al. 1979). The interest on CN_x films further expanded following the work done by Liu and Cohen in 1989 which reported the feasibility of producing β -C₃N₄ which is analogous to β -Si₃N₄ having hardness comparable to diamond (Liu and Cohen 1989). Over the years, the research continues with the discovery of various types of CN_x structures including diamond, graphitic, polymeric and others (Shimoyama et al. 2001; Sung and Sung 1996; Zambov et al. 2000).

Fabrication of one dimensional CN_x nanostructures is one of the most significant progress in the study of carbon related films beginning with the work carried out by Pradeep et al. in incorporating N in fullerene in 1991. This was followed by various work to fabricate other CN_x nanostructures (ns-CN_x) such as nanotube, nanofiber, nanorod, nanowire, nanotip, nanosphere, nanoribbon, nanobell and several rare species including flower-like, leaf-like and worm-like structures (Droppa et al. 2002; Pradeep et al. 1991; Wang and Ostrikov 2009; Yang, et al. 2006). The most recent progression in the fabrication of ns-CN_x focused on incorporating nitrogen into single or multilayer graphene sheets (Qu et al. 2010; Shao et al. 2010; Wang et al. 2010). Figure 1.1 summarizes the progression of the works done on ns-CN_x.

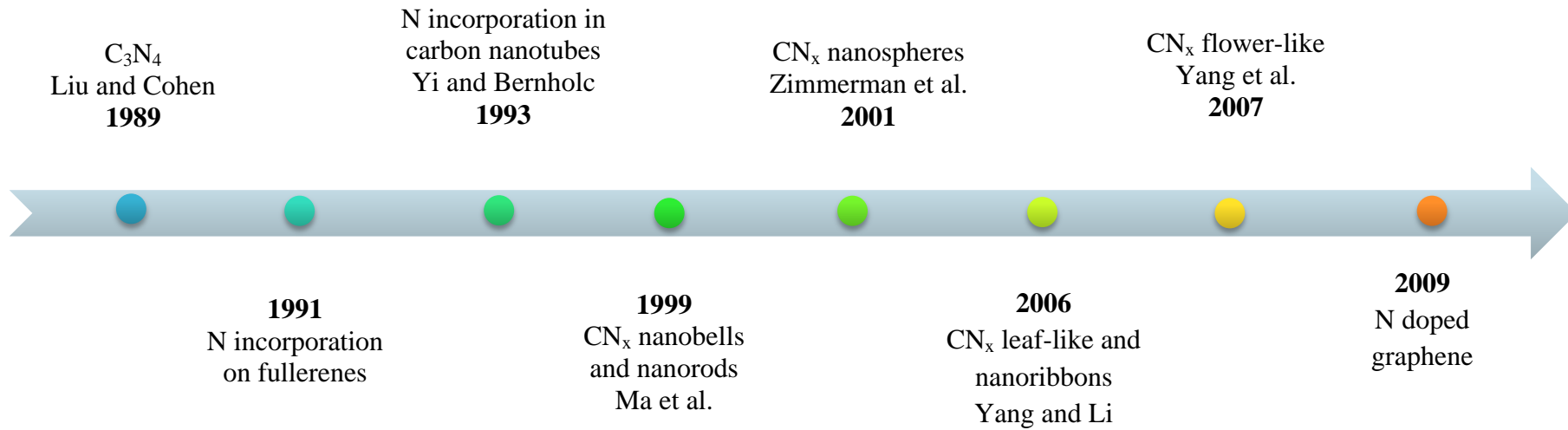


Figure 1.1: Progression chart of ns-CN_x.

1.2 Properties of Carbon Nitride and Application

CN_x is a promising material in various applications due to its interesting and unique properties. Nitrogen incorporation in carbon films leads to structural transformation with preference to bond as sp^2 bonded CN_x . In a study reported by Hu et al. on the preparation of carbon nitride films using plasma-assisted pulsed laser deposition technique having N incorporation increasing from 12% to 17% results in a decrease in sp^3 bonded carbon from 70% to almost 0% (Hu et al. 1998). Consequently, sp^2 content in the film increased. The increase in N content are caused by the preference in N to bond to carbon atoms in the films due to the strong electronegativity of N atom. Additionally, the N atom could be substituted in the carbon network to form double or single bond subjected to the N concentration (Wang et al. 2008).

N incorporation into carbon films brings about an enhancement in mechanical characteristic leading to excellent adhesion properties of these films (Lowther 1998; Ren et al. 1995). Additionally N incorporation also improve the local density of states near the Fermi level of these materials thus enhances their electronic characteristic. Such materials are suitable candidates for field emission devices which would show low turn-on voltage (Chan et al. 2003; Kim et al. 2011; Zhong et al. 2001). Lately, CN_x has gained considerable attention in its potential in various electrical devices, photo-catalyst, oxygen reduction agent, hydrogen storage material and active sensors (Bai et al. 2001; Jun et al. 1998; Pan et al. 2011a). One of the outstanding examples is that reported by Gong et al. on vertically aligned nitrogen containing carbon nanotube used as metal-free electrode in oxygen reduction reaction to improve fuel cell performance. These nitrogen containing carbon nanotubes are said to have better characteristic compared to conventional platinum electrode due to enhancement in electro-catalytic activity, being more stable for long term operation and at lower production cost (Gong et al. 2009). Integrated sensor systems including humidity sensitive field effect

transistor, temperature sensor and operational amplifier have utilized ns-CN_x as a component material in the device system. This ns-CN_x sensor was fabricated by analog mixed CMOS process (Lee et al. 2008). Other notable example of CN_x application is as hydrogen storage material. This study was done by Ito et al. using amorphous CN_x. The maximum hydrogen content uptake was reported as high as 0.78 wt% which is dependent on the type of hydrocarbon precursor used for the deposition such as CH₄, C₂H₆, C₂H₄ and C₆H₆ (Ito et al. 2008; Koh et al. 2012).

1.3 Related Works, Motivation and Objectives for This Study

A novel technique of growing vertically aligned CN_x nanorods was established and reported by Ritikos et. al. from Low Dimensional Materials Research Centre, University of Malaya where this work was carried out (Ritikos et al. 2011). This technique established the fabrication of CN_x nanorods by RF-PECVD at low temperature (100 °C) using a parallel plate configuration without the use of metal catalyst. The effect of high electric field induced by small electrode spacing between the powered electrode and the substrate holder resulted in the formation of these nanorods at fixed RF power of 80 W in a mixture of methane and nitrogen flow rates of 20 and 47 sccm, respectively. The work also shows that N incorporation is one of the crucial aspects in obtaining the vertical alignment. However, further work is proposed by that study to find ways of modifying these structures while retaining a large part of its deposition parameters and avoiding the use of metal catalysts. The use of catalytic materials can change the structure of CN_x but this sacrifices the purity of the resulting product since they introduce contaminants into the material structure. Thus, this work was motivated by these suggestions and also by the emergence of a recent study on the use of pre-deposited hydrogenated amorphous carbon (a-C:H) underlayer films as

template or seeding layer for the growth of carbon nanostructures (Wang et al. 2012b; Wang and Zhang 2006). These underlayer films would act as the substrate upon which this nanostructures are built on. Indeed substrate conditioning has been suggested as an important aspect that can influence the properties of the resulting upper-structures. Several studies have been carried out on the effects of substrate characteristic including variations in temperature, crystallinity orientation, morphology, type, and treatment process (Cao et al. 2007; Gielen et al. 1997; Jayatissa et al. 1998; Sakata et al. 2010; Smietana et al.2010).

In this work the ns-CN_x were deposited on a-C:H underlayers by RF-PECVD. The ns-CN_x were deposited from a mixture of methane and nitrogen at fixed deposition preparation conditions while methane was used as gas source for the growth of a-C:H underlayers prepared by varying a specific deposition parameter for each set of samples. The objectives of this work are as listed below:

- (1) To grow the ns-CN_x on a-C:H underlayers deposited under these conditions;
 - i. Different deposition time duration
 - ii. Different RF powers applied during deposition
 - iii. Different time duration of H₂ plasma treatment

- (2) To study the effects of structural properties of a-C:H underlayer on the morphology of the ns-CN_x formed.

1.4 Thesis Outline

This Chapter 1 features an introduction to this study and is followed by Chapter 2 which presents the literature review related to this work. The literature review is divided into four parts. The first part introduces various types of one-dimensional ns-CN_x including nanorod, nanotube, nanotip and also rare species such as nanobell, flower-like and leaf-like CN_x. The second part covers common deposition techniques employed to fabricate ns-CN_x. The third part looks into various types of substrate conditioning including film deposition on bare Si substrate, with catalytic assistance or with template assistance. The last part presents a brief theoretical background on the two analytical techniques used in this work that is Raman scattering and Fourier transform infrared spectroscopy.

Chapter 3 presents details on the experimental and analytical techniques used in this work. These include the deposition procedures and characterization of the films. The deposition procedures outline the description of the RFPECVD system, substrate preparation, film deposition and post deposition procedures. The characterization methods used comprise of atomic force microscopy (AFM), surface profilometer, scanning electron microscopy (SEM), Fourier transform infrared (FTIR) spectroscopy, Raman spectroscopy and Auger electron spectroscopy (AES). These methods are briefly described in this chapter.

Chapter 4 presents the experimental results, analysis and discussion related to the study of carbon underlayer films and the subsequent fabrication of ns-CN_x. The focus on this chapter is to study the effect of a-C:H underlayer on formation of ns-CN_x. For the a-C:H underlayers, their growth rate, surface roughness, chemical bonding and structural properties were studied. Subsequently, ns-CN_x were grown directly onto these a-C:H underlayer films. These ns-CN_x/a-C:H films were studied in terms of their

surface and cross sectional images, growth rates, elemental composition and bonding properties.

Chapter 5 presents the general conclusion of this study and also offers suggestions for future works.

CHAPTER 2 : LITERATURE REVIEW

2.1 Introduction

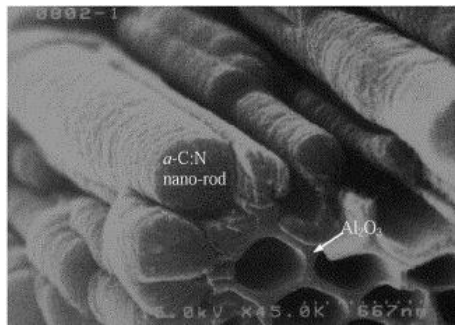
This chapter presents a literature review of two critical topics related to this work. The first part comprises a review on various types of one dimensional ns-CN_x which can consist of not only nanorod, nanotube, nanotip but also more rare species such as nanobells, nanoribbon, nanosphere, flower-like and leaf-like CN_x. Then, the next section looks into a brief theoretical background on two particular analytical techniques related to this work. These include the Fourier transform infrared and Raman analysis.

2.2 Carbon Nitride Nanostructures

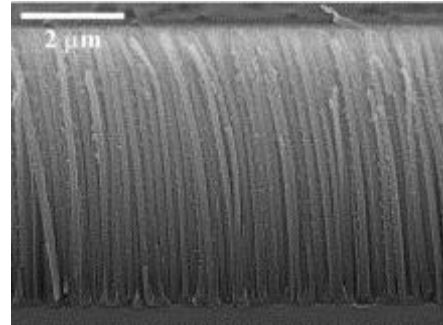
2.2.1 Nanorods

Nanorods are nanostructures with stick or rod shapes with relatively low aspect ratio. Several investigations have been done in order to fabricate these structures. Ritikos and co-workers have found CN_x nanorods deposited by RFPECVD at low temperature and not assisted by catalyst. The CN_x nanorods have diameter of 20-140 nm, length up to 5 μm with high nitrogen content of 42 at.% (Ritikos, et al. 2011). Moreover, Cespedes et al. also reported high density of 4 cm² area CN_x nanorods with diameter 50-200 nm and length 1 μm (Cespedes et al. 2005). CN_x nanorods were cited as one of the potential materials for applications in optic, electronic and optoelectronic devices (Liu et al. 2002a; 2002b). In another related work, Yang et al. obtained aligned ultra-fine crystalline CN_x nanorods prepared by pulsed laser ablation technique at room

temperature (Yang et al. 2007). Figure 2.1 shows SEM images of examples of CN_x nanorods.



(Liu et al. 2002a)



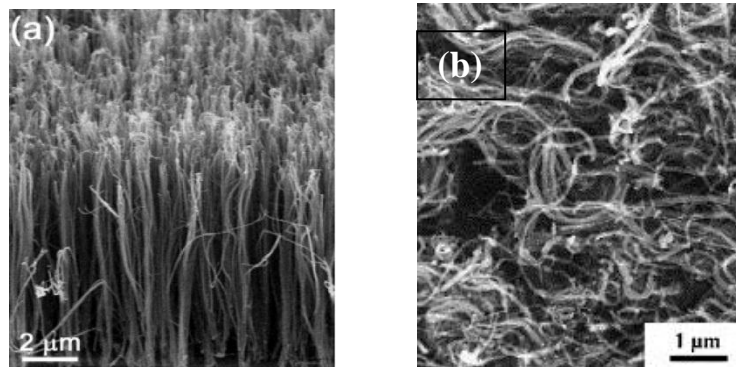
(Ritikos et al. 2011)

Figure 2.1: Example of FESEM images CN_x nanorods.

2.2.2 Nanotubes

Carbon nanotube (CNT) can be categorized either as multi wall or single wall nanotube. Single wall nanotube exhibit only one graphite layer with hexagonal lattice that appears wrapped up into a seamless cylinder. Multi wall nanotube form as a group of single wall nanotube with a mutual centre axis (Tu and Ou-Yang 2002). The inclusion of other element such as B and N into carbon nanotube network has been studied and it is expected to enhance their properties. From previous work, it was reported that doping nitrogen to carbon nanotubes network is expected to enhance its structural, magnetic and electronic properties and the size of carbon nitrogen atom is almost the same (Che, Peng, and Wang 2004; Ganesan et al. 2010; Krstić et al. 2007; Moradian and Azadi 2006). From experiment and simulation, Hu et al. showed that nitrogen influenced the structural properties of CN_x by which it causes relaxation of sp^3 bonded carbon to sp^2 bonding (Chan et al. 2004; Hu et al. 1998). The enhancement in electronic characteristic could be applied as field emitting devices (Chan et al. 2003; Kim et al. 2011; Zhong et al. 2001). This is due to improvement of local density of

states near the Fermi level in CN_x thus lowers the field emission threshold voltage (Srivastava et al. 2006). By functionalizing CNT with different transition metals such as W, Ti, Cr and Mn, the magnetic moment may be aligned to create either ferro or anti-ferro magnetic properties between neighboring metal atoms. This functionalized CNT can be applied in gas and energy storage devices (Pan et al. 2011b). Koh et al. showed that the graphitic CN_x nanotubes is one of the promising material in H_2 storage with the ability to uptake up to 4.66 wt. % hydrogen (Koh et al. 2012). Other applications include utilizing nitrogen doped carbon nanotubes coated with atomic layer of SnO_2 as functional material in lithium ion batteries (Meng et al. 2011). Figure 2.2 depicts the example of FESEM images of CN_x nanotubes.



(Choi et al. 2005)

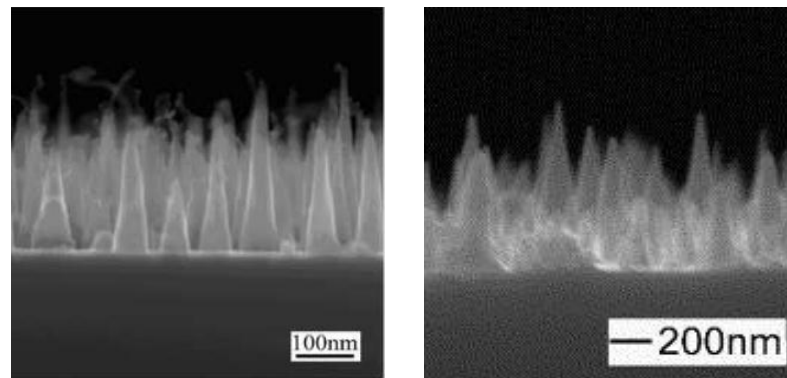
(Tao et al. 2007)

Figure 2.2: Example SEM images of various CN_x nanotubes structure.

2.2.3 Nanotips

CN_x nanotips show similar features as nanorods but lower aspect ratio and are tapered at the tip. Figure 2.3 shows the examples of FESEM images of CN_x nanotips. Liu et al reported on CN_x nanotips containing graphitic clusters which help to enhance its field emission characteristic (Liu et al. 2000) while Wang et al. stated that the CN_x nanotips discovered in their work have emission current density of 0.5 mA/cm^2 at $6 \text{ V}/\mu\text{m}$ and the turn on field of $5.2 \text{ V}/\mu\text{m}$ (Wang et al. 2012b). In a recent work on CN_x

nanotips prepared by hot filament plasma enhanced CVD system, a thin carbon underlayer was pre-deposited using RF magnetron sputtering prior to the deposition procedure. This underlayer was used as seed layer to promote the growth of nanotips. In another work, Dang and Wang reported on the effect of different growth duration on PL properties of CN_x nanotips. The longer duration resulted in stronger PL intensity due to strong effect of light trapping within the nanotips. This work showed that the dimension (length, height and diameter) of the nanotips influences the absorption and reflection process during the PL measurement (Dang and Wang 2012).



(Wang et al. 2012a)

(Wang and Zhang 2006)

Figure 2.3: FESEM images of CN_x nanotips.

2.2.4 Other ns- CN_x

Nanobells. Several works have reported the growth of CN_x nanobells (Bai et al. 2001; Wang 2002, 2006; Zhang, et al. 2002). This structure is made up of a series of stacking graphite cones growing parallel to each other in compartmentalized spaces, were produced by using microwave plasma enhanced CVD technique from a mixture of CH_4 and N_2 gases. From the HRTEM image shown in Figure 2.4, these structures were seen as nanotubes with nanobell compartments where the catalyst are encapsulated at the root of the fiber like structure. The bell-like structures are made up of a curved top and bend

edges. It was proposed that the nanobells growth follow the vapour-liquid-solid (VLS) growth mechanism. Nanobells give good field emission characteristic with high emission current. Furthermore, they exhibit high hydrogen uptake making them good candidate for hydrogen storage material (Bai et al. 2001; Zhang et al. 2002). Other related work produced polymerized CN_x nanobell by using electrochemical method that can be used as Li storage. From electrochemical performance of Li intercalation test, the specific capacity obtained for this nanobell is 480 mAhg^{-1} which is considerably high for such application (Zhong et al. 2001).

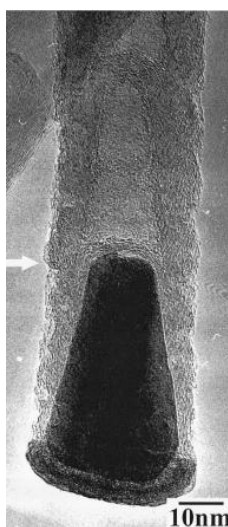


Figure 2.4: HRTEM image of CN_x nanobell (Zhang et al. 2002).

Nanoribbons. CN_x nanoribbons structures could be prepared using solvothermal technique through a chemical reaction of $C_3N_3Cl_3$ and Na. This product would form aligned and microsphere nanoribbons as depicted in Figure 2.5. These nanoribbons can be applied in nanoscale devices due to their special mechanical, electrical and optical properties (Li et al. 2006).

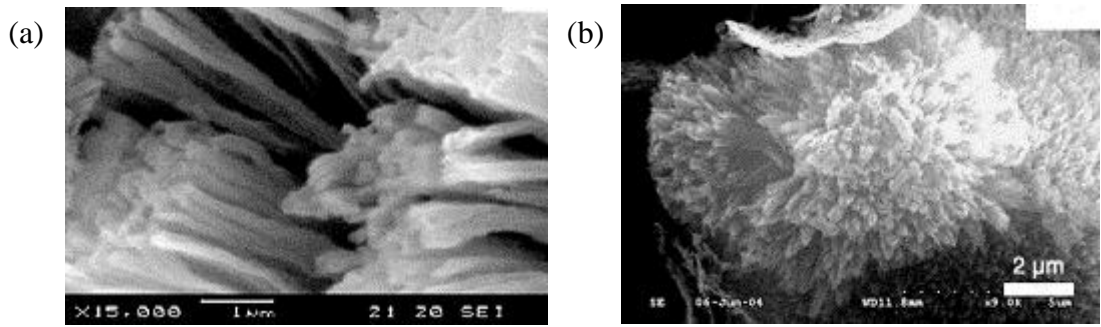


Figure 2.5: SEM images of carbon nitride (a) aligned nanoribbons and (b) microsphere nanoribbons (Li et al. 2006).

Nanospheres. CN_x nanospheres could be prepared using solution reaction or template-directed solid-state of cyanuric chloride or fluoride with lithium nitride. Zimmerman et al were able to obtain nanosphere with sizes in the range of 30-200 nm. The features of the nanospheres could be controlled by using silica spheres as template. It is important to control the sphere size and shape for their application and desired properties (Zimmerman et al. 2001). Figure 2.6 shows example of TEM image of the CN_x nanospheres.

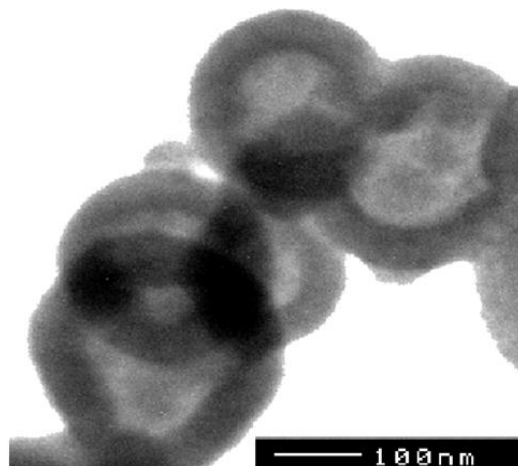


Figure 2.6: TEM image of the CN_x nanospheres (Zimmerman et al. 2001).

Flower-like. Bai et al. reported the formation of flower-like CN_x prepared by the high-energy ball-milling and subsequent thermal-annealing process in a horizontal tube furnace using melamine as precursor. In this work, annealing temperature of up to 650°C is the key factor in the successfully formation of flower-like CN_x (Bai, Cao and Xu 2010). Yang et al. fabricated flower-like CN_x via liquid pulsed laser ablation technique using ammonia solution. These structures are made up of self-assembled nano-petals structures. Different ablation time, laser energy, ammonium concentration and drying speed play crucial roles in the formation of these flower-like structures. Figure 2.7 shows examples of SEM images of flower-like CN_x (Yang et al. 2007).

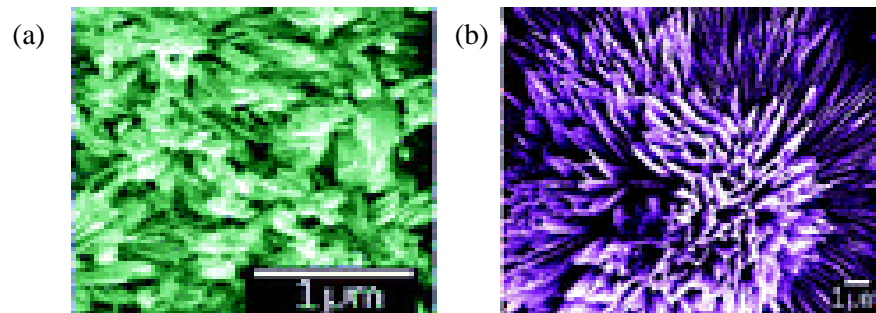


Figure 2.7: SEM image the formation of (a) nano-petals and (b) flower-like CN_x structure (Yang et al. 2007).

Leaf-like. Leaf-like CN_x structure consists of large number of packed ordered nanorods could be formed by self-assemble process using liquid phase pulsed laser ablation of graphite target and ammonia solution. The formation of leaf-like structure depends on the ablation duration. Such structures have wide band gap and are therefore suitable for optical application. Example of this structure is shown in Figure 2.8.

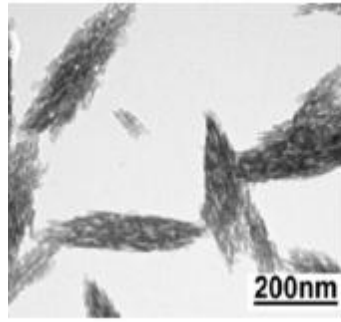


Figure 2.8: The TEM image of CN_x leaf-like structures (Yang et al. 2006).

2.3 Review on Preparation of Carbon Nitride Nanostructures

The fabrication of CN_x nanostructures can be obtained by several preparation techniques. Their properties are strongly dependent on the deposition parameters. Therefore, comparative study between different approaches in synthesizing CN_x nanostructures is essential. The synthesis of CN_x structure was started by Yi et al. in 1993 not long after Iijima discovered carbon nanostructures which was identified as carbon nanotube (Ayala et al. 2010; Iijima 1991; Yi and Bernholc 1993). Techniques that have been utilized to produce CN_x nanostructures include sputtering, arc discharge, laser ablation and chemical vapour deposition (CVD). CVD consists of different variation including microwave plasma CVD, floating catalyst CVD, hot filament plasma enhanced CVD, radio frequency plasma enhanced CVD and electron cyclotron resonance CVD. CVD is proven to be the most effective technique in producing large deposition area and seldom requires extensive post treatment compared to other techniques (Tao et al. 2007; Zhong et al. 2001). Additionally, this well-known technique is preferred because of the ease in control and the deposition could be carried out at low deposition temperature.

2.3.1 Sputtering

In sputtering technique, film deposition is carried out by using radio frequency (RF), direct current (DC) or pulsed DC source as power sources and it generates ions that can eject material through sputtering process from a target, then deposits the sputtered elements onto a substrate. CNT coated with amorphous CN_x and ns- CN_x have been obtained by RF magnetron sputtering (Banerjee et al. 2010; Kim et al. 2011). The fabrication process was carried out on c-Si substrate at a working pressure range of 6.7×10^{-3} to 5×10^{-2} mbar with Ar to N_2 flow rate ratio of 1:1 and 4:1, respectively. High purity graphite was used as target. The deposition was carried out for 3 hours and 10 minutes for CNT coated with amorphous CN_x and ns- CN_x , respectively. In the fabrication of the CNT coated with amorphous CN_x , Ni with thickness of 7 nm was used as catalyst. In another study, Suenaga et al. deposited nanotubulite CN_x using DC magnetron sputtering system. The sample was deposited on cleaved NaCl substrate in Ar/ N_2 . The deposition temperature was at 350 °C (Suenaga et al. 1999). Examples of conventional sputtering system are shown in Figure 2.9.

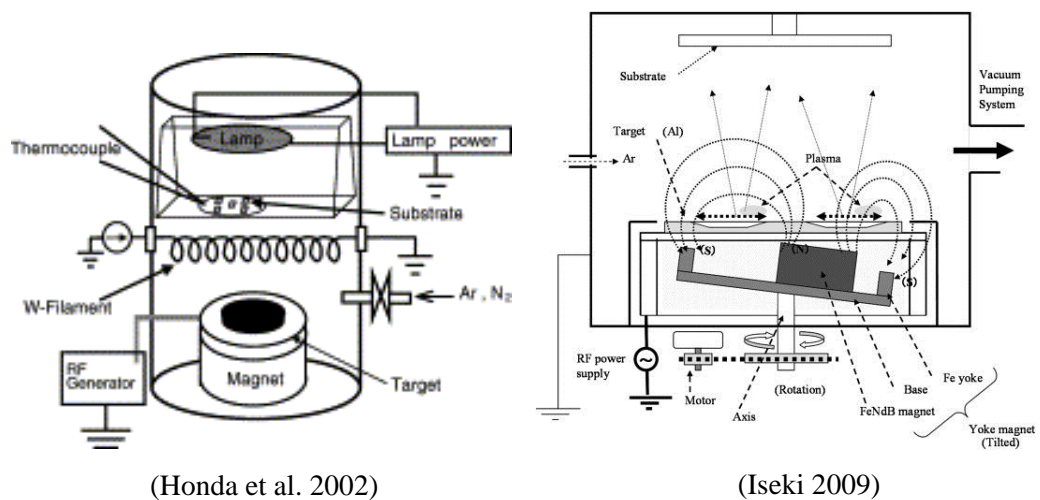


Figure 2.9: The example of schematic diagram of magnetron sputtering system.

2.3.2 Arc Discharge

Arc discharge has been one of the earlier methods in producing ns-CN_x. The arc discharge occurred as the anode rods in the schematics move closer to the cathode, thus forming a plasma. Glerup et al. reported on nitrogen doped single wall carbon nanotube prepared using graphite mixed with melamine and Ni/Y as catalyst and these were packed into the drillings of anode rods. Yu et al. prepared nitrogen doped fullerenes using a similar technique. The preparation of nanotubes and nitrogen doped fullerenes was carried out at current of 95–100 and 100–135 A, respectively (Glerup et al. 2004; Yu et al. 1995). Other related work includes the fabrication of nitrogenated carbon nanotubes using Fe, Co and Ni as catalyst at deposition pressure 300 Torr in nitrogen – helium mixture ambient (Droppa et al. 2002). An example of a conventional arc discharge system is shown in Figure 2.10.

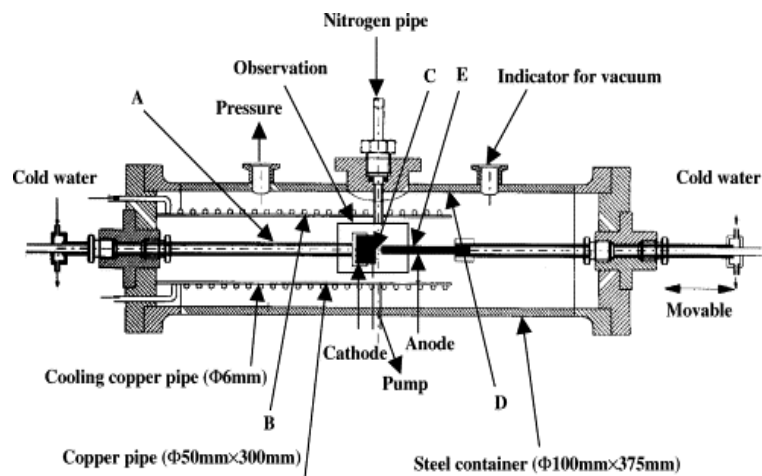


Figure 2.10: Example of schematic diagram of arc discharge system (Cui et al. 2004).

2.3.3 Laser Ablation

Laser ablation is one of the common physical vapour deposition used in producing ns-CN_x. Laser ablation occurs when short laser pulses are irradiated onto a solid or liquid target, which at certain conditions will form a plasma. The utilization of laser ablation has a few advantages such as enabling direct chemical analysis for solids, produces high quality sample with low contamination and enables analysis to be done without separating the solids and solution. CN_x nanorods has been prepared using a Nd: YAG laser with wavelength of 532 nm focused onto a solid graphite target which was submerged in a 35% ammonia solution at longer ablation duration of 5 hours. Alternatively, at lower deposition duration (2 hours), only nanoparticles were formed (Yang et al. 2007). Other ns-CN_x using this technique includes flower-like and leaf-like CN_x which could be produced by controlling the deposition duration (Yang et al. 2007b, 2006a, 2006b). Examples of conventional laser ablation system are shown in Figure 2.11.

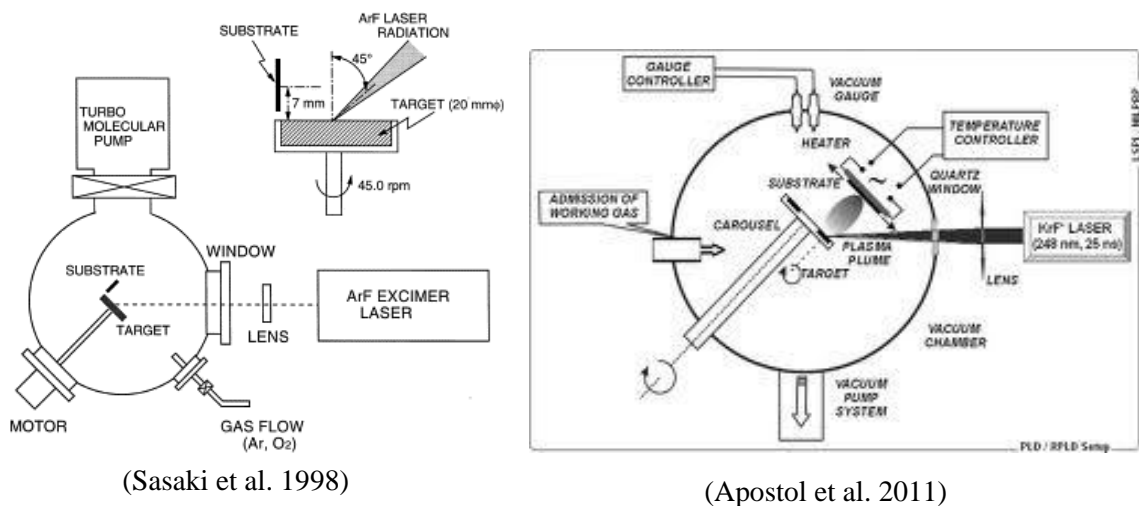


Figure 2.11: Example of schematic diagram of pulsed laser ablation system.

2.3.4 Chemical Vapour Deposition

2.3.4.1 *Hot filament plasma enhanced CVD*

Hot filament plasma enhanced CVD (HFPECVD) has been utilized to fabricate CN_x nanotips on carbon substrates (Dang and Wang 2012; Wang et al. 2005, 2012a, 2012b; Wang, Dong and Xu 2011; Wang and Zhang 2006, 2007). A coiled tungsten filament with diameter of 1 mm was used and was placed at varied distance of 8 -10 mm to produce CN_x nanotips. Negative bias voltage or RF power was applied to substrate holder to create plasma. The filament and substrate temperature were heated in the range of 1600 to 1950 °C and 750 to 800 °C, respectively. The filament was pre-treated in a H_2-NH_3 plasma for 5 minutes in order to improve nucleation. The CN_x nanotips were grown using a mixture of CH_4 , NH_3 and H_2 gases and flow rates of 20, 10–70 and 40–70 sccm, respectively. Apart from that, Ar has also been used as reaction gas usually at flow rate of 30 sccm. The nanotips were grown between 12–30 minutes in a total pressure of 2-4 kPa. Additionally, CN_x nanotubes and some rare species such as worm-like and foil-like nanostructures have also been produced using this technique. (Kurt, Bonard and Karimi 2001a, 2001b). Figure 2.12 depicts the example of schematic diagram of HFPECVD system.

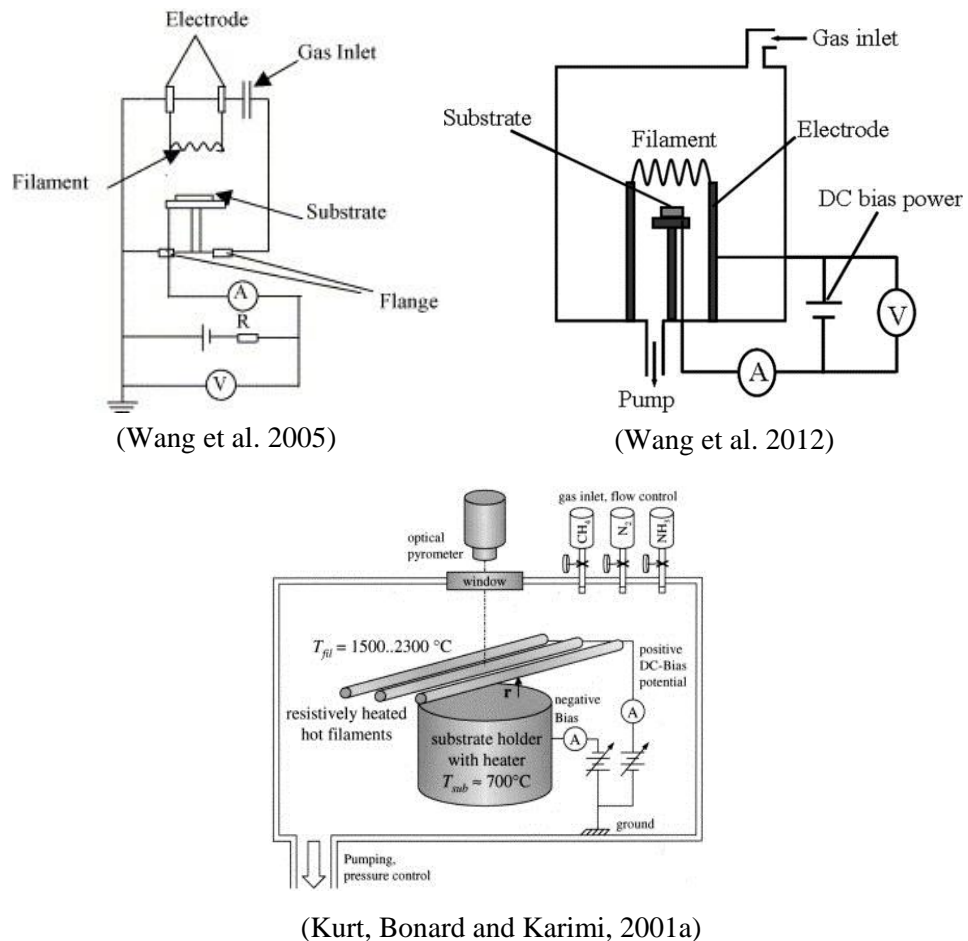


Figure 2.12: Example of schematic diagram of HFPECVD system.

2.3.4.2 *Electron cyclotron resonance CVD*

Electron cyclotron resonance CVD (ECRCVD) has been used to obtain CN_x nanotubes, CN_x nanotips and vertically aligned amorphous CN_x nanorods as reported by Liu et al., Sung et al. and Lai et al. (Lai et al. 2003; Liu et al. 2000, 2002b; Sung et al. 1999). The CN_x nanorods and nanotubes structures were deposited on anodic alumina composite membrane with pore diameter 100-250 nm and 50-80 μm length which acts as a template for the growth of the structure. All structures were prepared using a mixture of C_2H_2 and N_2 gases. The electron cyclotron resonance operated using a microwave excitation at 2.45 GHz to generate plasma was fed perpendicularly through the quartz dome into a magnetic field created by coils surrounding the chamber. It is believed that ECRCVD provides the highest plasma density compared to other CVDs

such as RF, dc or microwave plasma enhanced CVD. For template assistance CN_x nanorods fabrication, the alumina template was eliminated by mechanical polishing post treatment. Figure 2.13 shows some examples of schematic diagram of ECRCVD system.

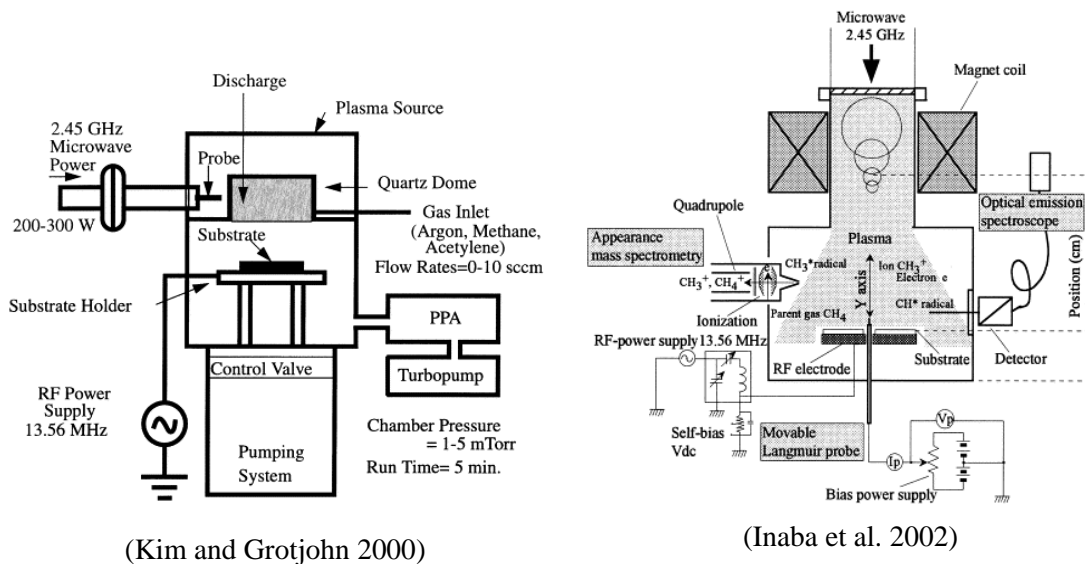


Figure 2.13: The example of schematic diagram ECRCVD system.

2.3.4.3 Radio frequency plasma enhanced CVD

Examples of radio frequency plasma enhanced CVD (RFPECVD) system are shown in Figure 2.14. This is a popular technique used in the fabrication of CN_x films. Deposition parameters such as temperature, flow ratio, RF power and pressure are crucial aspects which influence the morphology of the CN_x nanostructures. Cespedes et al. reported CN_x nanorods growth prepared by catalyst assistance at deposition temperature in a range of 650-800 °C (Cespedes et al. 2005; Ritikos et al. 2011). CN_x nanorods were synthesized without assisted by catalytic material was reported by Ritikos et al. These CN_x nanorods were prepared by RFPECVD technique using CH_4

and N_2 as precursor gases and deposited at different duration of 5 to 90 minutes on p-type $\langle 111 \rangle$ Si substrate at low temperature $\sim 100\text{--}200^\circ\text{C}$ and RF power of 60 W.

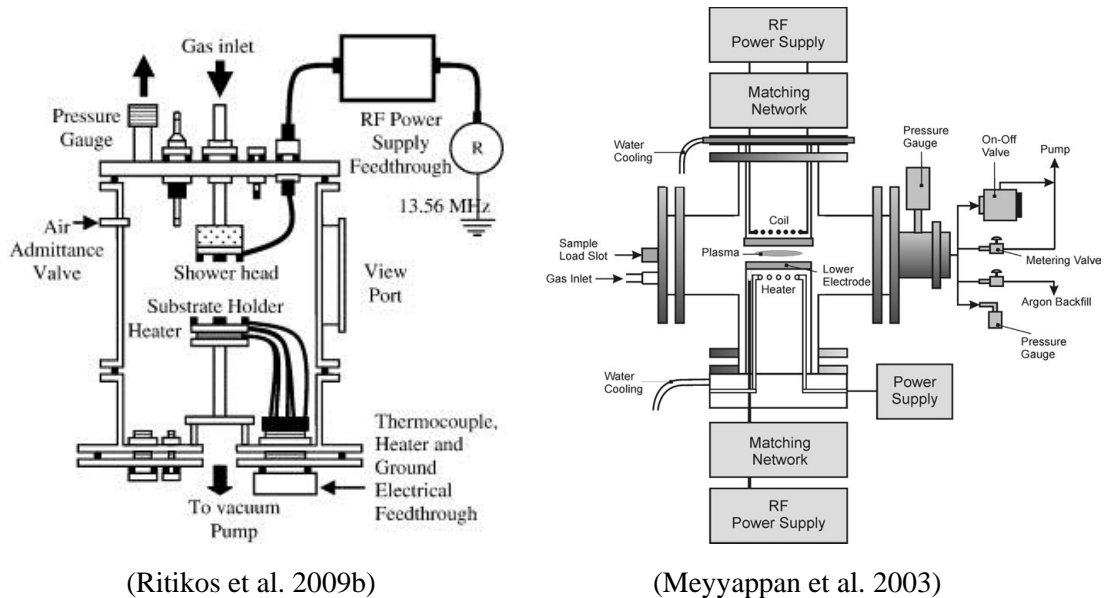


Figure 2.14: The schematic diagram of RFPECVD system.

2.3.4.4 Microwave plasma CVD

Examples of microwave plasma enhanced CVD (MWPECVD) is shown in Figure 2.15. They are one of the common techniques which have been used in producing ns- CN_x including nanotubes and nanobells. Plasma was generated by the microwave source working at frequency of 2.45 GHz. The CN_x nanotubes could be grown on Si substrate from a mixture of different gases such as CH_4 , C_2H_2 , NH_3 or N_2 and are usually assisted by catalyst such as Fe and Ni. The deposition temperature, pressure and gas flow rate ratio are critical parameters that influenced the formation of the structures. Nanotubes and nanobells structures could be deposited on Si substrate at temperature between $450\text{--}800^\circ\text{C}$ for 10 to 30 minutes at microwave power of $500\text{--}600$ W and pressure of 2 kPa (Bai et al. 2001; Chan et al. 2003; Srivastava et al. 2006; Zhang et al. 2002; Zhong et al. 2001).

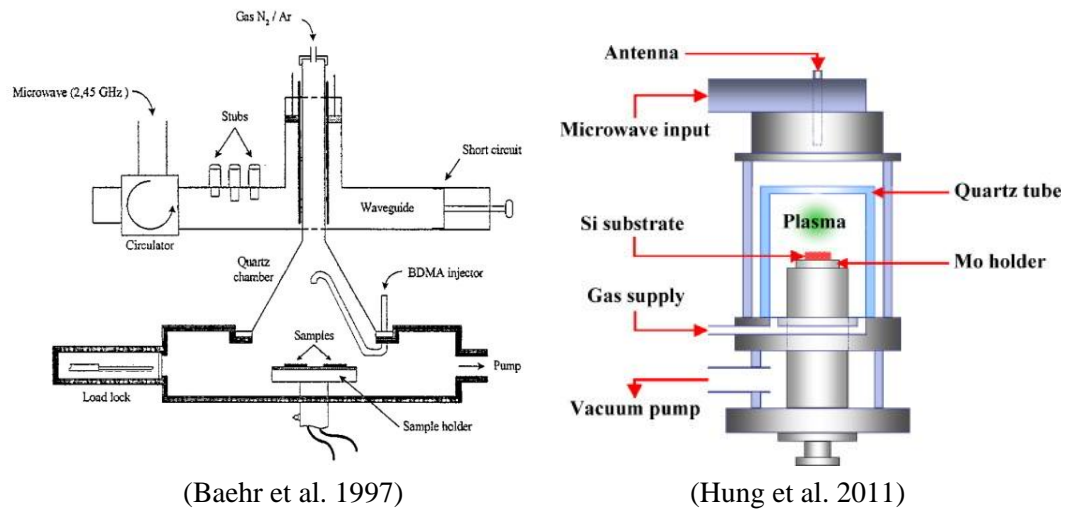


Figure 2.15: Example of schematic diagram of MWPECVD system.

2.3.4.5 Floating catalyst CVD

There are several works reported on the fabrication of CN_x nanotubes and nanofibers by using this technique. Usually single or multilayered catalyst such as Fe, Ni, Al_2O_3 and MgO are used with carbon and nitrogen sources in a mixture of acetonitrile and ethanol or CH_4 , NH_3 and H_2 . The deposition of the films could take as long as 8 to 60 minutes depending on the deposition conditions and temperature of the substrate. The deposition requires pressure of the horizontal tube furnace to be in range of 1×10^{-6} to 89 mbar. N_2 or Ar gas is flowed into the tube before it was heated to the desired temperature. When the entrance temperature increase to about 200 °C, the precursor was introduced into the tube and evaporation begins. The temperature of the furnace is increased up to 950 °C. The vapour was carried out by the gas flow to the higher temperature region and thus the reaction occurs. Then, the tube furnace is allowed to cool down to room temperature (Ayala et al. 2007a, 2007b; He et al. 2005; Koós et al. 2009; Liu et al. 2005, 2010; Maldonado, Morin and Stevenson 2006;

Maldonado and Stevenson, 2005; Suenaga et al. 2000; Tao et al. 2007). Figure 2.16 shows the typical schematic diagram of a floating catalyst CVD system.

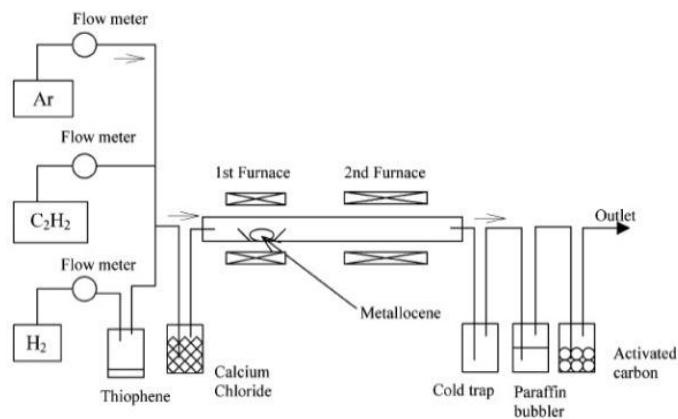


Figure 2.16: Example of typical schematic diagram of floating catalyst CVD system (Singh et al. 2002).

2.4 Substrate Condition

2.4.1 Bare Substrate

Si and SiO₂ wafers are common substrate in ns-CN_x fabrication. The Si wafer have two different impurity doping which are n and p-type with various crystal orientation including <111> and <100> which provide various structural properties of the resulting product. Si substrate needs to be cleaned before being used in order to remove contamination and maintain the quality of substrate. A number of methods are used in these cleaning processes. The standard method involves sequential immersion in HF, HCl and NH₄OH solutions with thorough rinsing in deionized water in between and finally are rinsed in acetone and ethanol and dried in a flow of N₂. Other approach proposed include that of Brown et al. where the substrates are immersed in acetone and isopropyl alcohol in ultrasonic bath for 5 minutes in each solution and then the substrates were rinsed in deionized water and dried in N₂ flow (Brown et al. 2011).

2.4.2 Catalyst

The use of catalytic materials to produce ns-CN_x is a common practice. Usually, transition metals such as Ni, Co, and Fe were used to achieve the desirable structures (Lin et al. 2003; Sen et al. 1997). Catalyst preparation technique could be divided into two types. The first is solution base preparation, such as dissolution, stirring, precipitation, refluxing, separation, annealing or calcination. These techniques are commonly used in CVD sample preparation. The second is physical method including thermal evaporation, lithography, sputtering, transfer printing and combustion (Lin et al. 2003; Tao et al. 2007). These physical techniques are more widely used since they are quicker, easier and enables small patterns compared to solution base techniques. There are three factors affecting the formation of catalytic growth of ns-CN_x. First, the selection of catalyst where different materials formed different structures through the precursor gases due to different catalytic reaction. Secondly, the effects of adsorption or absorption on the catalyst surface due to the surface energy and its electronic state. Finally, the structure of the catalyst including its size and crystallographic structure (Lin et al. 2003). He et al. produced aligned nitrogen doped carbon nanotube by CVD technique on Si substrate using Fe as catalyst and acetonitrile as precursor gas while Sen et al. obtained CN_x nanotubes by pyrolysis of pyridine on ~50 nm size of Co powder (He et al. 2005; Sen et al. 1997). Ayala et al. used multilayered catalyst films which promote the formation of vertically aligned nitrogen doped carbon nanotube prepared from acetonitrile. These multilayered catalysts contain different metallic films made up of Si, Al, MgO, Mo and Fe. The catalyst was then removed by mild sonication (Ayala et al. 2007b). According to Brown et al., even though the purification method has been enhanced recently, there are still few obstacles which should be resolved such as the possibility of structural damage, the extra cost and process (Brown et al. 2011).

2.4.3 Template and Underlayer

Another approach in synthesizing ns-CN_x is by using template assistance. This technique does not involve the use of catalyst. Examples are the CN_x nanotubes that were prepared by ECR-CVD on anodic alumina (Sung et al. 1999). The anodic alumina was used as the template, prepared by anodizing aluminum foil in aqueous phosphoric and oxalic acid mixture which produced channels with parallel and packed arrays structures. CN_x nanotubes were formed in the channels with the help of a bias voltage applied to the graphite substrate. After the CN_x nanotubes were obtained, the anodic alumina template was chemically removed by dissolving them in KOH solution. Similar method was used by Liu et al. for fabrication of CN_x nanorods (Liu et al. 2002). Figure 2.17 shows examples of template used in CN_x nanotubes fabrication.

Other successful method used in the formation of ns-CN_x is by depositing a carbon underlayer prior to the growth of the ns-CN_x. The carbon underlayer acts as seed layer (Wang et al. 2011; Wang and Zhang 2006). The surface roughness of the carbon underlayer effects the growth rate of the ns-CN_x (Wang and Ostrikov 2009).

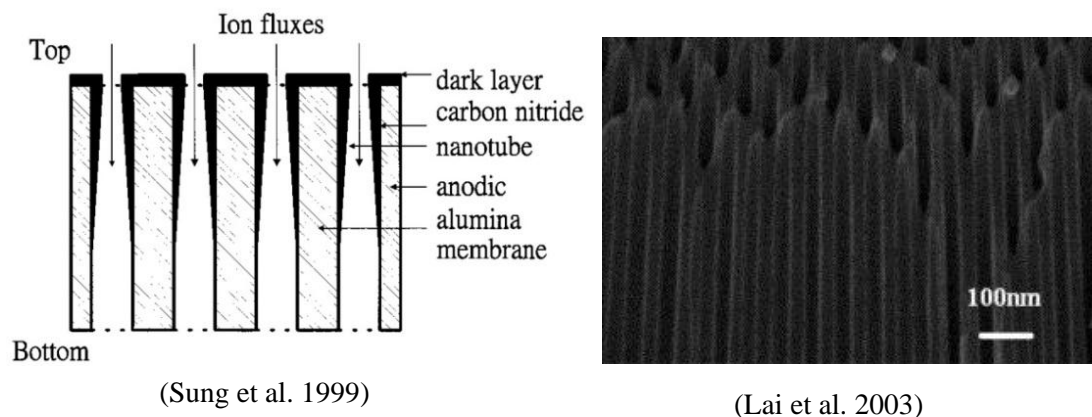


Figure 2.17: The example of template used in CN_x nanotubes fabrication.

2.5 Review of Analytical Methods

The following section reviews some of the analytical methods used in this work. The review includes Fourier transform infrared (FTIR) and Raman scattering analysis. Other methods including profilometer measurement, atomic force microscopy (AFM), field emission scanning electron microscopy (FESEM) and Auger electron spectroscopy (AES) analysis are not discussed since they can be interpreted directly from images and/or instrumental software.

2.5.1 Fourier Transform Infrared Spectroscopy

Fourier transform infrared (FTIR) spectroscopy is one of the common and popular characterization tool widely used in the determination of bonding in a-C:H and CN_x . Any compound, either organic or inorganic has covalent bonds which would absorb electromagnetic radiation in various specific frequencies in the infrared region. The wavenumber of interest is in the region of $400-4000\text{ cm}^{-1}$. The vibrational energy transition for different bonding in a compound are assigned to specific value, thus could be used as the 'finger print' of the material. In general, there are a few types of vibrational motion including stretching, bending, scissoring, wagging, rocking and twisting. These are shown in Figure 2.18.

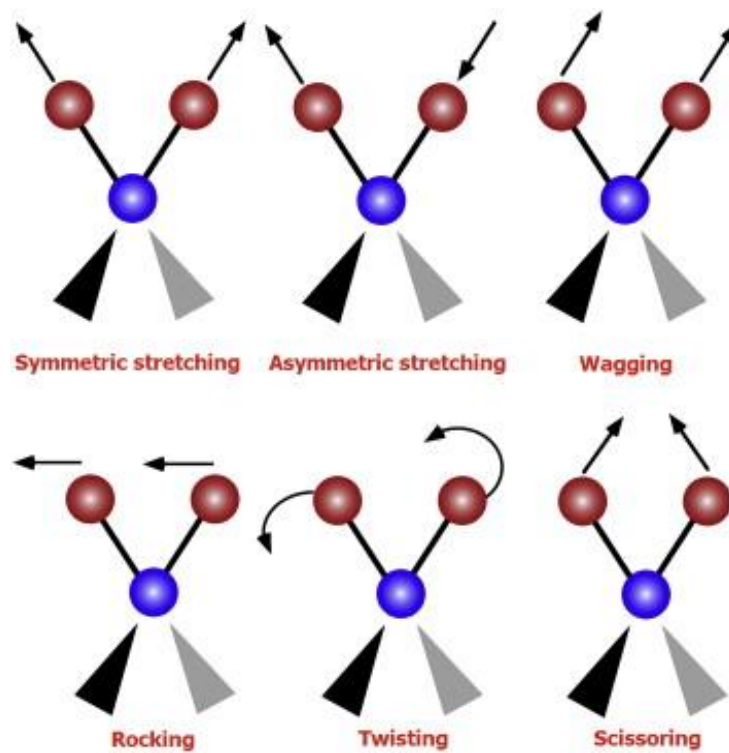


Figure 2.18: Type of vibration mode in FTIR analysis (Marcelli et al. 2012).

From the FTIR spectrum obtained, the peak position and intensity of each bond are assigned. However, the interpretation of the data should be done carefully since there are some overlapping peaks which form broad peak thus clustering the shape and the profile of the spectrum. Deconvolution method using Gaussian fitting has been used extensively to solve this problem (Fanchini et al. 2005; Rodil 2005). Figures 2.19 and 2.20 show examples of typical FTIR spectra of a-C:H and CN_x films.

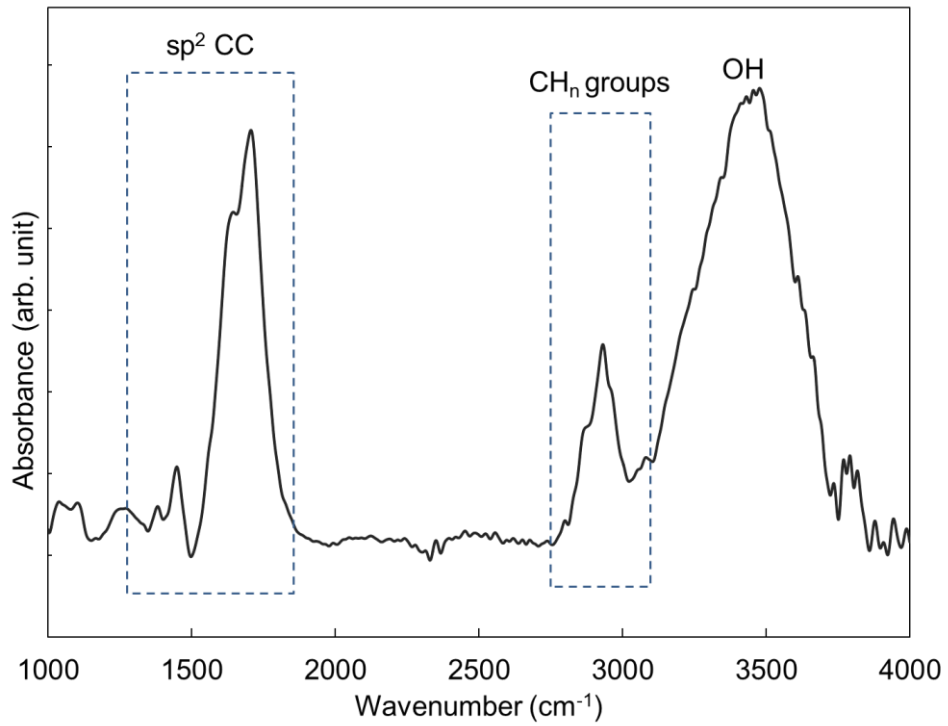


Figure 2.19: Example of typical FTIR spectrum of a-C:H film.

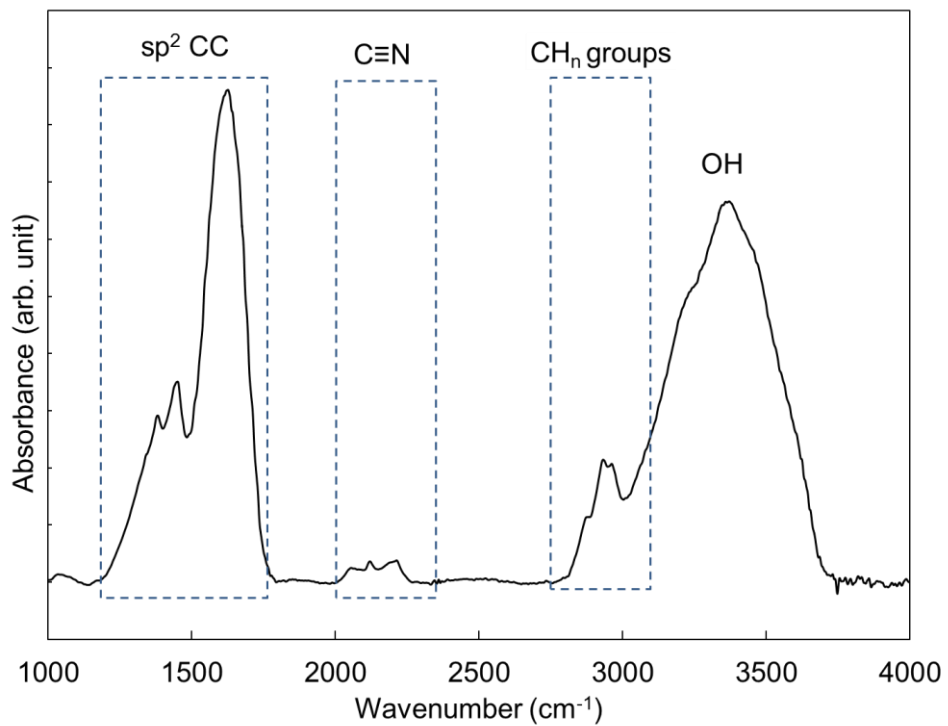
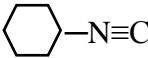
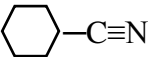


Figure 2.20: Example of typical FTIR spectrum of CN_x film.

For the example shown, the spectrum could be divided into specific bonding regions. Each bonding component was fitted into three regions. Table 2.1 list the various functional groups that could be obtained in a-C:H and CN_x films for these three main regions.

Table 2.1: The assignments of FTIR vibrational frequencies of a-C:H underlayer and nanostructured CN_x films prepared by RFPECVD.

Region (cm ⁻¹)	Wavenumber (± 0.1 cm ⁻¹)	Assignment	Reference
1300-1800	1460	C sp ³ H ₂ bending	Fanchini et al. 2005; Ritikos et al. 2009;
	1630	C=C and/ or C=N	
	1680	N-H	
	1700	C=C stretching	
2000-2300	2060	HCN	Kundoo et al. 2003; Mutsukura and Akita 1999; Mutsukura 2001
	2105		
	2160	C ₂ H ₅ -N≡C	
	2190	CH ₃ -N≡C	
	2215		
	2245	hydrocarbon groups-C≡N	
2800-3700	2800-3000	C-H _n stretching	Ritikos et al. 2009; Pereira et al. 2006; Kundoo 2003; Fanchini et al. 2005
	2920	sp ³ CH ₂ or sp ³ CH or C sp ³ H ₂ asymmetric stretching	
	2965	sp ³ -CH ₃	
	3200-3500	N-H stretching	
	3330	N-H and / or O-H	
	3350	N-H	

2.5.2 Raman Spectroscopy

Raman spectra are associated with the structure of material. The various type of carbon structure such as diamond, graphite, amorphous and others structures would give different Raman spectra. Firstly, it is important to identify the general type of structure according to its features. Example of typical Raman spectra for different types of structure is presented in Figure 2.21 (Chu and Li 2006).

Typical Raman spectrum for carbon films shows two prominent peaks due to sp^2 sites known as the D and G peak at Raman shift of 1360 and 1560 cm^{-1} , respectively. However, there may also be one background peak at Raman shift of 1500 cm^{-1} typically found for amorphous hydrogenated carbon (Huang et al. 2003). The D peak is attributed to breathing modes of sixfold aromatic rings and only become active in the presence of disorder. The G peak is due to bond stretching of all pairs of sp^2 atoms both in rings and chains (Escobar-Alarcón et al. 2005; Ferrari, Rodil and Robertson 2003; Ferrari 2007; Zhao et al. 2011). There are four information which could be deduced from the Raman analysis. This includes (a) sp^2 phase clustering, (b) presence of sp^2 chains or rings, (c) bond disorder and (d) relative content of sp^2 and sp^3 .

The Raman interpretation typically includes the deconvolution using Gaussian fitting method (Marchon et al. 1997; Park et al. 2005). From this fittings, five parameters can be extracted including its peak position and full width half maximum (FWHM) of the D and G peaks and also the peak integrated intensities to calculate the I_D/I_G ratio.

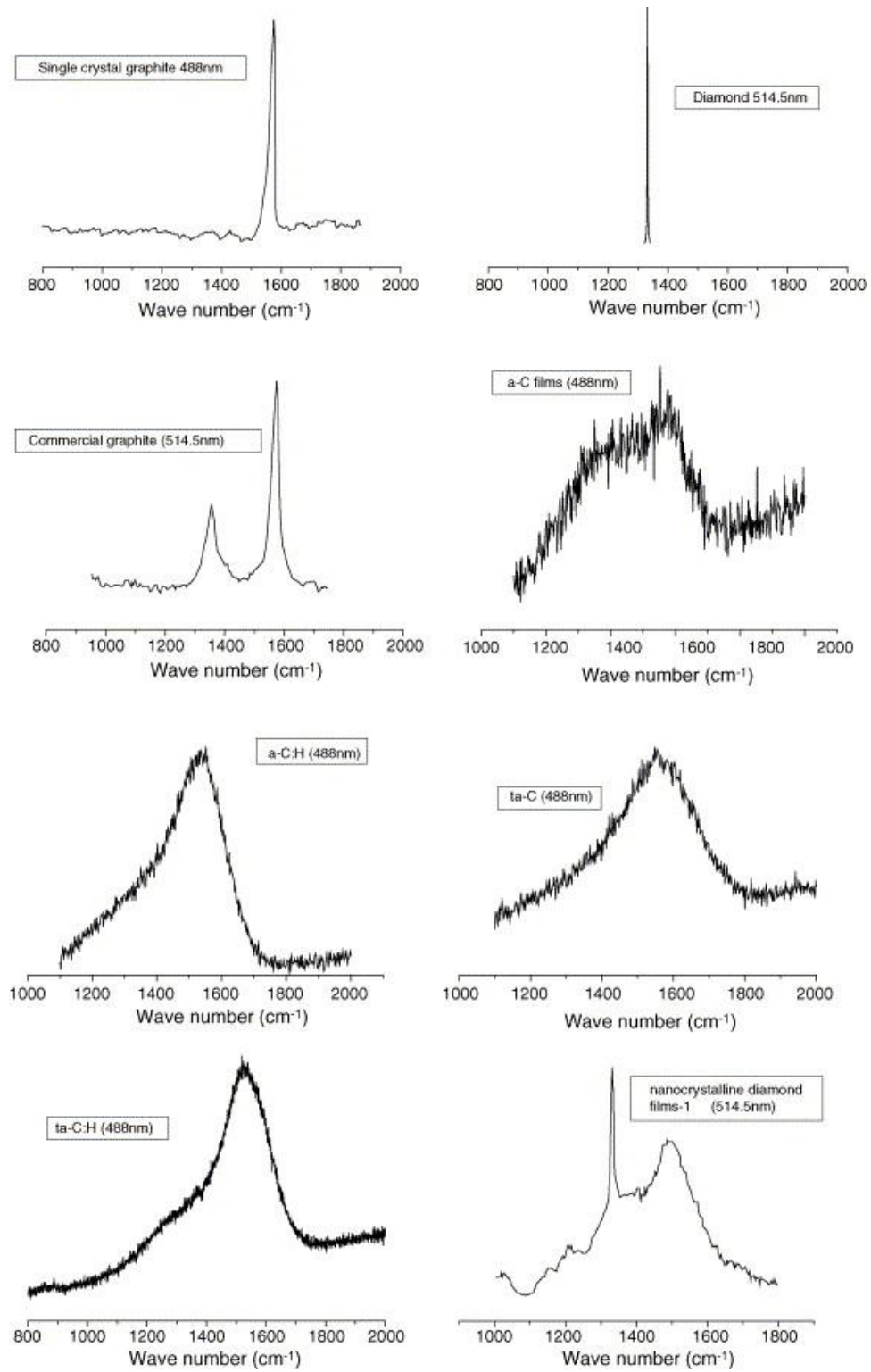


Figure 2.21: Typical Raman spectra for carbon based materials.

The red-shift (to higher wavenumber) in G peak position towards 1600 cm^{-1} being higher than that of graphite (1550 cm^{-1}) though not exceeding the limit of graphitic carbon may imply that these films have high degree of graphitization. This may also imply that the film exhibit characteristic of olefinic (chain sp^2 group) with shorter bond length (Gilkes et al. 1998). The blue shift (to lower wavenumber) in D peak position can be attributed to the strained or curved graphite plane which occurs when there is a change in the vibration frequency due to the change of spacing between the atoms (Ferrari and Robertson 2000; Yu, Lee and Lee 2002).

A broadening in the width of the D peak (FWHM_D) is correlated to the increase in disorder due to the re-distribution of clusters with different orders and dimensions. This is due to the presence of different order in the clusters. The FWHM_G is also sensitive to structural disorder though this is attributed to bond angle and bond length distortion. If there is no defect within the cluster, the size of FWHM_G would be small. Conversely, an increase in bandwidth of both D and G, indicates lower degree of clustering and less ordered structure (Zhao et al. 2011).

The I_D/I_G ratio depend on the size of the sp^2 phase (Casiraghi et al. 2005). According to Zhao et al, the low I_D/I_G ratio (<1) in disordered graphite is due to the decrement of defect or ordering of carbon atoms. This is attributed to small crystal size or the destruction of symmetry in the crystalline structure. However in amorphous carbon, the increase in I_D/I_G towards unity ($I_D/I_G \approx 1$) indicates an increase disorder or decreasing crystallite size (Zhao et al. 2011). Further increase in I_D/I_G indicates an increase in the number and/or size of graphitic cluster in the films (Ferrari and Robertson 2000).

CHAPTER 3 : EXPERIMENTAL AND ANALYTICAL TECHNIQUES

3.1 Introduction

In this work, carbon nitride (CN_x) nanostructured films were prepared using radio frequency plasma enhanced chemical vapour deposition (RFPECVD) technique. This chapter presents the deposition procedures, experimental and analytical techniques used in the characterization of the films. The first section focused on the RFPECVD system, substrate preparation, film deposition and post deposition procedures. The substrate preparation procedures consist of the substrate cleaning and pre-deposition treatments. The next section discussed the characterization methods used, which include atomic force microscopy (AFM), surface profilometer, scanning electron microscopy (SEM), Fourier transform infrared (FTIR) spectroscopy, Raman spectroscopy and Auger electron spectroscopy (AES).

3.2 Radio Frequency Plasma Enhanced Chemical Vapour Deposition System

The radio frequency plasma enhanced chemical vapour deposition which is made up of a reaction chamber connected to three part subsystems consisting of a vacuum system, gas distribution system and electrical system (Ritikos et al. 2009). Figure 3.1 shows the schematic diagram of the RFPECVD system.

In this work, pure methane 99.995% (CH_4), nitrogen 99.995% (N_2) and hydrogen 99.995% (H_2) were used. The gases were flowed into the reaction chamber through the sequence of line tubing and mass flow controllers (MFC) which are used to control their flow rates. These MFCs operate at 0-200 standard cubic centimeter per minute (sccm) for N_2 and H_2 while 0-50 sccm for CH_4 .

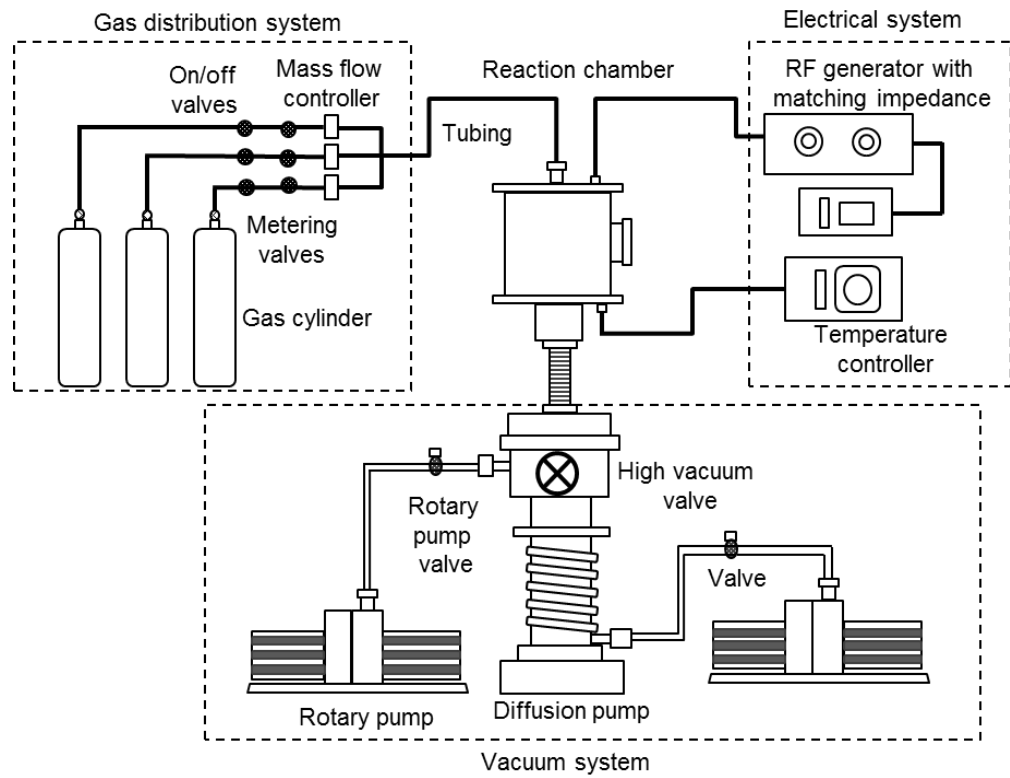


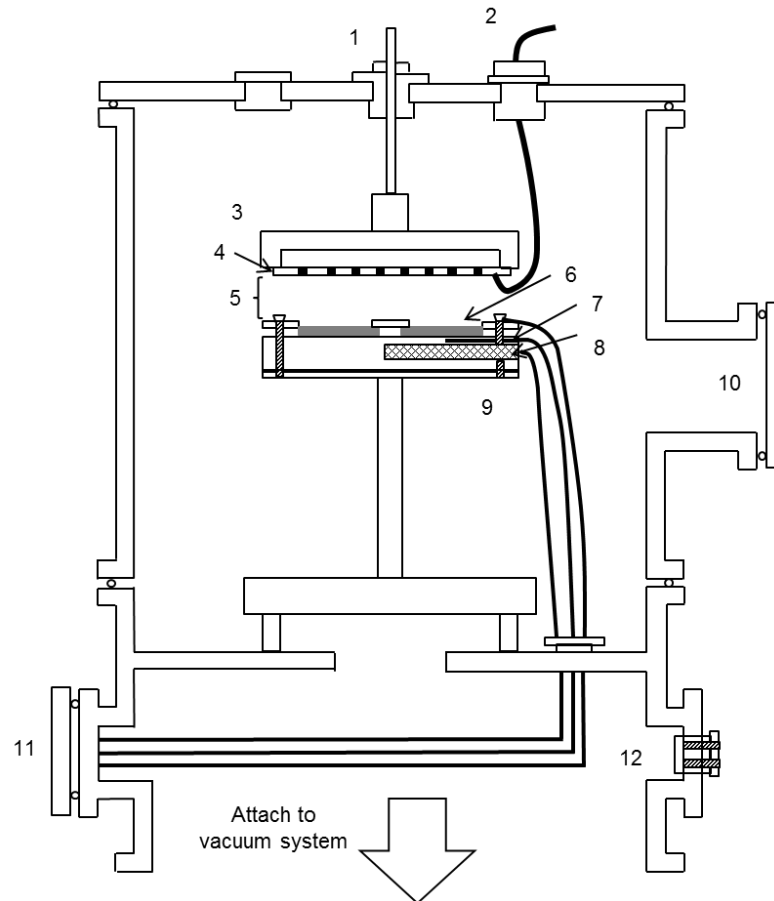
Figure 3.1: Schematic diagram of RFPECVD system.

The vacuum system consists of a water-cooled diffusion pump and a rotary pump connected to the reaction chamber via a bellows valve. The rotary pump is used for the initial rough pumping and also during deposition while the diffusion pump is used for fine pumping. Firstly, using the rotary pump, the reaction chamber is roughly

pumped to a base pressure of approximately at 3×10^{-3} mbar. During this time, the diffusion pump is warmed up for about 30 minutes once the desired pressure is achieved. The bellow valve direction of the pump is switched on and the pumping is continued till the chamber pressure reached approximately to 5×10^{-5} mbar. The rotary pump should be switched off immediately before the diffusion pump is operated to avoid backflow due to difference in pressure.

The electrical system consists of a RF generator with a matching impedance network, and also a temperature controller fitted with a heater power supply. The RF generator is connected to the reaction chamber via the matching impedance which balanced the different between impedance of the unit and the system. The substrate was heated using (400 W) Watlow firerod cartridge heater driven by the ac power supply, where the substrate temperature was measured using K-type thermocouple. The temperature was monitored and controlled using a thermocouple and temperature controller.

The main part in this RFPECVD system is the reaction chamber. Figure 3.2 shows the schematic diagram of this reaction chamber. This chamber is made from stainless steel. The RF generator and gas distribution system are connected to the upper part while the pumping system is attached to the bottom part of this chamber. The electrode is arrayed in a parallel plate configuration. The upper electrode is a shower head with holes size of about 1 mm and arrayed 1 cm apart. This electrode is connected to the RF generator and is insulated from the chamber using a teflon block. The bottom electrode which acts as the substrate holder, was electrically grounded and connected to the heating component. The legs of the substrate holder are insulated by teflon cylinder to avoid touching the body of the reaction chamber. Throughout this work, the distance between the top and bottom electrode is fixed at 1 cm.



- | | |
|---------------------------------|----------------------------------|
| 1. Gas shower head | 7. Thermocouple |
| 2. Upper electrical feedthrough | 8. Heater |
| 3. Teflon | 9. Substrate holder |
| 4. Shower head | 10. View port |
| 5. Electrode distance | 11. Lower electrical feedthrough |
| 6. Substrate | 12. Pressure gauge |

Figure 3.2: Schematic diagram of RFPECVD system reaction chamber.

3.3 Sample Preparation

3.3.1 Substrate Cleaning Procedures

The substrates were cleaved into rectangular pieces with dimension of 2.0 cm x 2.5 cm. The substrate cleaning is an important part in preparing the substrates for the film deposition. Small amount of contamination on the substrate may change the properties of the sample and also decrease the adhesion of the film onto the substrate. In this work, all samples were deposited onto silicon (Si) substrate.

Firstly, the Si substrate was rinsed in deionized water and then soaked in a solution of $\text{H}_2\text{O}:\text{H}_2\text{O}_2:\text{HCl} = 6:1:1$ for 10 minutes. Then, these substrates were soaked with deionized water in a beaker placed in an ultrasonic bath for 10 minutes. They were soaked again in a solution of $\text{H}_2\text{O}:\text{H}_2\text{O}_2:\text{NH}_4\text{OH} = 5:1:1$ for 1 minute. After the substrates were rinsed with deionized water, they were then immersed in a solution $\text{H}_2\text{O}:\text{HF} = 10:1$ for 1 minute. Finally, the substrates were rinsed with deionized water and immersed in ethanol and then acetone before they were dried in a stream of nitrogen gas and then placed in the deposition chamber. This whole process was done to remove impurities and the oxide layer on the surface of these Si substrates.

3.3.2 Pre-deposition Process

The deposition chamber was thoroughly cleaned to remove all the deposits left from the previous deposition process. Sand paper was used to remove the deposits on the steel surface inside the chamber. The surface was then thoroughly cleaned with acetone. The set up was assembled and the thermocouple and electrical connection were attached to the substrate holder. Four clean substrates were positioned on the substrate holder with a mask shown in Figure 3.3. The chamber was sealed and all the valves were closed before the system is ready to be pumped down.

The reaction chamber was evacuated in two phases using the rotary pump and sequentially using the diffusion pump to obtain a base pressure of 5×10^{-5} mbar. In the first phase, the chamber was evacuated together with the gas lines with all the valves and mass flow controllers fully opened. This is to ensure there is no leakage and also reduces the contamination due to residual gases in the lines. Once the desired pressure have been reached, the gas line valves were closed and rotary pump's valve was closed before the diffusion pump's bellow valve was fully opened. The chamber was further prepared until the pressure of about 10^{-5} mbar is achieved.

In this high vacuum condition, the substrates were heated to approximately 100°C . Once the high vacuum pressure and substrate temperature were stable, the pre-deposition substrate treatment is initiated. The bellow valve was closed and the rotary pump's valve is opened. Then, hydrogen gas was immediately flowed into the chamber. The hydrogen gas flow was maintained at 50 sccm. By adjusting the rotary pump's valve the deposition chamber was maintained at a pressure of 0.8 mbar. The RF generator was turned on and fixed at 60 W to carry out hydrogen plasma treatment on the substrate for 10 minutes. This process was done to further minimize substrate surface contamination.

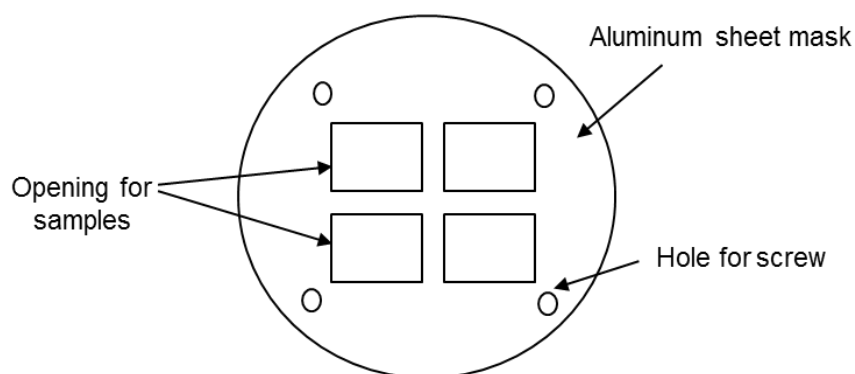


Figure 3.3: Top view mask of substrate holder.

3.3.3 Deposition Process

The film grown in this work consist of underlayer amorphous hydrogenated carbon, a-C:H films and carbon nitride films which were deposited onto these a-C:H underlayer; were grown by RFPECVD. Both configurations are shown in Figure 3.4. These a-C:H underlayers were deposited from pure methane (99.995%) plasma. Where there are variation in the a-C:H underlayer deposition, some of the parameter are fixed throughout this work. This include the flow rate, deposition pressure and substrate temperature of 20 sccm, 0.31 mbar and 100 °C, respectively. The CN_x films were grown on these a-C:H underlayer from the RF discharge of gas mixture of pure methane (CH_4) and nitrogen (N_2) gas. The deposition parameters are fixed throughout this work. The flow rate of the CH_4 and N_2 were fixed at 20 and 50 sccm respectively. The RF power was fixed at 60 W while the deposition pressure was fixed at 0.58 mbar. Single a-C:H underlayers were also fabricated to study the underlayers themselves.

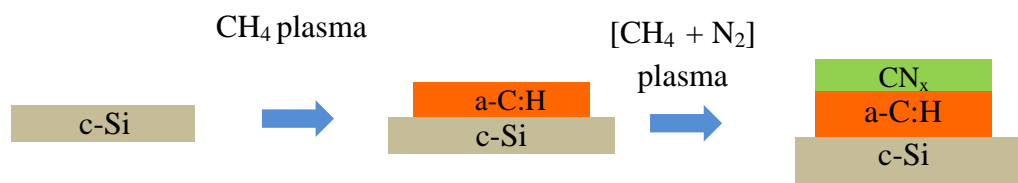


Figure 3.4: Single a-C:H underlayer deposited on Si substrate and CN_x film deposited on a-C:H underlayer prepared by RFPECVD.

Three sets of a-C:H underlayer and the subsequent CN_x thin films were prepared. In the first set, a-C:H underlayers were deposited at different deposition duration of 5, 10, 15 and 30 minutes at RF power of 60 W. CN_x films was deposited on these a-C:H underlayers. In set 2, a-C:H underlayers were prepared at different RF power of 30, 40, 50, 60, 80 and 100 W and deposited for 10 minutes. The last set consists of a-C:H underlayers deposited at fixed RF power of 100 W and deposition time of 10 minutes; and these are subsequently treated in hydrogen plasma for different duration of 3, 5 and 10 minutes. The hydrogen plasma was produced from hydrogen at flow rate 50 sccm. Subsequently CN_x films were deposited onto these films and the effects of varying each deposition condition were studied in terms of the a-C:H underlayer and the CN_x formation. The chart of the set of samples prepared in this work is shown in Figure 3.5. Table 3.1 summarizes the parameters for a-C:H layer and CN_x film.

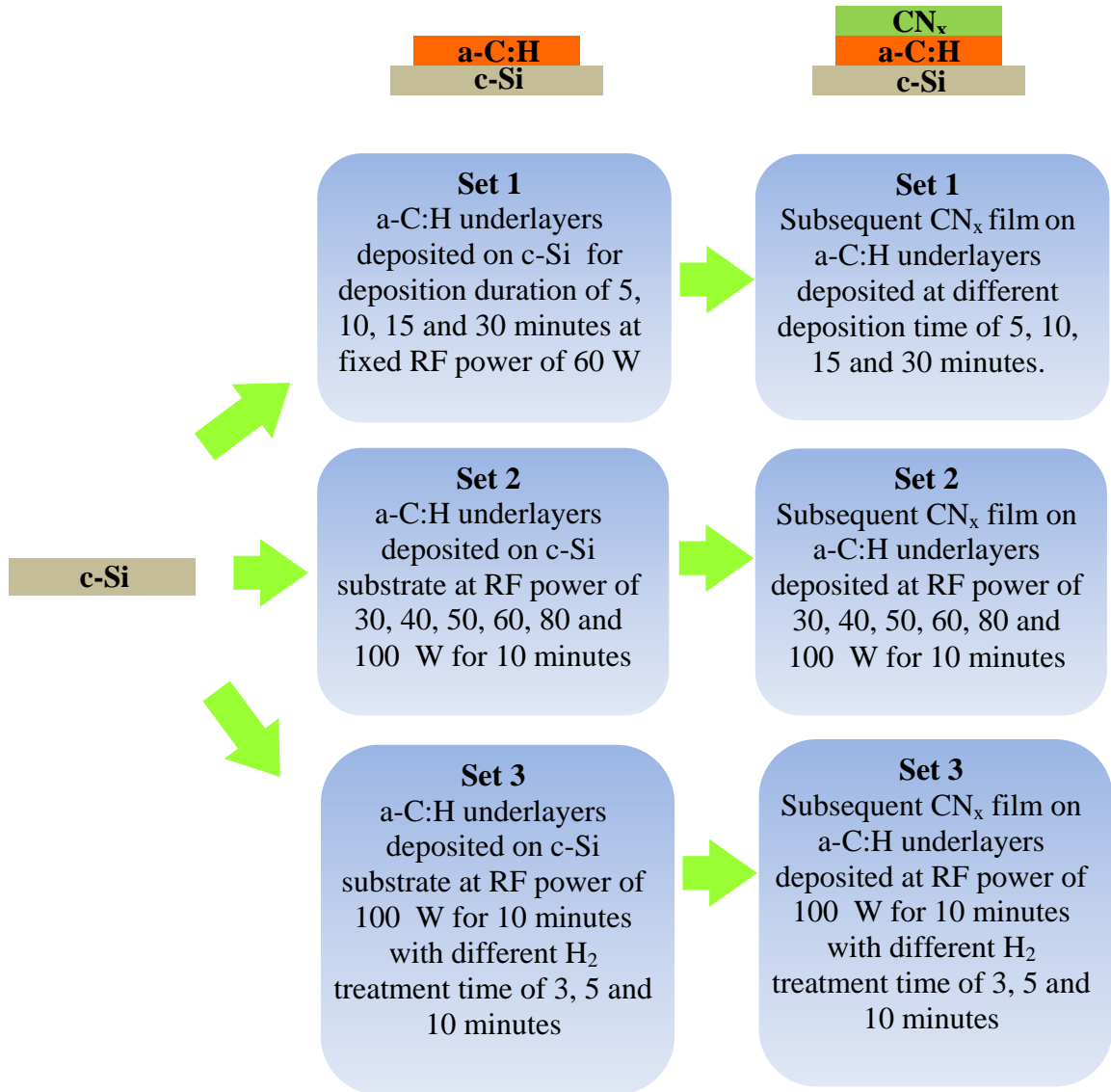
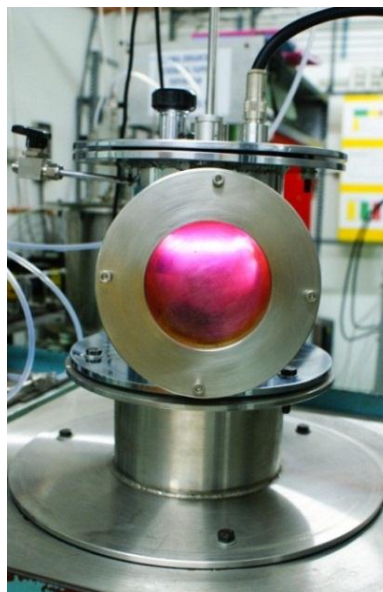


Figure 3.5: Chart of sample preparation.

Table 3.1: Deposition parameter of a-C:H layer and CN_x nanostructures.

Films	a-C:H			CN _x
	Set 1	Set 2	Set 3	
Deposition time (minutes)	0, 5, 10, 15 and 30	10	10	90
RF power (W)	60	30, 40, 50, 60, 80 and 100	100	60
Hydrogen plasma treatment	-	-	0, 3, 5 and 10 minutes	-
Gas source and flow rate (sccm)	CH ₄ 20	CH ₄ 20	CH ₄ 20	CH ₄ +N ₂ 20 + 50
Pressure (mbar)	0.3	0.3	0.3	0.6
Deposition temperature (°C)	100	100	100	100

The RF generator was turned on to ignite the plasma once the substrate temperature has stabilized. The plasma discharge is depicted in Figure 3.6. Carbon nitride films were deposited for 90 minutes on the a-C:H coated c-Si substrates. For comparison a set of CN_x films was deposited on bare c-Si substrates. Throughout the deposition, the chamber pressure, substrate temperatures and gas flow rates were regulated at their fixed value.

**Figure 3.6:** Plasma discharge during deposition process.

3.3.4 Post-deposition Process

At the end of the deposition time, the RF generator and heater power supply were turned off. The chamber was continually pumped down to allow the sample to cool down slowly to room temperature under vacuum.

3.4 Analytical Techniques

3.4.1 Atomic Force Microscopy

Atomic Force Microscopy (AFM), a scanning probe microscopy technique was established in 1986 by Binnig and co-workers. This instrument produces atomic scale images of the surface topography of conducting and non-conducting surfaces. Figure 3.7 shows a schematic diagram of AFM. Thin film sample was placed on a piezoelectric scanner under a stationary sharp tip attached to a flexible cantilever. The instrument works by measuring deflection from the cantilever as it is scanned across the surface of the sample. The cantilever deflection detection system is used to retain a constant deflection angle by adjusting the displacement of piezoelectric scanner tube in z-direction which moves upward and downward. This allows the changes of surface morphology of the sample when scanning along the x and y-direction to be recorded in the form of a topographic map. The sensitivity of the cantilever is determined by its length and type of material that makes up the tip. Commonly, SiN_3 is selected because SiN_3 shows high hardness and durability and can be mass produced using chemical vapour deposition while the tip could be induced using microelectronic lithography.

There are 3 modes of measurement usually used in AFM. This includes contact, non-contact and tapping modes. The choice of modes depends on the type of sample to be scanned and also resolution. High resolution surface topography could be obtained by contact mode while non-contact mode prevents sample damage. On the other hand,

tapping mode is preferred because it combines the advantages of both contact and non-contact modes. This minimizes damage of the film surface while producing high resolution image. A VEECO Dimension 3000 atomic force microscope as shown in Figure 3.8, was used to determine the surface roughness and morphological properties of the a-C:H underlayer.

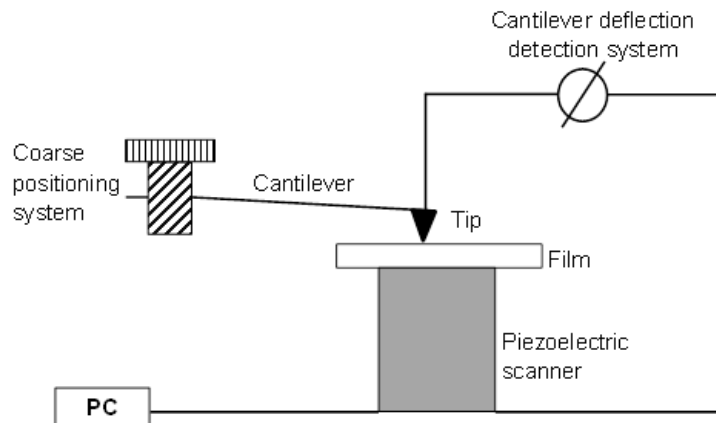


Figure 3.7: Schematic diagram of AFM



Figure 3.8: VEECO Dimension 3000 atomic force microscope.

An a-C:H underlayer was scanned within an area of $5 \times 5 \mu\text{m}^2$. Figure 3.9 (a) and (b) show a typical surface morphological image and the corresponding roughness analysis respectively.

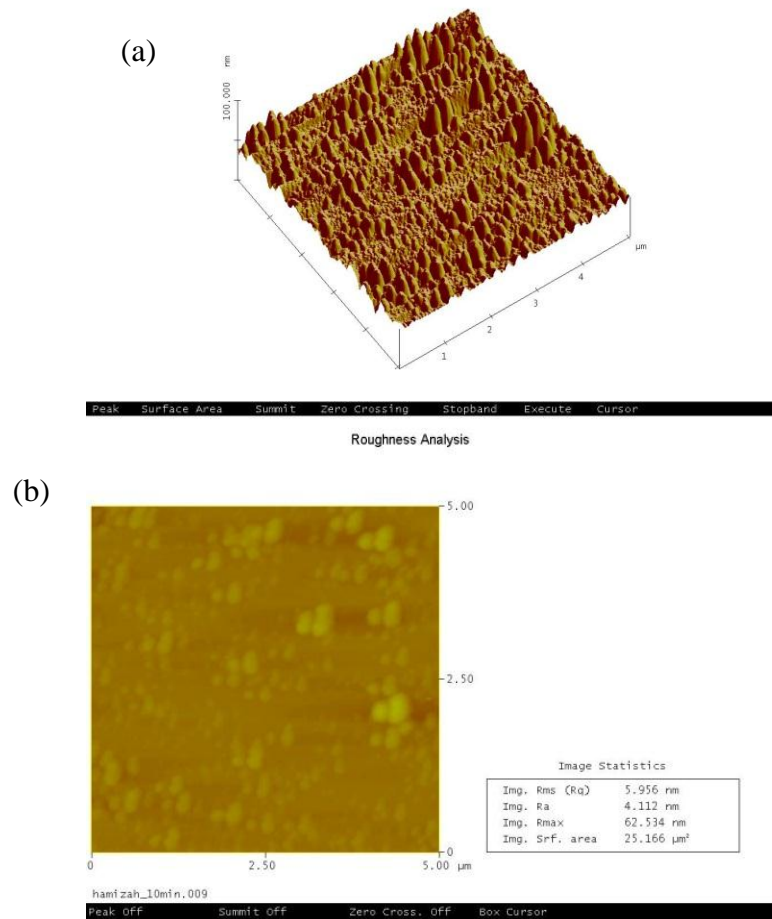


Figure 3.9: Surface morphological (a) and roughness analysis (b) of a-C:H underlayer deposited by RFPECVD at 10 minutes.

3.4.2 Profilometer

The growth rate of the a-C:H underlayer was calculated from the film thickness obtained using a KLA TENCO P-6 profilometer. The profilometer is shown in Figure 3.10. The thickness is measured from the height difference between the substrate surface and the carbon layer. Figure 3.11 shows a typical surface profile measurement used to determine the thickness of the a-C:H underlayers. The thickness was calculated at different positions and average of the thickness was obtained.

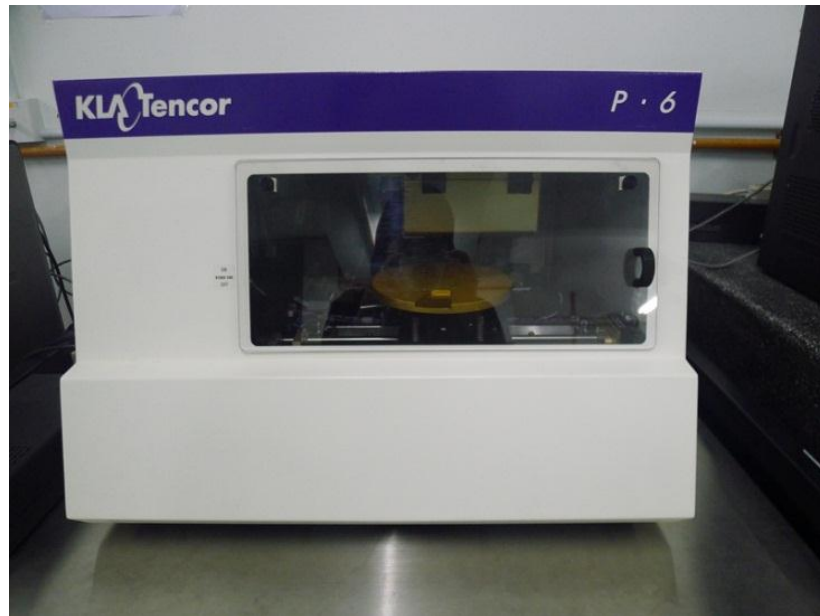


Figure 3.10: KLA TENCO P-6 profilometer.

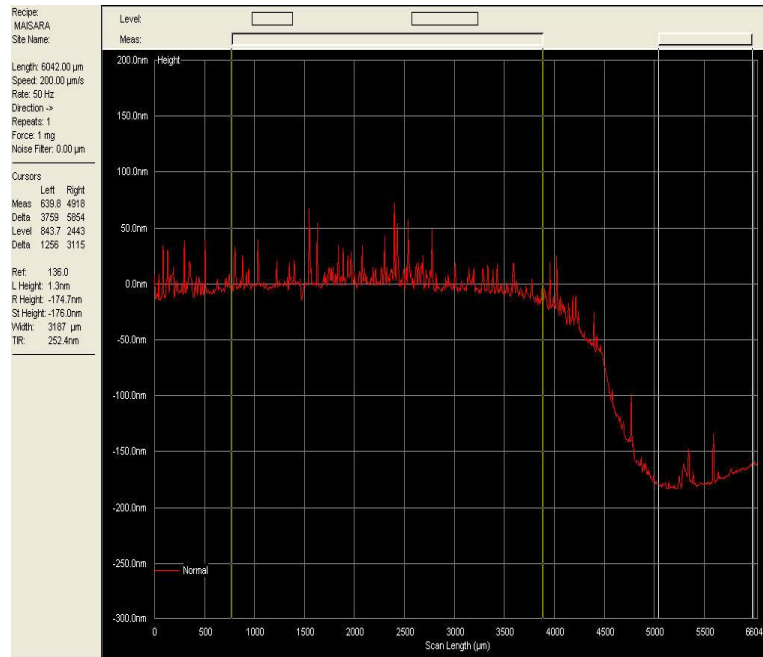


Figure 3.11: Data observed from profilometer for film deposited at 100 W RF power with 3 minutes hydrogen treatment process.

3.4.3 Scanning Electron Microscopy

High resolution surface and cross section of images of the CN_x films were obtained from a FEI Quanta 200 field emission scanning electron microscope (FESEM). The FESEM is shown in Figure 3.12. The FESEM operates using a beam of electron which is scanned across a sample. During the scanning process, the specimen is bombarded with electrons. The electrons may be elastically reflected or absorbed by the sample. Secondary electrons and x-rays can be produced from the specimen surface if the incident beam is energetic enough. This causes a slight energy loss and path change in the incident electrons and ionization of electron in the specimen atom. Several secondary electrons can be produced by each of the incident electrons and all these effects can be used to produce an image.



Figure 3.12: FEI Quanta 200 field emission scanning electron microscope.

The thickness of CN_x films was obtained from the cross sectional images. The thickness was calculated from the vertical height of the film perpendicular to the underlayer surface for at least 50 points from each image, and then the average was calculated. Growth rate is obtained by dividing the film thickness with the deposition duration. An example of surface and cross section images of CN_x films are shown in Figure 3.13.

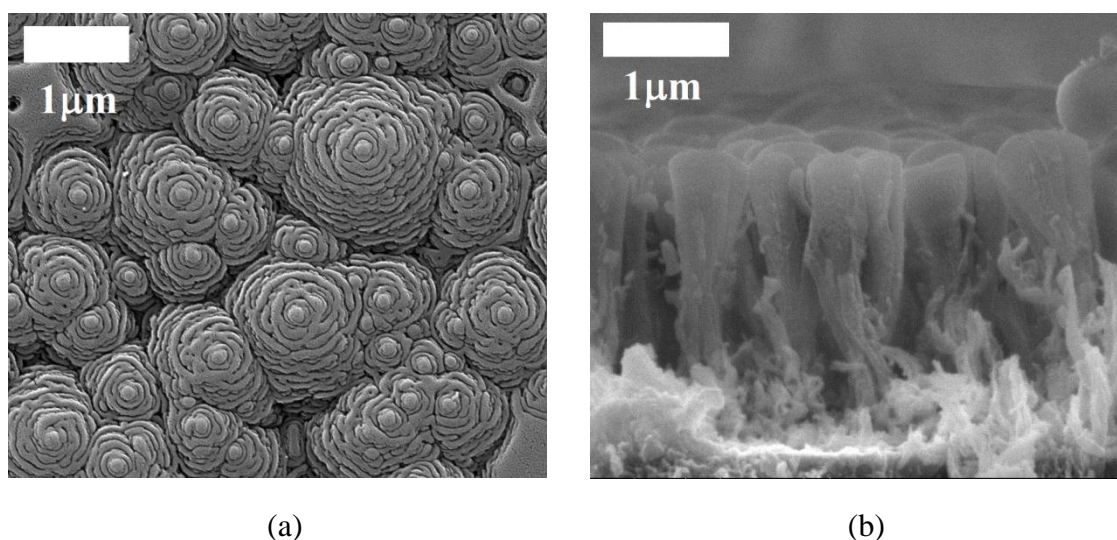


Figure 3.13: Surface (a) and cross section (b) images of CN_x film deposited on a-C:H underlayer prepared at RF power of 50 W.

3.4.4 Fourier Transform Infrared Spectroscopy Measurement

Fourier Transform Infrared (FTIR) spectroscopy, is used to determine the chemical bonding structure and molecule content in the a-C:H underlayer and CN_x thin film. The FTIR technique is used to identify the absorption of various bonding of the a-C:H and CN_x films. This was done by measuring the infrared radiations by the sample under transmission mode. Molecular vibrations give rise to IR bands only if they cause a change in the dipole moment of the molecule which includes stretching, wagging, rocking and bending. The normal way to interpret an IR spectrum is to identify functional group regions, then to note any unusually strong bands or particularly prominent patterns in the fingerprint region. These functional groups could be identified from the spectra with reference to those obtained from literature. Figure 3.14 shows the schematic diagram of Fourier Transform Infrared Spectrometer. The interferogram is a complex signal produced from an optical pathway pattern. This signal is generated by combination of two beams oriented toward the sample by a beam splitter. The sample absorbs the beam that passes through at specific wavelength and the computer compares the signal produced with a reference laser beam. The resulting interferogram shows all

the information in an imaginary one time-domain signal. A mathematical process called Fourier transform is applied by the computer to produce the resulting infrared spectrum.

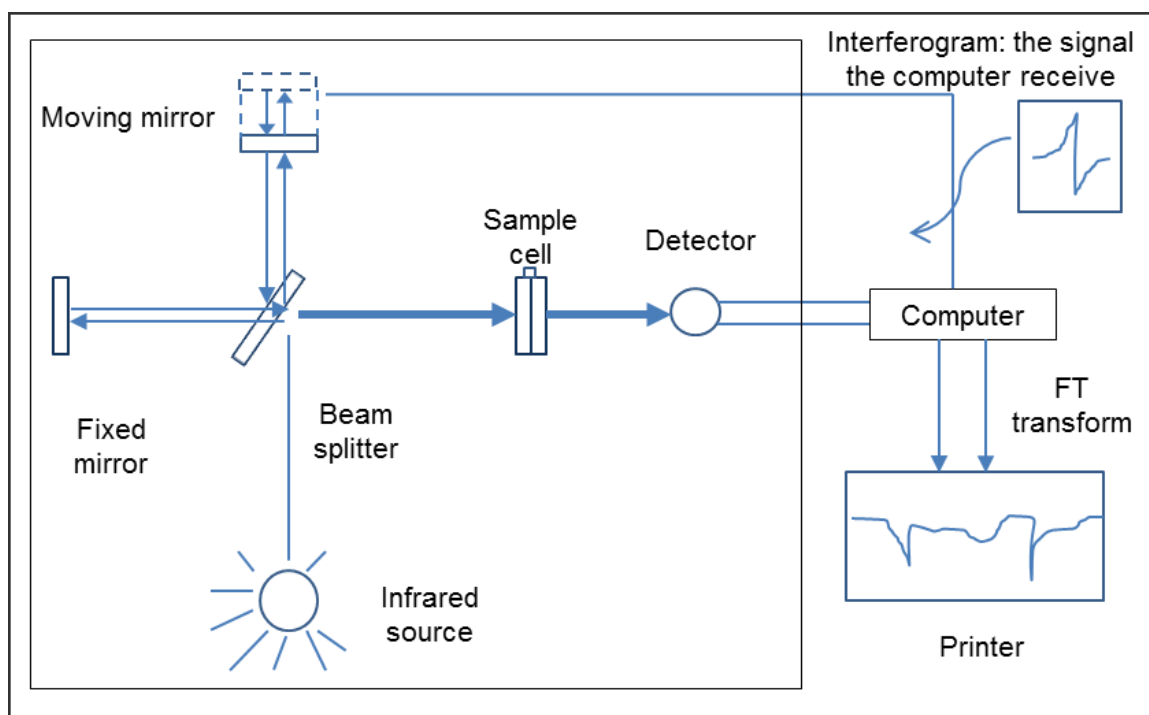


Figure 3.14: Schematic diagram of Fourier Transform Infrared Spectrometer.

FTIR measurements were done using a Perkin Elmer System 2000 FTIR spectrometer in transmission mode as shown in Figure 3.15. The sample deposited on Si substrate was scanned in the range of $400\text{--}4000\text{ cm}^{-1}$. A blank Si substrate was used as background. The spectrum is converted to absorption spectrum by normalizing it to film thickness.



Figure 3.15: The Perkin Elmer System 2000 FTIR spectrometer.

Figure 3.16 shows a typical FTIR spectrum of a-C:H underlayer while Figure 3.17 shows a typical FTIR spectrum for CN_x nanostructures. These spectra are divided into 2 and 3 regions at wavenumber respectively of 1300-1800, 2000-2300 and 2800-3700 cm^{-1} . Each region is assigned to bonds accordingly as shown in Table 2.1.

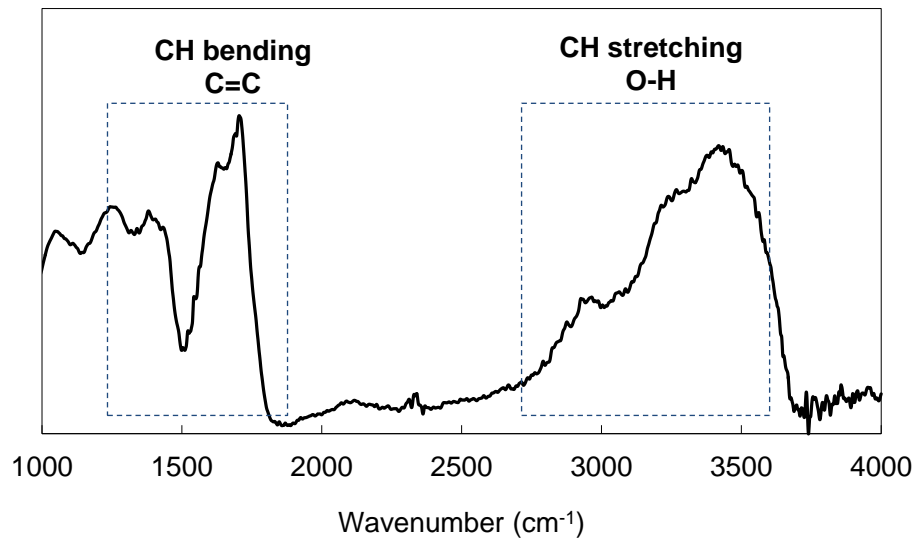


Figure 3.16: FTIR spectrum of a-C:H underlayer.

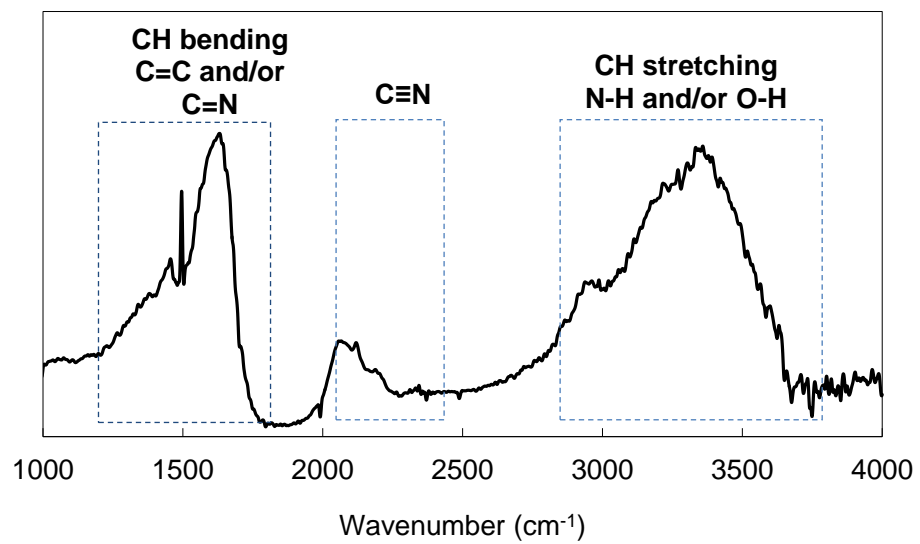


Figure 3.17: FTIR spectrum of CN_x nanostructures.

The spectrum was deconvoluted according to those proposed by other researchers (Mutsukura and Akita 1999; Fanchini et al. 2005; Li et al. 2006) to obtain the integrated intensity of the absorption spectra. This integrated intensity can be determined from the following relation.

The absorption coefficient is given by equation 3.1.

$$\omega = \frac{1}{d} \ln \left(\frac{100}{\%T} \right) \quad (3.1)$$

where d is the film thickness and T is the transmittance.

The integrated intensity of the absorption band representing a particular bonding configuration is obtained using equation 3.2.

$$I = \int \frac{\alpha(\omega)}{\omega_0} d\omega \quad (3.2)$$

The Gaussian or Doppler line shape was used to deconvolute the component peak from the absorption spectrum. This can be expressed using

$$\alpha(\omega) = \alpha_{max} \exp \left\{ \frac{-4(\ln 2)(\omega - \omega_0)^2}{(\Delta\omega)^2} \right\} \quad (3.3)$$

with

$$\alpha_{max} = \frac{2(\ln 2)^{1/2} S_{band}}{\pi^{1/2} (\Delta\omega)} \quad (3.4)$$

and

$$S_{band} = \int \alpha(\omega) d\omega \quad (3.5)$$

S_{band} , ω , $\alpha(\omega)$ and ω_0 are the area under the spectrum, the full width half maximum (FWHM) of the absorption peak, the maximum absorption coefficient and the position of absorption peak respectively. Equation 3.2 can be rewritten in the form of

$$y = A \exp(-Bx) \quad (3.6)$$

where A , B and x can be expressed in the following form

$$y = \alpha(\omega) \quad (3.7)$$

$$x = (\omega - \omega_0)^2 \quad (3.8)$$

$$A = \frac{B^{1/2} S_{band}}{\pi^{1/2}}, \text{ or } A = \frac{2(\ln 2)^{1/2} S_{band}}{\pi^{1/2} (\Delta\omega)} \quad (3.9)$$

$$B = \frac{4(\ln 2)}{(\Delta\omega)^2} \quad (3.10)$$

Performing natural logarithm on both sides of equation 3.6,

$$\ln y = \ln A - B(\omega - \omega_0)^2 \quad (3.11)$$

From equation 3.2, the integrated intensity can be expressed as

$$I = \frac{S_{band}}{\omega_0} \quad (3.12)$$

Figure 3.18 shows an example of deconvolution of FTIR absorption peaks obtained for CN_x nanostructures in wavenumber region of $1950-2350 \text{ cm}^{-1}$. These peaks were deconvoluted using Gaussian fitting calculated by OriginPro 8.1 program.

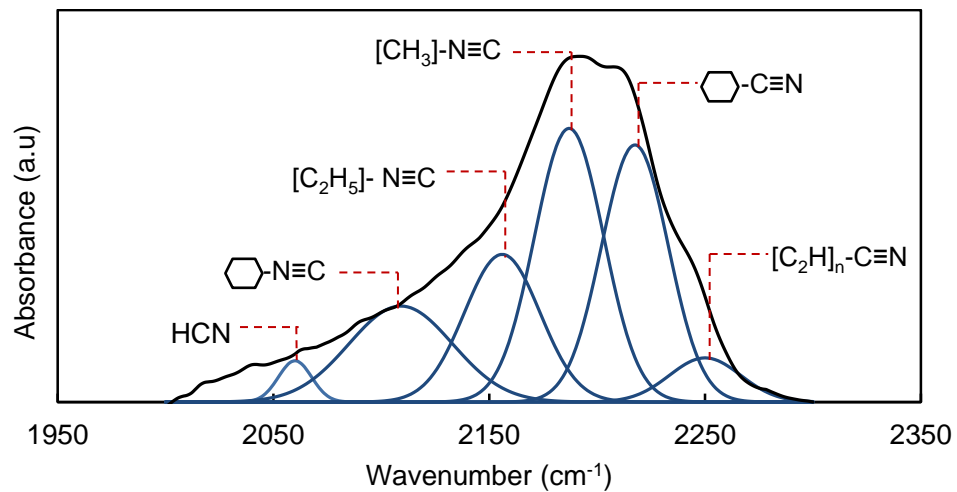


Figure 3.18: Example of deconvolution FTIR absorption peaks of a-C:H underlayer and CN_x nanostructures in wavenumber region of $2000-2300 \text{ cm}^{-1}$ (Mutsukura 2001).

3.4.5 Raman Spectroscopy

Raman Spectroscopy is used to study the vibrational, rotational and other low frequency transition properties of materials. The Raman effect occurs when frequency of monochromatic light changes upon interaction with a sample due to an inelastic scattering of the monochromatic laser source. The sample absorbs the photon from the laser source and reemitted photon and the difference in frequency of incident and emitted photon provides information about the vibrational and rotational transition in molecules.

Figure 3.19 shows the Renishaw inVia Raman Microscope and in this work measurements were carried out by using Helium-Cadmium laser with excitation wavelength of 325 nm and grating slit of 2400 lines/mm for film deposited on c-Si substrate. Raman shift was determined in wavenumber range of 1000-2500 cm^{-1} measured at an exposed time of 10 s at laser power of approximately 0.2 mW.



Figure 3.19: The Renishaw inVia Raman Microscope.

The example of typical Raman spectra for a-C:H underlayers is shown in Figure 3.20. The example is for films prepared at different deposition duration showing the presence of D and G bands in range of 1350-1380 cm^{-1} and 1550-1600 cm^{-1} respectively. For the deconvolution of D and G bands, the spectra were initially corrected by removing the PL background baseline as shown in Figure 3.20 (a). The corrected spectra are then deconvoluted using standard Gaussian fitting computed using Origin Pro 8.1 as shown in Figure 3.20 (b). From the fitting, the clustering of the sp^2 phase, bond disorder, presence of sp^2 rings or chains and sp^2/sp^3 ratio of the films were studied.

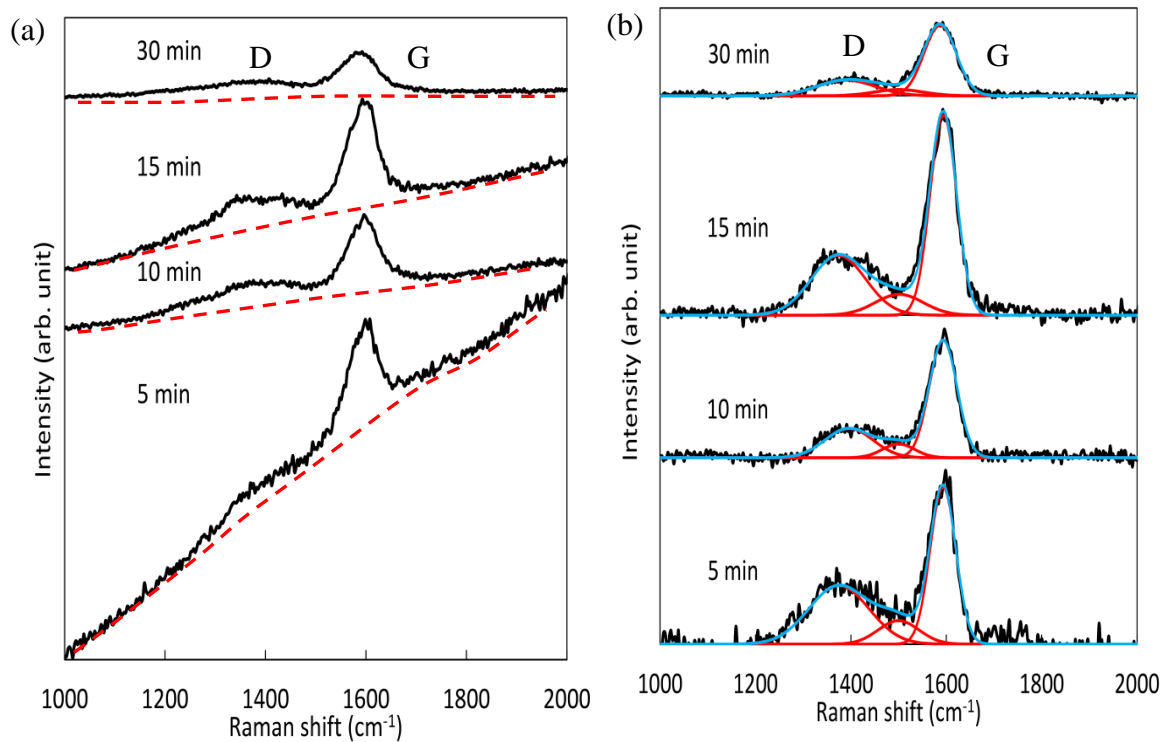


Figure 3.20: (a) Raman spectra with the baseline and (b) corrected Raman spectra with the Gaussian fitting D and G bands.

3.4.6 Auger Electron Spectroscopy

Auger Electron Spectroscopy (AES) have been used widely to determine the composition of the surface layer of a film. This measurement is derived from the phenomenon of emission of low energy electron by Auger process when electrons with energies of 3-20 keV are incident on a sample, that is electrons from atoms in the sample could be ejected producing a photoelectron and an atom with a core hole. The atom then relaxes via the transition of electrons with lower binding energy into the core hole. Energy released from this relaxation can be converted into an X-ray or emission of an electron. The emitted electron due to this relaxation process is called an Auger electron. Schematic diagram of this Auger process is summarized in Figure 3.21. With the emission of the Auger electron, the atom is left in a doubly ionized state. The energy of the Auger electron is characteristic of the element that emits it, and can thus be used to identify the element. The short inelastic mean free path of Auger electrons in solids ensures the surface sensitivity of its measurement. AES is a popular technique for determining the composition of the top few layers of a surface. It cannot detect hydrogen or helium, but is sensitive to all other elements, being most sensitive for low atomic number elements.

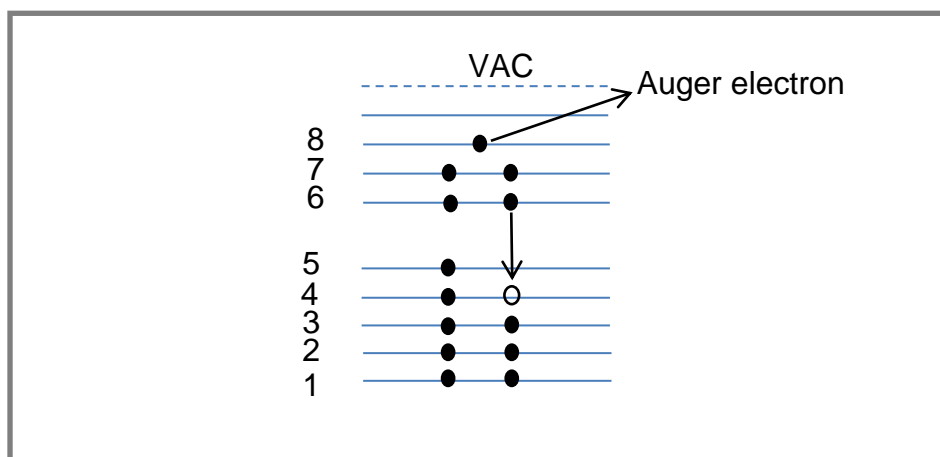


Figure 3.21: Schematic diagram of Auger electron process.

In this work, Auger electron was measured by JAMP-9500F Field Emission Auger Microprobe, as shown in Figure 3.22. Etching and measure cycles were carried out to obtain reliable, consistent result, since the top surface of the film tends to have contamination. The etching process is done by sputtering of high energy heavy ion beam in which Ar^+ ions was used to impinge the surface of the film. Figure 3.23 illustrates the typical AES spectra of CN_x nanostructured films. In this example, the films are prepared at different deposition duration for the a-C:H underlayer. From the quantitative analysis, the nitrogen to carbon content ratio was calculated.



Figure 3.22: JAMP-9500F Field Emission Auger Microprobe.

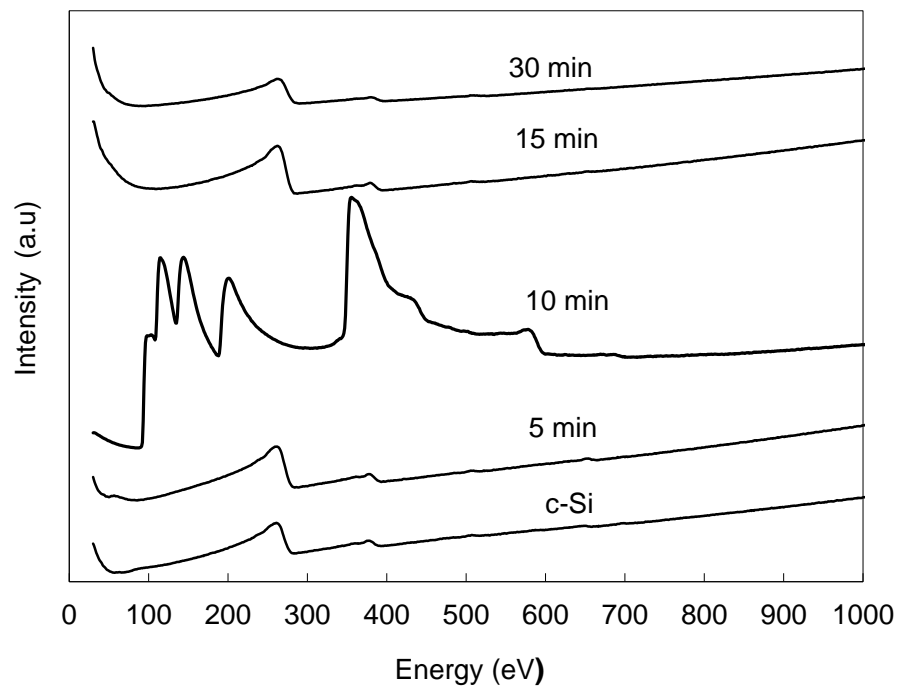


Figure 3.23: AES spectra variation of CN_x prepared on different deposition duration of a-C:H underlayer and bare c-Si substrate.

CHAPTER 4 : EFFECTS OF HYDROGENATED AMORPHOUS CARBON UNDERLAYER ON THE FORMATION OF CARBON NITRIDE NANOSTRUCTURES: RESULTS, ANALYSIS AND DISCUSSION

4.1 Introduction

This chapter presents the experiment results, analysis and discussion related to the study of hydrogenated amorphous carbon (a-C:H) thin films used as the underlayer film in the subsequent fabrication of carbon nitride nanostructures (ns-CN_x). These films were deposited using radio frequency plasma enhanced chemical vapour deposition (RFPECVD) from the precursors methane and nitrogen gases. For the a-C:H underlayers, their growth rate, surface roughness, chemical bonding and structural properties were studied. Subsequently, ns-CN_x were grown directly onto these a-C:H underlayer films. These ns-CN_x/a-C:H films were studied in terms of their surface and cross section images, growth rates, elemental composition and bonding properties.

This exploratory study focuses on three different aspects of the a-C:H underlayer growth and treatment. The first aspect looks into the effects of growth duration on these underlayer films, then the effects of the morphology of the underlayer on the formation of the ns-CN_x were studied. While the deposition time duration is varied, other critical deposition parameters such as the RF power, gas ratios, deposition temperatures and pressures, were kept constant. These critical parameters are known to significantly influence the structure of the film and thus it is expected that by keeping them constant throughout the deposition, the bulk structure of the films themselves should remain constant. This may enable studies of the growth and surface morphology to be scrutinized.

The second part looks into one of these critical deposition parameters, namely the effect of applied RF power on the deposition of the a-C:H underlayer and corresponding ns-CN_x. This was carried out while keeping the rest of the parameters constant, including the deposition duration. The third part looks into a totally different aspect. This involves the effect of hydrogen treatment onto a particular a-C:H underlayer sample. The as-deposited sample chosen exhibited the smoothest surface. The purpose of the treatment is to determine the potential of using surface treatment to alter the a-C:H surface and subsequently to produce different ns-CN_x structures.

In each part, the results and discussion were first focused on the characterization of the a-C:H underlayer films, followed by the characterization of the subsequent formation of ns-CN_x. The discussion in these part includes the correlation of the properties of the a-C:H underlayers and the structure of the ns-CN_x. Figure 4.1 summarizes the methodology and variations in the parameters involved in the modification of the a-C:H underlayer.

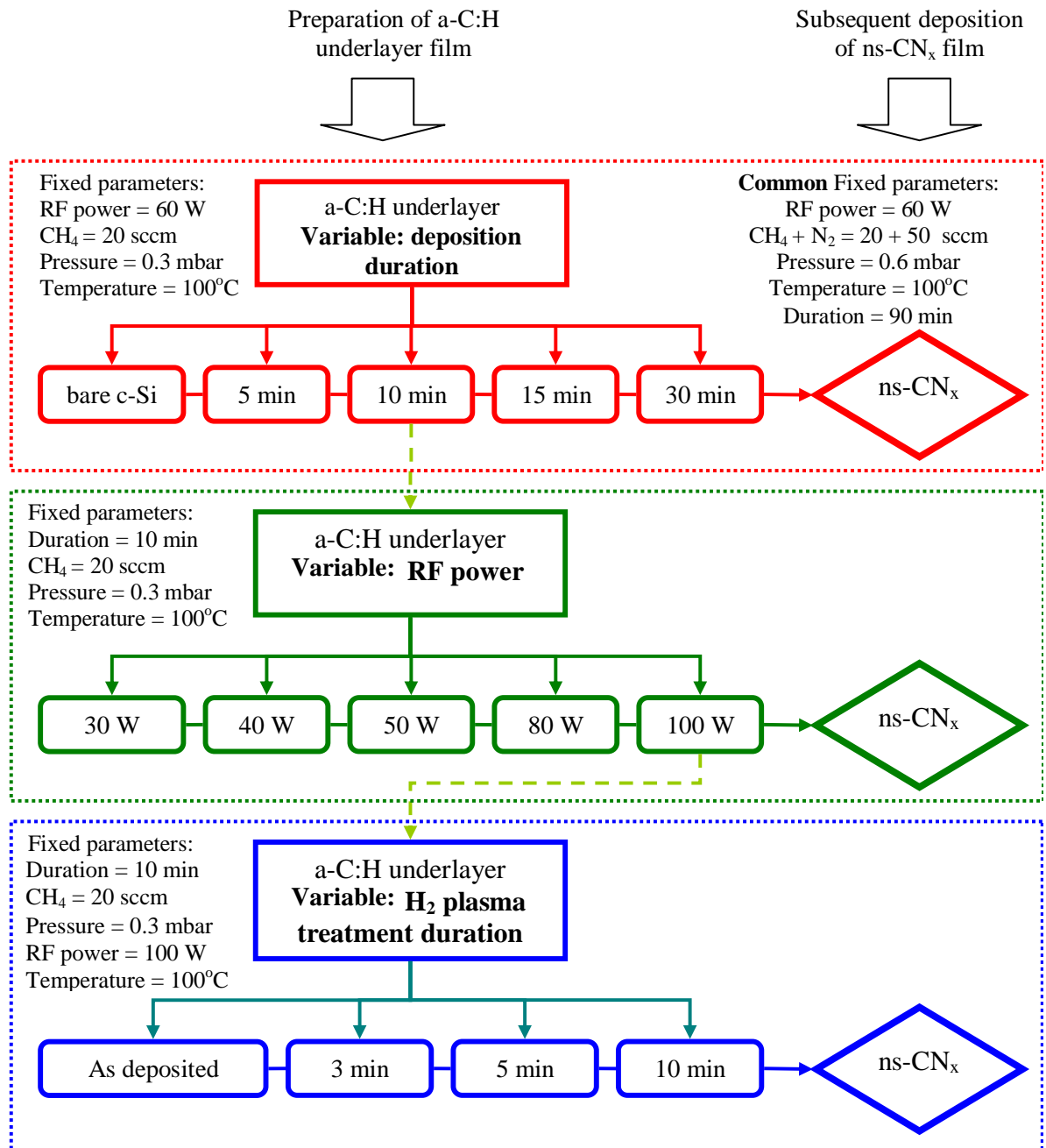


Figure 4.1: Summary of the methodology and variations in film preparation parameters.

4.2 Effects of Deposition Time Duration of a-C:H Underlayer and Resulting CN_x / a-C:H Formation

The first study focuses on the effects of different deposition time duration on the properties of a-C:H underlayers and thus its effects on the properties of the ns- CN_x . Five sets of samples are prepared where the deposition duration for a-C:H underlayers was varied at 5, 10, 15, 30 minutes, together with a CN_x prepared on bare c-Si. The growth rate, morphology, chemical bonding properties and composition of the films were studied.

4.2.1 Effects of Deposition Time Duration on a-C:H Underlayers

4.2.1.1 *Growth rate of a-C:H underlayers*

The thickness of these a-C:H underlayers were determined from surface profiler measurement. Figure 4.2 presents the variation of thickness and deposition rate of a-C:H underlayer deposited as a function of deposition time duration (t_D). The thickness of the a-C:H underlayers increase gradually at t_D up to 10 minutes, and subsequently increased linearly up to t_D of 30 minutes. The growth rates of these a-C:H films were calculated from the thickness. The growth rate decreased slightly when t_D was increased from 5 to 10 minutes and then, with further increase in t_D an almost constant increase in the growth rate was observed.

The growth rate of the a-C:H underlayers by RFPECVD is dependent on the number of nucleation sites present for the diffusion of carbon growth radicals from the plasma. The creation of the nucleation sites is mainly contributed by hydrogen etching effects and/or ion bombardment and abstraction process by CH_3 radicals. These

effectively break weak C-C bonds or H terminated bonds (Si-H on the c-Si substrates or C-H bonds), creating dangling bonds which allowed C growth radicals to bond onto the film. The slight decrease in growth rate for the film deposited at t_D of 10 minutes indicates that the rate of nucleation sites formation was larger than the rate of diffusion of C growth radicals onto these nucleation sites. Longer deposition duration increased the number of growth radicals reaching the growth sites thus increased the growth rate of the film.

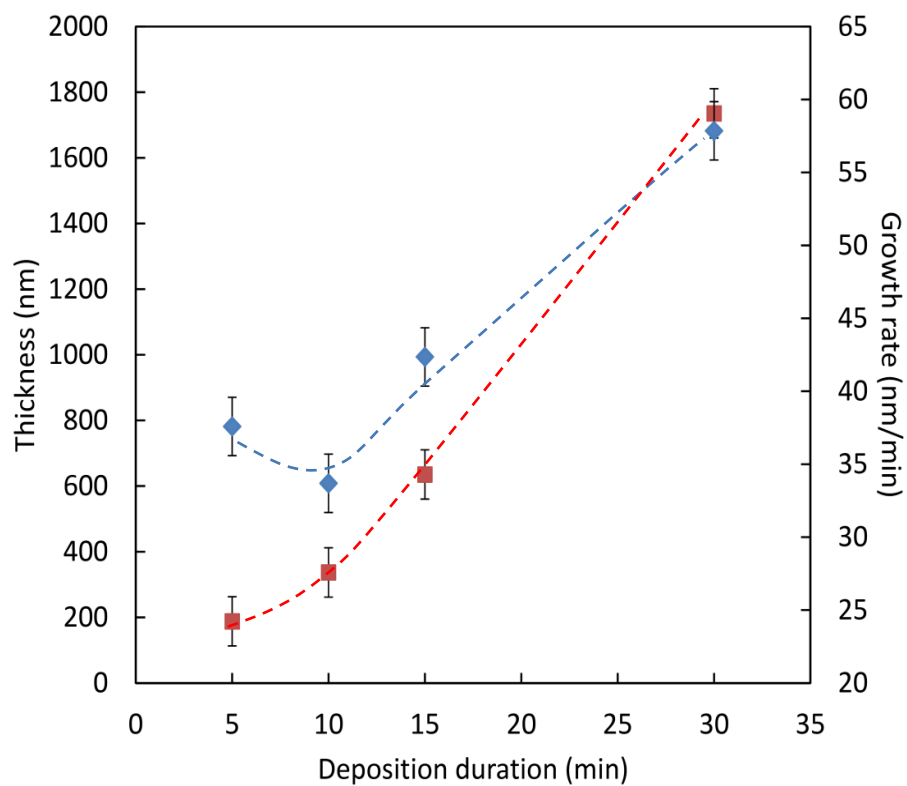


Figure 4.2: Thickness (■) and growth rate (◆) of a-C:H underlayer deposited by RFPECVD for different deposition time duration. The line is only an eye-guide.

4.2.1.2 Surface roughness and surface morphology of a-C:H underlayers

The morphology and surface roughness of the a-C:H underlayer films were determined from AFM measurements. The AFM surface images of the a-C:H underlayer are shown in Figure 4.3, while the variation of the corresponding surface roughness as a function of t_D is shown in Figure 4.4.

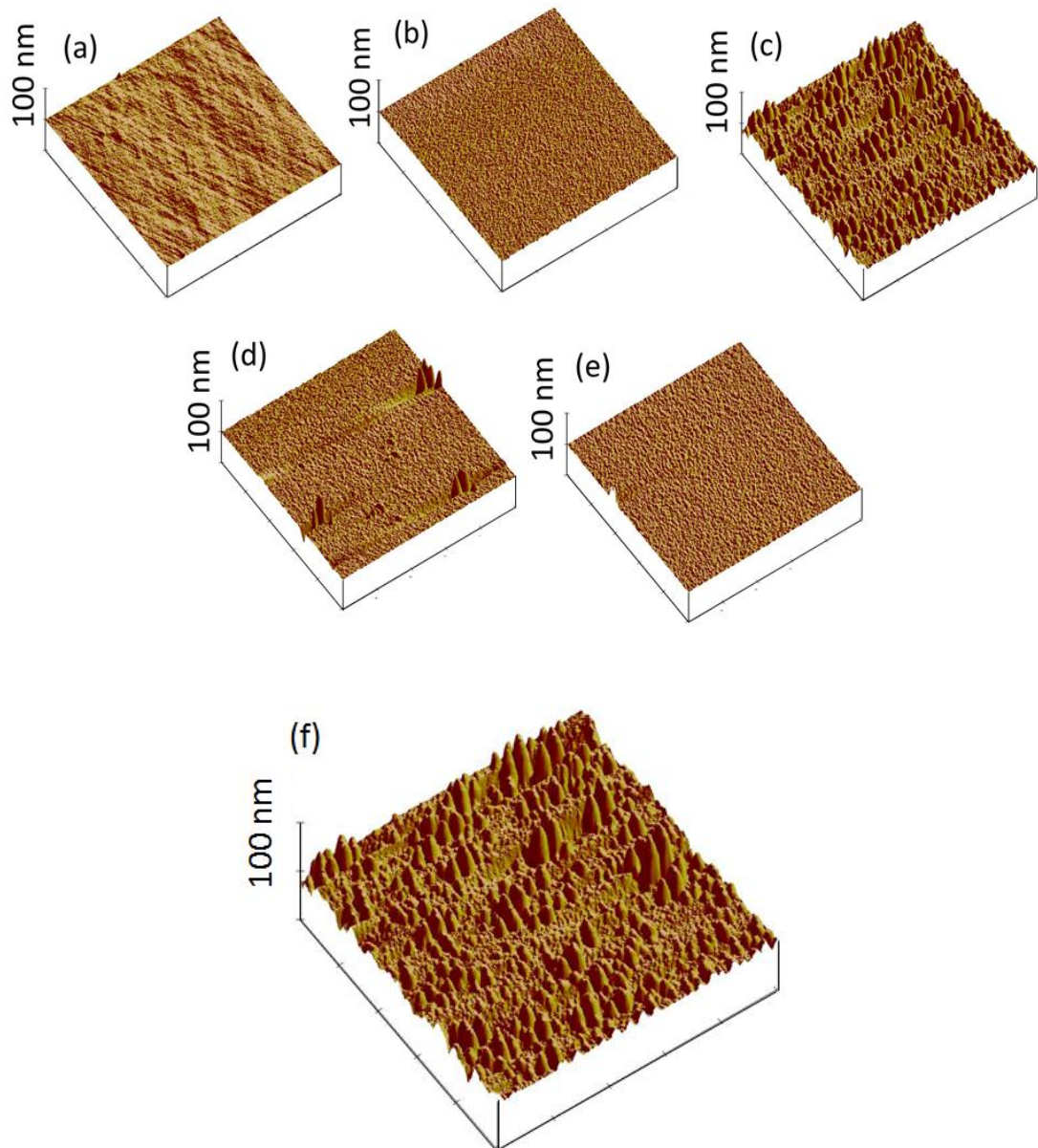


Figure 4.3: AFM surface morphology of (a) bare c-Si, a-C:H underlayers deposited for t_D of (b) 5, (c) 10, (d) 15, (e) 30 minutes and (f) the high magnification of a-C:H underlayer deposited at 10 minutes.

The surface roughness increases to maximum for the film deposited at t_D of 10 minutes while that of 5 and 30 minutes remained almost the same as bare c-Si. The maximum surface roughness for film deposited at t_D of 10 minutes is consistent with the AFM surface morphology seen in Figure 4.3 (c) where the surface roughness is contributed by the formation of what appear to be islands of broad tip cone-like structures protruding vertically on the substrate surface. Magnification of Figure 4.3 (c) is shown in Figure 4.3 (f). With the further increase in t_D from 10 minutes to 30 minutes, the cone-like structures appears to decrease and then disappear altogether resulting in the smooth film at t_D of 30 minutes. This corresponds to a sharp decrease in surface roughness from t_D 10 minutes to 15 minutes and then a gradual decrease from 15 minutes to 30 minutes as seen in Figure 4.4.

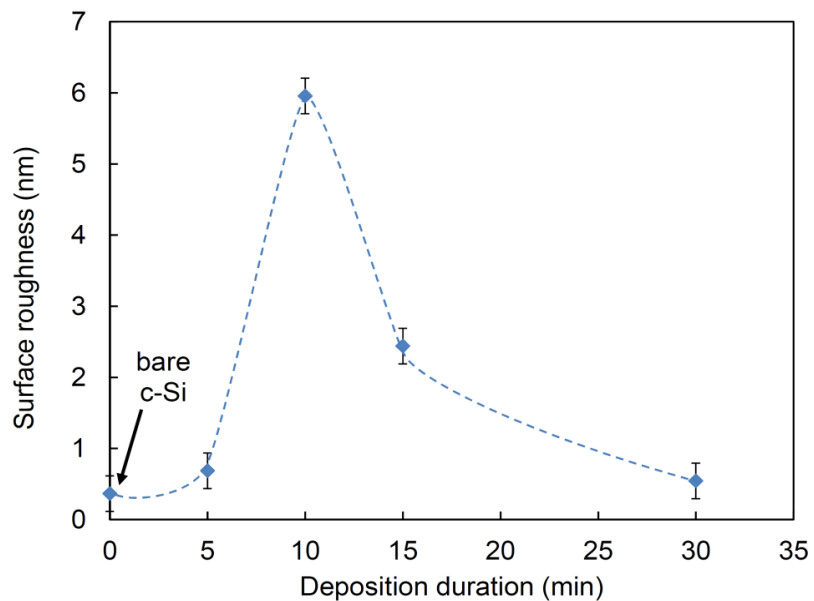


Figure 4.4: Variation of surface roughness of bare c-Si and a-C:H underlayers deposited at 5, 10, 15 and 30 minutes.

4.2.1.3 Chemical bonding properties of a-C:H underlayers

FTIR spectra were obtained to study the chemical bonding of the a-C:H underlayers. The FTIR spectra for the films prepared at different t_D are shown in Figure 4.5. The spectra can be separated into 2 main regions at wavenumber ranges of 1200-1900 cm^{-1} and 2700-3800 cm^{-1} . The absorption bands at 1200-1900 cm^{-1} are assigned to CH bending and C=C stretching bonds; while the band in the region of 2700-3800 cm^{-1} are assigned to various of CH_n groups and O-H bonds (Mutsukura and Akita 1999).

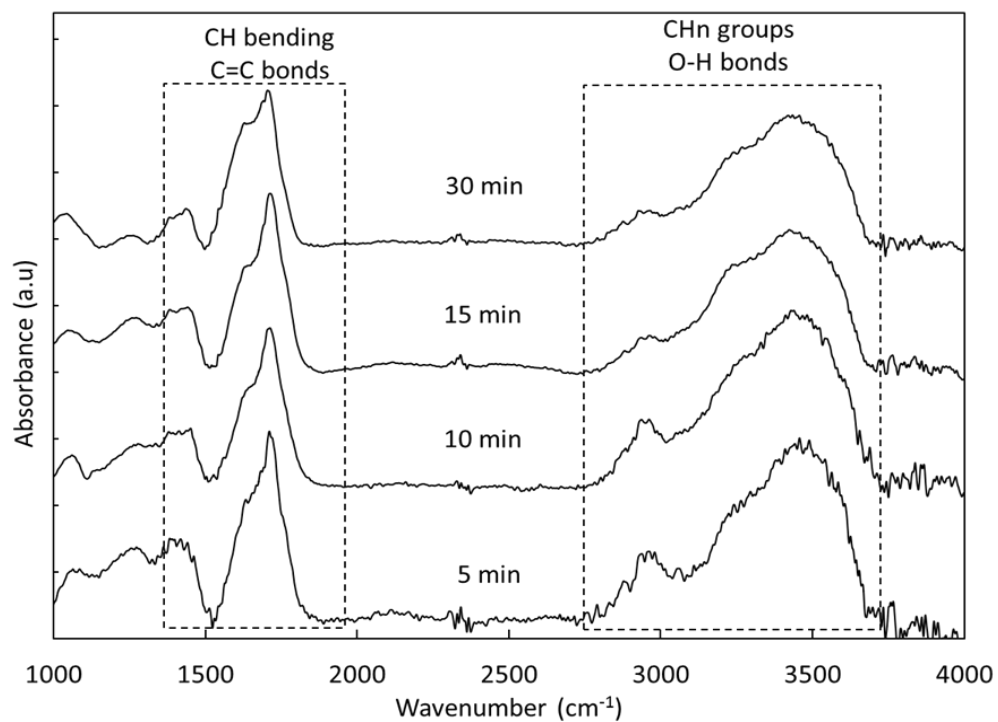


Figure 4.5: The FTIR spectra of a-C:H underlayer deposited for varied deposition duration.

For detailed analysis, the FTIR spectra were deconvoluted into its corresponding components as shown in Figure 4.6. For the region in the wavenumber range of 1200-1900 cm^{-1} , the deconvolution peaks corresponds to sp^2 C, Raman D, sp^3 CH, Raman G, CH, C=C and C=C stretching modes found at 1350, 1380, 1450, 1580, 1600, 1650 and

1700 cm^{-1} , respectively. The peaks in the second region within the wavenumber range of 2700-3200 cm^{-1} are represented by the symmetry $\text{sp}^3 \text{CH}_2$, symmetry $\text{sp}^3 \text{CH}_3$, asymmetry $\text{sp}^3 \text{CH}_2$, asymmetry $\text{sp}^3 \text{CH}_3$, $\text{sp}^2 \text{CH}$ and $\text{sp}^2 \text{CH}^2$ bonds located at 2835, 2875, 2930, 2960, 3000 and 3020 cm^{-1} respectively. From these spectra, the chemical bondings in the films remain almost the same indicating that the bonding composition remains the same irrespective of t_D . In particular, the bonds within the range of 1200-1900 cm^{-1} remain almost the same, with the deconvolution peaks showing almost no changes with the change in t_D . This is expected since the deposition parameters such as the RF power, deposition pressure and temperature, and gas flow rates were kept constant. These parameters are the ones which would greatly affect the structure of the films. The deposition duration should not influence the structure of the bulk film drastically. This however does not mean that the bonding and structure of the film does not alter during the film growth, as proven in the AFM analysis. This could be correlated with the slight change in the absorption intensities of the CH_n bands within the wavenumber range of 2700-3200 cm^{-1} . It could be seen that their intensities decreases particularly for the films deposited at t_D above 10 minutes which indicates a decrease in H content in the film. The fact that this decrease occurs for the film deposited at t_D above 10 minutes coincide with the change in the film surface from the cone-like formation to a smoother surface, and corresponding decrease in surface roughness. This suggests a certain relationship between the decrease in H content through the CH_n bonds and the surface morphology. It is believed that H etching and energetic ion bombardment of the growing surface may contribute to the formation of these cone-like structures thus creating a very rough film surface. These cone-like structures were believed to be covered with H terminated bonds. The presence of energetic H atoms at the growth sites resulted in the formation of these bonds as they were easily diffused onto the dangling bonds covering the surface of these cone-like

structures. These effects become effective at the initial t_D up to t_D of 10 minutes where the formation of these cone-like structures form uniformly on the film surface. However with the further increase in t_D from 10 minutes to 30 minutes, the increase in the number of growth radicals at the growth sites increased the size of the cone-like structures, forcing them to fuse together. This will effectively embed the cone-like structures as indicated in the progression shown in Figure 4.3 (c) and (d). Finally, as seen in Figure 4.3 (e) a smooth surface effectively covered the cone-like structures results in the smooth film. This corresponds to the gradual decrease in surface roughness from t_D 10 minutes to 30 minutes seen in Figure 4.4.

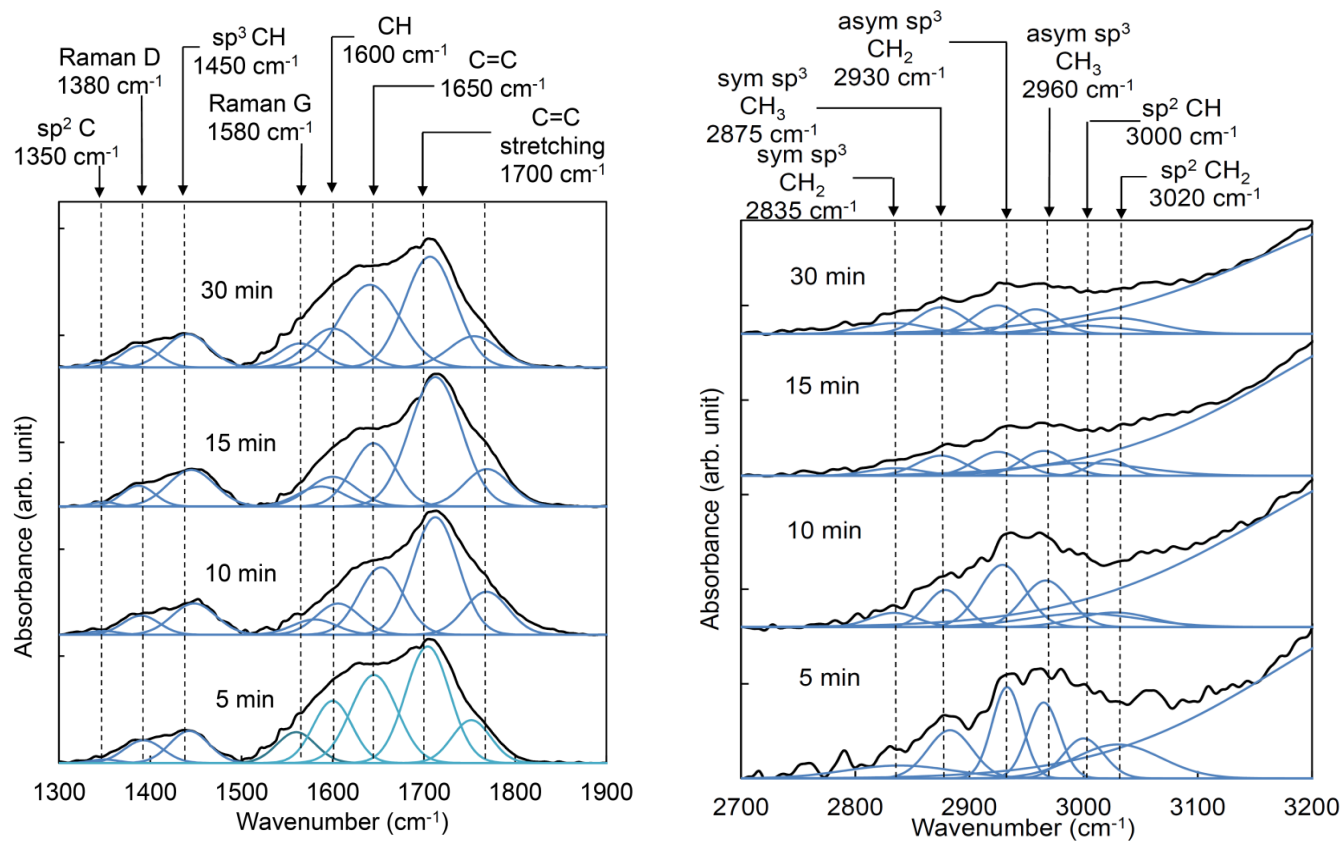


Figure 4.6: Variation of FTIR spectra for a-C:H underlayers deposited at different duration of 5, 10, 15 and 30 minutes.

4.2.1.4 Raman Analysis

Figure 4.7 (a) and (b) present the raw Raman spectra and the Raman spectra after the background extraction for a-C:H underlayers prepared at different t_D of 5, 10, 15 and 30 min respectively. The typical D and G peaks are detected around Raman shift of 1360-1380 cm^{-1} and 1580-1600 cm^{-1} respectively assigned to disorder and graphitic carbon (Ferrari and Robertson 2000). The D band is attributed to disordered sp^2 graphite-like micro-domain induced by linkage with sp^3 carbon atoms and the finite crystalline sp^2 micro-domains whereas G band corresponds to a graphite-like layer of sp^2 micro-domains (Liu et al. 2002). In general, the G band is more dominant compared to the D band.

The strong background could be observed in Figure 4.7 (a) for a-C:H underlayer prepared at 5 minutes due to strong luminescence which results in positive slope in the baseline (Nemanich et al. 1988). This phenomenon was also observed by Theye et al. when they used Raman spectroscopy to characterize the hydrogenated amorphous carbon film (Theye, Paret and Sadki 2001). As the deposition time increases from 10 to 30 minutes the decrease in slope of the Raman spectra could be observed. These results are in agreement with the results observed in the FTIR results discussed previously. Further analysis of these Raman spectra was done. The luminescence background has been removed by subtracting their baseline and the spectra were deconvoluted into 3 bands as shown in Figure 4.7 (b). The spectra show two prominent peaks which are D and G bands, and a background peak at Raman shift approximately at 1500 cm^{-1} indicated by the curve fit assigned to disordered sp^3 carbon according to Chu et al. (Chu and Li 2006). However, the presence of D band is forbidden in ideal graphite. As it is disturbed by sp^3 sites, the intensity of D band increases (Schwan et al. 1996).

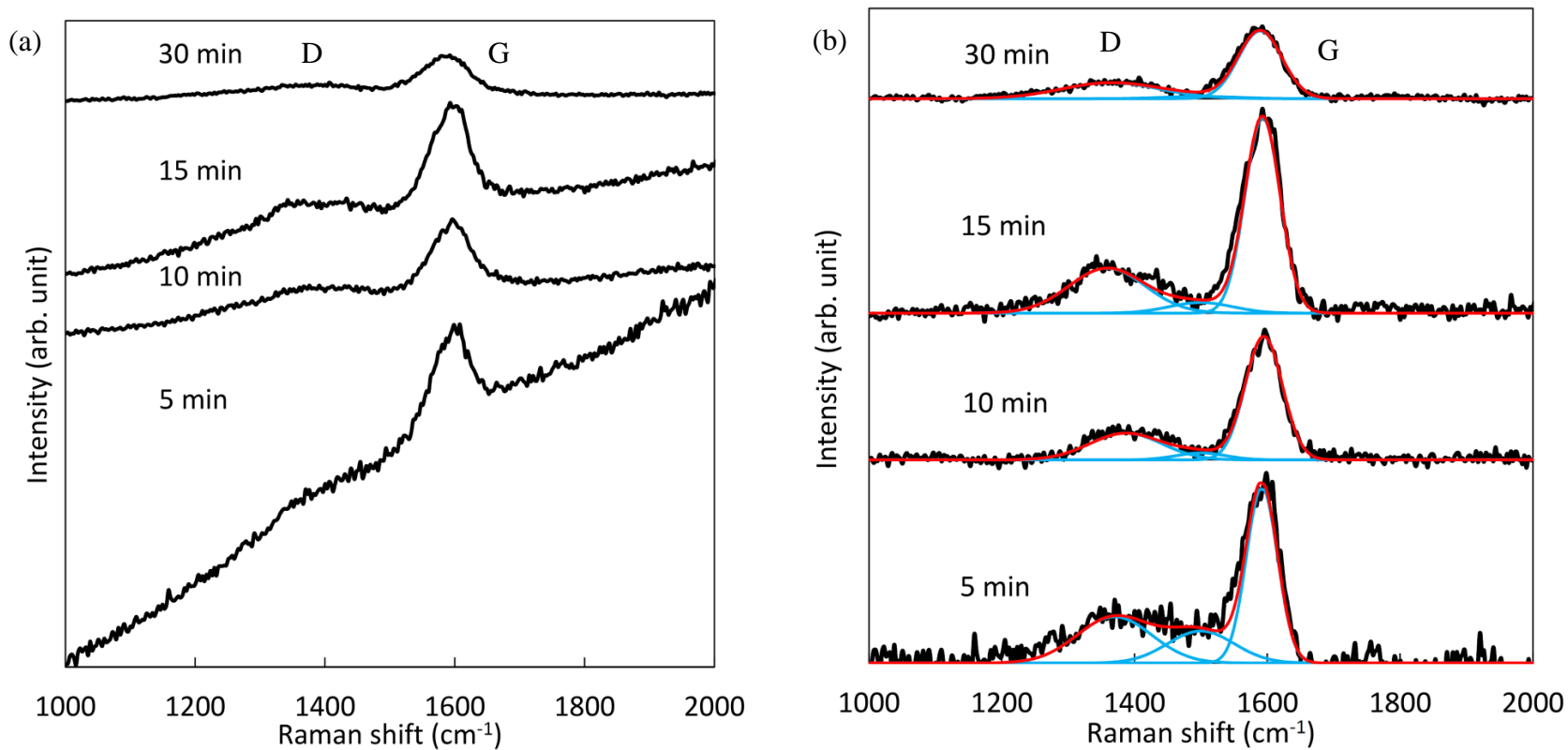


Figure 4.7: The raw Raman spectra with strong background (a) and the Raman spectra after the background extraction (b) for a-C:H underlayers prepared at different deposition duration of 5, 10, 15 and 30 min.

From Raman analysis, the variation of G and D peak positions, FWHM and I_D/I_G ratio for a-C:H underlayers as a function of t_D were obtained as shown in Figure 4.8. In general, the G peak position is almost uniform at $\sim 1590\text{ cm}^{-1}$ for all films as shown in Figure 4.8 (a). This is higher than its 1550 cm^{-1} value in visible Raman but does not exceed the band limit of graphitic carbon. This indicates that the shifted G peak position in uv region is contributed by olefinic (chain) sp^2 groups with high vibrational frequencies than graphitic groups due to their shorter bond lengths (Gilkes et al. 1998). Likewise the D peak position, it is also uniform at around 1375 cm^{-1} for the a-C:H underlayer deposited at t_D of 5, 10 and 15 minutes and increases to 1390 cm^{-1} for a-C:H underlayer prepared at t_D of 30 minutes as shown in Figure 4.8 (b). The band width of G and D bands for a-C:H underlayer prepared at t_D of 10 minutes are highest compared to others as seen in Figure 4.8 (c) and (d). It is suggested that the a-C:H underlayer prepared at 10 minutes has lower degree of clustering of sp^2 phases and less ordered structures compared to those underlayers prepared at t_D of 5, 15 and 30 minutes (Jawhari, Roid and Casado 1995). This may be due to the increase in bond-angle disorder at sp^2 site in carbonaceous materials. From Figure 4.8 (e), the I_D/I_G ranges from 0.4 to 0.9. It is observed that the I_D/I_G decreases as the t_D increases indicating an increase in the ratio of sp^3 to sp^2 bonded to carbon. Zhao et al has suggested that the low ratio of I_D/I_G (<1) in disordered graphite is due to the decrement of defect or ordering of carbon atoms. This is shown by small crystal size or the destruction of symmetry in crystallite structure (Zhao et al. 2011).

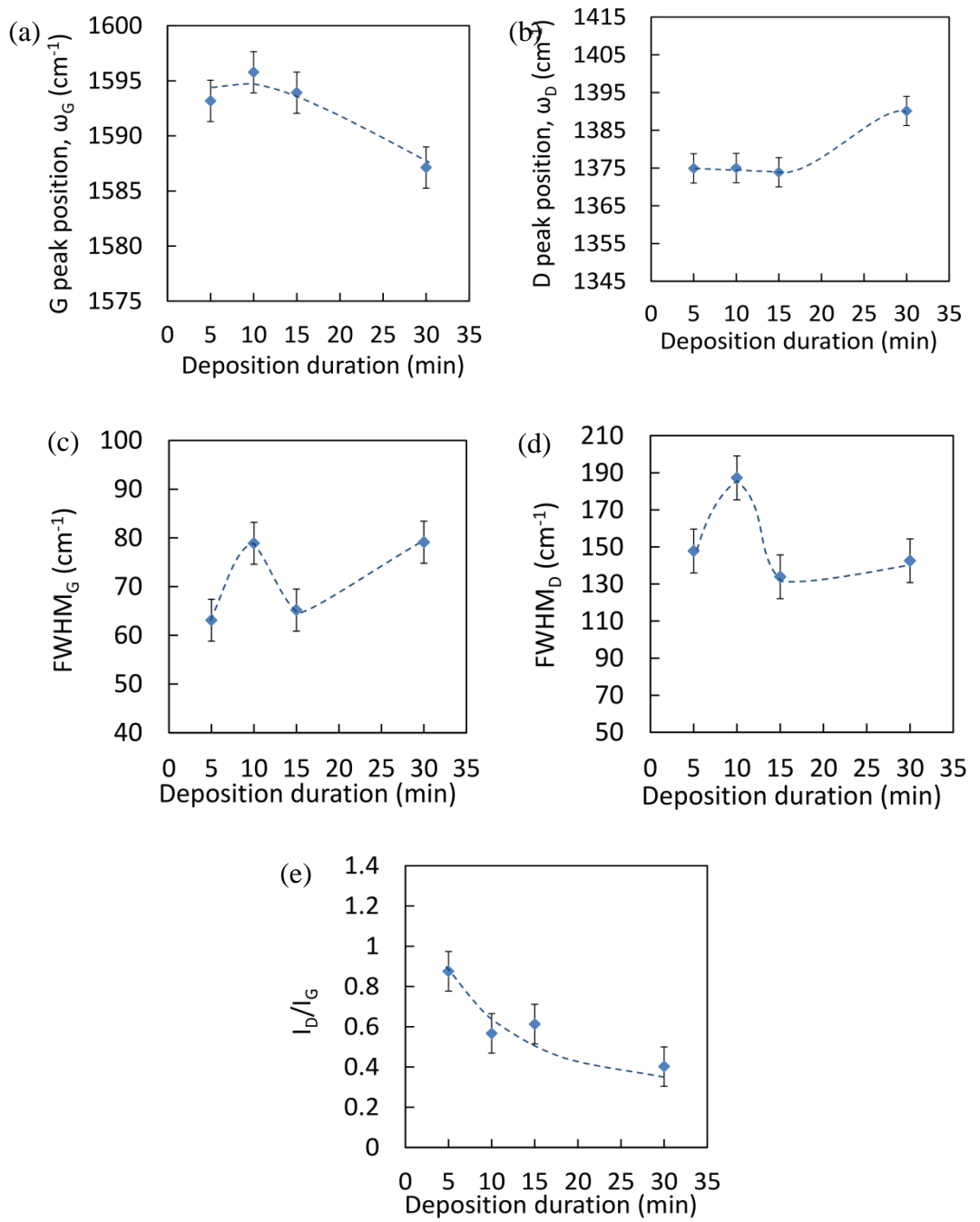


Figure 4.8: Raman analysis of a-C:H underlayers prepared at t_D of 5, 10, 15 and 30 minutes. Line is guide to the eyes.

4.2.2 Effect on Resulting ns-CN_x/a-C:H Formation

4.2.2.1 Surface and cross-sectional images

The surface and cross-sectional images of the ns-CN_x deposited onto the a-C:H underlayer which were produced at different t_D are shown in Figure 4.9.

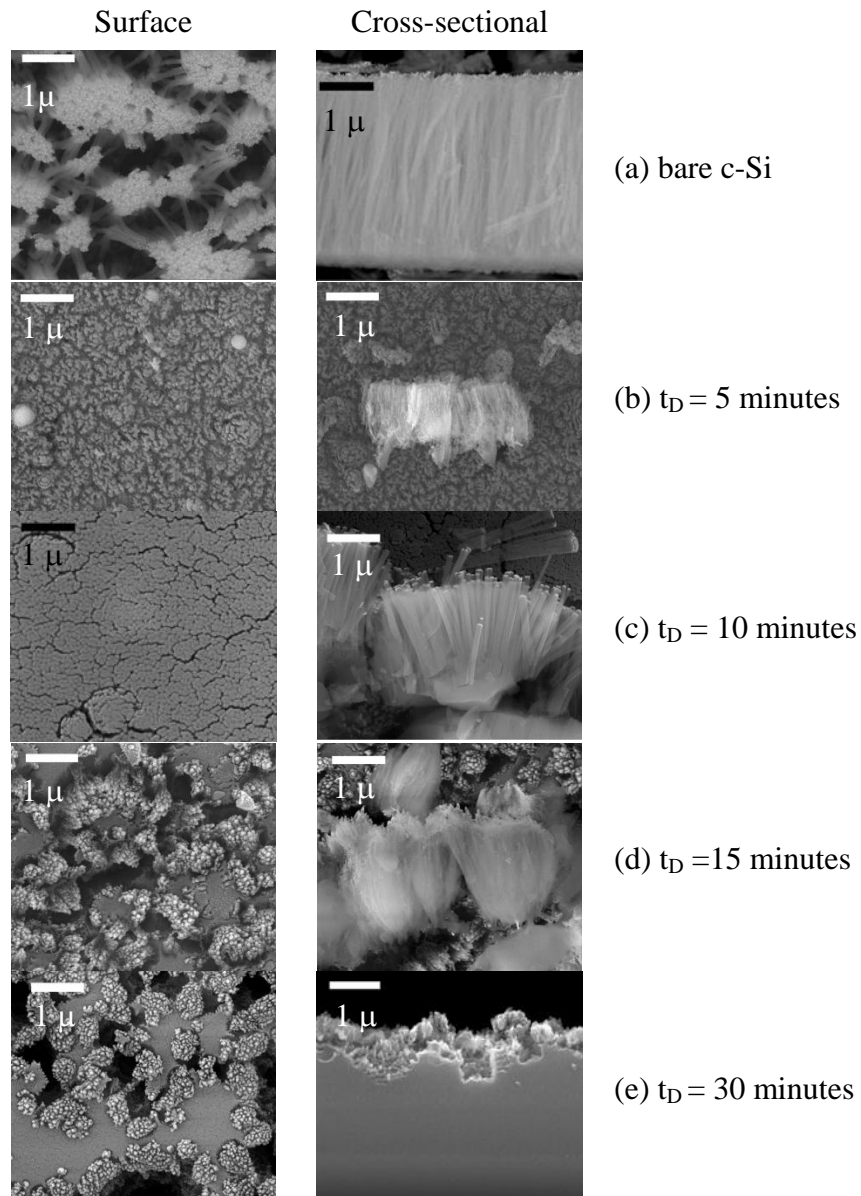


Figure 4.9: Surface and cross-sectional images of ns-CN_x deposited on a-C:H underlayer prepared at different t_D .

Figure 4.9 (a) shows that ns-CN_x could be deposited directly on bare c-Si substrate. These fiber-like nanostructures exhibited high aspect ratio with average diameter of 88 ± 14 nm and length of 3.81 ± 0.09 μm . It was also observed from Figure 4.9 (b)-(e) that the formation of ns-CN_x could be influenced by introducing the a-C:H as an underlayer base. The formation of these ns-CN_x on the a-C:H base varied in accordance to t_D . The nanostructures formed on the a-C:H underlayer deposited at t_D of 5 minutes resembles those on bare c-Si substrate but the length of the former was decreased by almost one third. Furthermore, they were more tightly packed and were formed on the surface of the a-C:H underlayer. The film deposited on the a-C:H underlayers at t_D of 10 minutes were tightly packed, rigid and cylindrical in shape with enhanced vertical alignment. These nanostructures show a slightly lower aspect ratio compared to the fiber-like structures produced on the bare c-Si substrate whereby the average diameter of the former was 84 ± 17 nm while their average length was 3.38 ± 0.07 μm . The ns-CN_x deposited on the a-C:H underlayer deposited at t_D of 15 minutes formed bunches of dendrite-like structures fused at the base. The nanostructures deposited on the a-C:H underlayer at t_D of 30 minutes also showed a dendrite-like structures but of smaller size protruding from that possibly the a-C:H underlayer. This is influenced by cone-like structure of the a-C:H as underlayer appears to decrease and disappear altogether.

Among these, the well aligned, rigid, cylindrical rod-like structure is of great interest. Figure 4.10 compares the well aligned fiber-like CN_x formed on bare c-Si and a-C:H underlayer deposited at t_D 10 minutes. The formation of the fiber-like ns-CN_x formed on the bare c-Si substrate is believed to be influenced by the crystalline structure of the substrate itself. In contrast, this was not so for film grown on the c-Si substrate coated with the a-C:H underlayer film. Here, the growth of the rod-like ns-CN_x coincided with the high surface roughness of the film. The high surface roughness was

contributed by the presence of vertical broad tip cone-like features of the a-C:H underlayer. These morphological features may have acted as the template for the formation of these structures. Ion bombardments on the H terminated bonds of the cone-like structures along with H etching effects during the growth of the CN_x structures might have induced the formation of a higher ordering of these structures which resulted in the growth of highly aligned rigid cylindrical nanostructures. It is also seen that the ‘roots’ of the nanofibers that grew directly on the c-Si substrate appear to form separately from each other. In contrast, the nanorods grew on the a-C:H underlayer appears to have more solid base where their ‘roots’ grew from. It is very likely that this base is the a-C:H underlayer film.

For deposition on the a-C:H underlayers film which were produced at t_D of 15 and 30 minutes, the formation of ns- CN_x reduced significantly in size and appeared as dendrite-like structures. These cone-like structures appear to be embedded in the a-C:H film. The changes in the growth of the ns- CN_x corresponds to the reduction in the surface roughness of the a-C:H underlayer and shows that the growth of the nanorods are effectively suppressed.

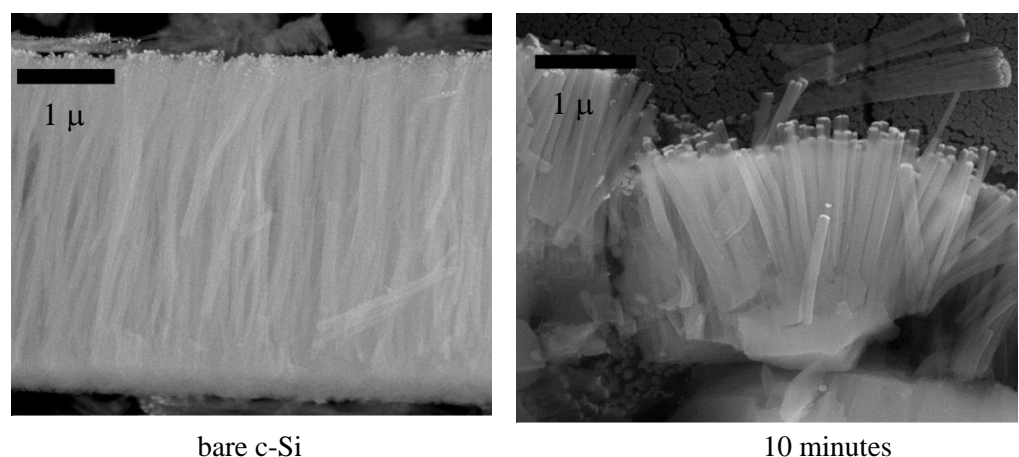


Figure 4.10: Variation of FESEM cross-sectional images for ns- CN_x deposited on bare c-Si and 10 minutes a-C:H underlayer.

4.2.2.2 Auger electron spectroscopy measurement of ns-CN_x

The elemental composition of these ns-CN_x was determined by using AES. From these measurements the relative concentration (%) of C and N elements were calculated. The N/C ratio for the ns-CN_x grown on the a-C:H deposited as a function of t_D is shown in Figure 4.11. The results indicate that the incorporation of nitrogen was at the highest for the film deposited at t_D of 10 minutes. This coincides with the formation of the rigid and aligned nanostructures (Ritikos et al. 2011). This indicates that high incorporation of N atoms into the film structure is important in the formation of the rigid and highly aligned vertical cylindrical ns-CN_x. It is important to determine how these N atoms are bonded to the C structure. This was studied by means of FTIR characterization.

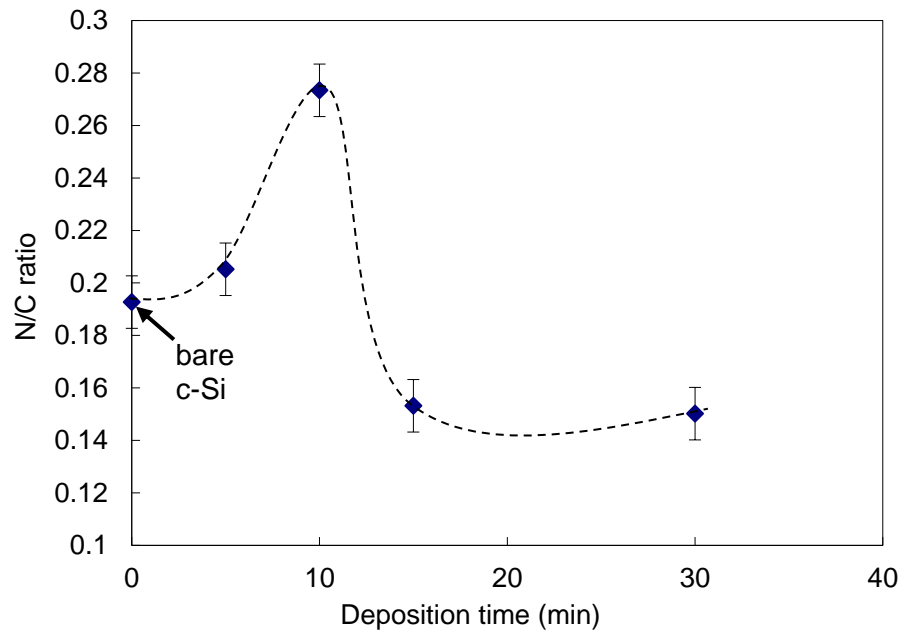


Figure 4.11: Variation of nitrogen to carbon N/C ratio of ns-CN_x deposited on c-Si, a-C:H underlayers at t_D of 5, 10, 15 and 30 minutes.

4.2.2.3 FTIR spectra of ns-CN_x

The FTIR spectra obtained for the ns-CN_x films deposited onto the a-C:H underlayer which was prepared as a function of t_D are shown in Figure 4.12. The spectra are composed of 3 main characteristic bonding groups. These include the absorption band at 1300-1800 cm⁻¹ related to sp²-CH bending and C=C and/or C=N; absorption band at 2000-2300 cm⁻¹ corresponding to sp¹ nitrile and/or isonitrile (C≡N) bonds and those at 2800-3700 cm⁻¹ which are related to sp³ CH_n groups and N-H and / or O-H (Motta and Pereyra 2004; Mutsukura and Akita 1999; Pereira et al. 2006). For clarification, the individual spectra for each region are presented in Figure 4.13. Compared to the spectra for the a-C:H underlayer (Figure 4.5), the spectra for the ns-CN_x films show the additional absorption region within the range of 2000-2300 cm⁻¹, which was attributed to the incorporation of N atoms into the film structure. Indeed it is the band in this region which shows the most significant changes with the variation in the deposition parameter. These changes are deemed more important and reliable than the other regions since the changes in the sp² or sp³ phases may be influenced or contributed by any changes in the a-C:H underlayer films during the CN_x deposition.

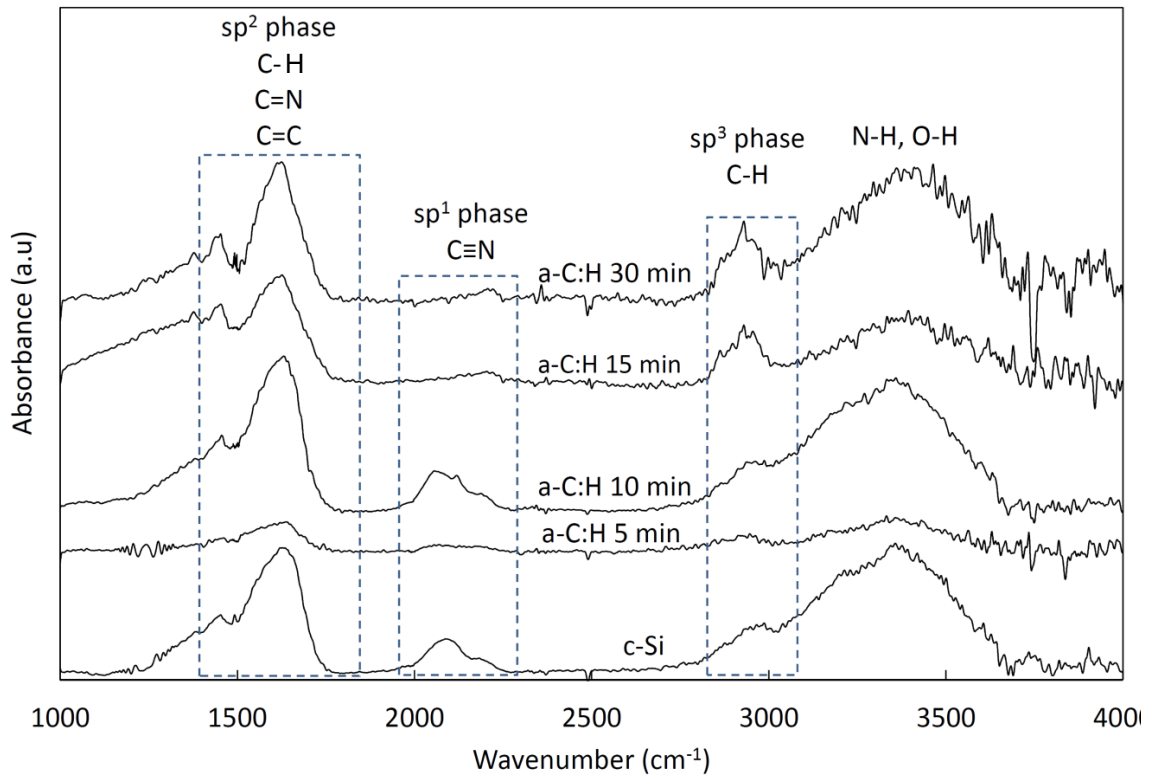


Figure 4.12: Variation in FTIR absorbance spectra of ns-CN_x as a function of deposition duration of a-C:H underlayers.

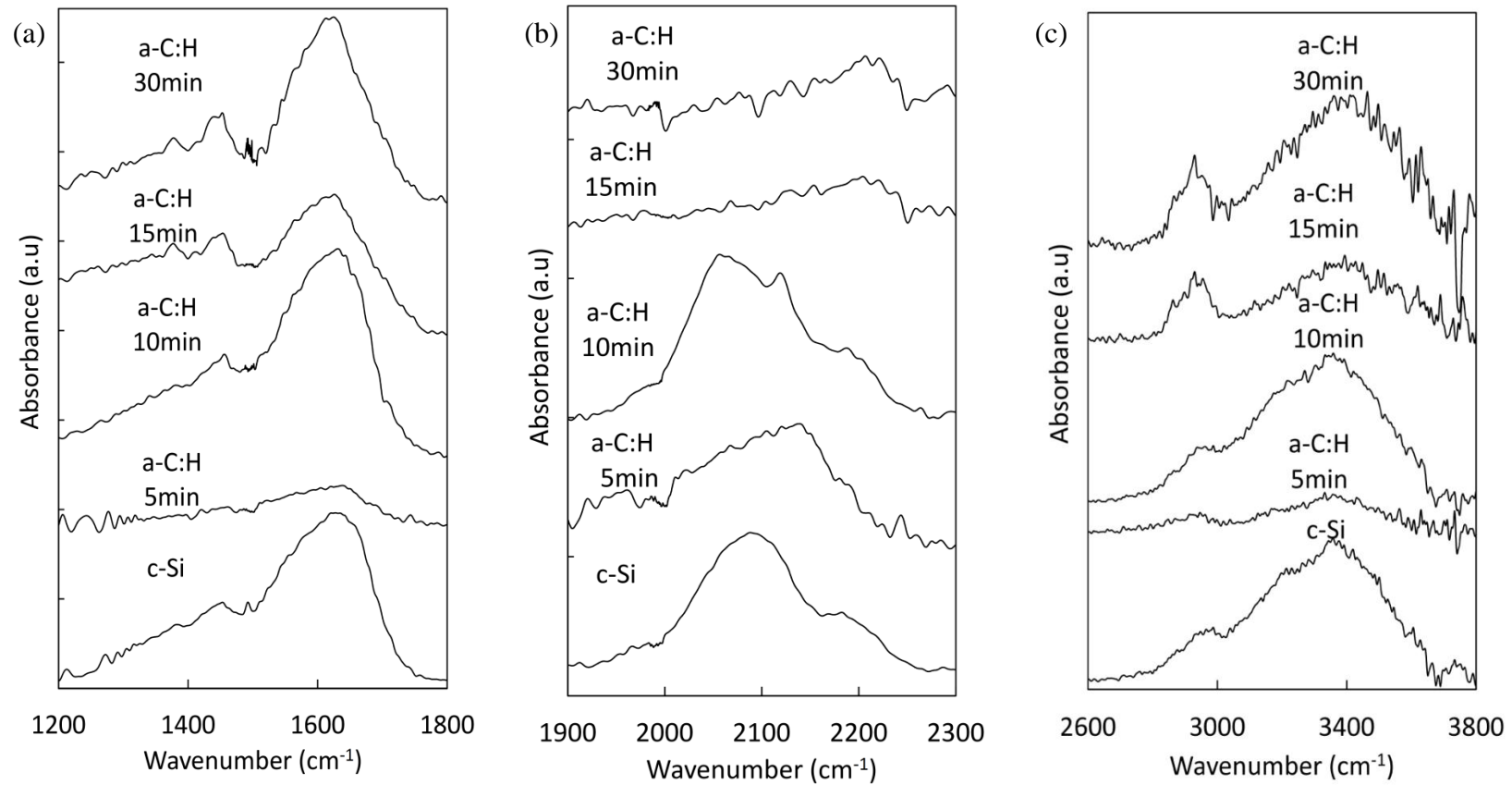


Figure 4.13: The FTIR spectra for ns-CN_x deposited at different t_D of a-C:H underlayers in the range of (a) sp^2 , (b) sp^1 and (c) sp^3 phases.

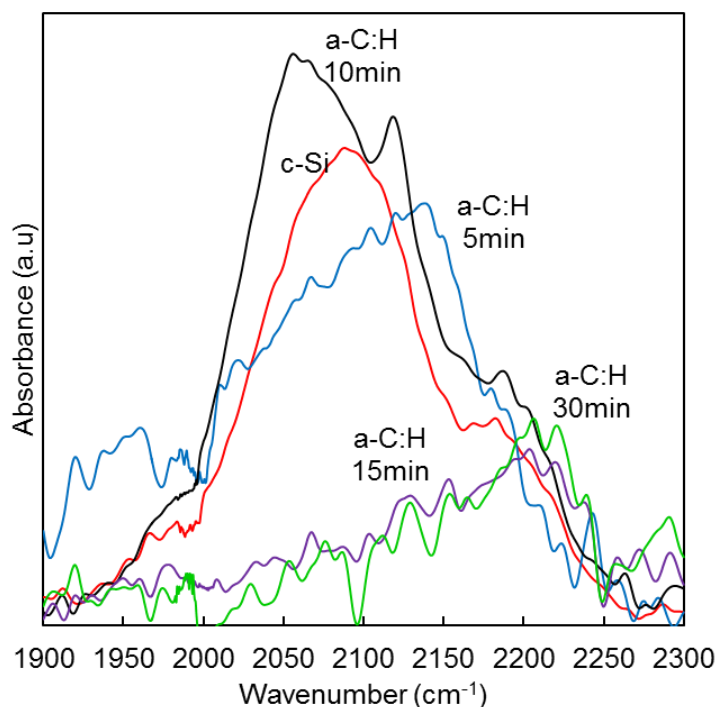


Figure 4.14: The FTIR spectra in the wavenumber range of 1900-2300 cm^{-1} of CN_x nanostructures as a function of t_D a-C:H underlayers.

The spectra region in question, shown in Figure 4.14 is contributed by the presence of nitrile and/or isonitrile ($\text{C}\equiv\text{N}$) bonds in the films. The broad bands in this region were decomposed into five overlapping bands associated with these nitrile ($-\text{C}\equiv\text{N}$) and isonitrile ($-\text{N}\equiv\text{C}$) bonds (Mutsukura 2001; Mutsukura and Akita 1999) which include the isolated and/or fused aromatic rings bonded either to isonitrile ($-\text{N}\equiv\text{C}$) bonds at 2105 cm^{-1} or nitrile bonds ($-\text{C}\equiv\text{N}$) at 2215 cm^{-1} ; hydrocarbon molecules which include C_2H_5 at 2160 cm^{-1} and CH_3 at 2190 cm^{-1} bonded to isonitrile ($-\text{N}\equiv\text{C}$); and the hydrocarbon groups (CH_3 , C_2H_5 , etc.) bonded to nitrile ($-\text{C}\equiv\text{N}$) which appear as a single peak at 2245 cm^{-1} . The deconvolution of the spectra carried out using standard Gaussian curve-fitting method (Fanchini et al. 2005; Mutsukura and Akita 1999) is shown in Figure 4.15. Among these spectra and their deconvolution, a consistency in the film prepared on bare c-Si and the underlayer film at t_D of 10 minutes

is observed, where they exhibit some similar traits and preferential bonds in the films. These preferential bonds coincide with the formation of the vertical aligned nanostructures for both films, suggesting the importance of these bonds.

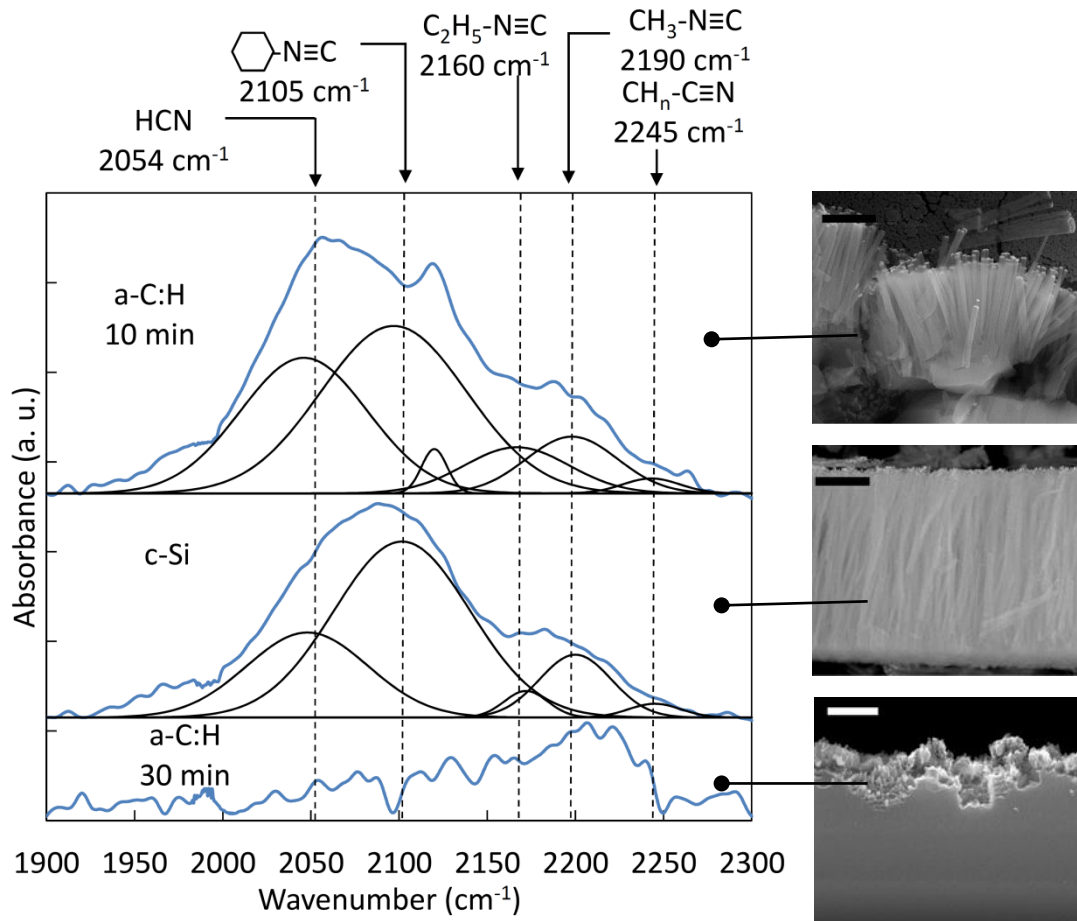


Figure 4.15: Gaussian fitting profiles for FTIR spectra in wavenumber region of 2000-2300 cm^{-1} for a-C:H underlayer at t_D 10, 30 minutes and c-Si.

The dominant peak in both samples was located at 2105 cm^{-1} suggesting the preferential bonding of isonitrile bonded to aromatic rings in the film in the formation of these nanostructures. The presence of these bonds also suggest a dominant presence of aromatic bonds in the film being part of the architecture that made up the nanostructures. In addition, isonitrile bonds tend to form rigid, linear and continuous non-terminating bonds, which would form long ordered networks in the material

suitable for the formation of the nanostructured fibers and rods. Furthermore, preferential bonding of the ring through N atom rather than C for the isonitrile, suggested the presence of partial charge ($-N^+ \equiv C^-$) formed within the nanostructures. The electric field imposed by the RF plasma aligns the partial charge, resulting in the formation of the vertical aligned growth of these structures perpendicular to substrate surface (Ritikos et al. 2011).

4.2.3 Summary

The influence of the surface morphological and chemical bonding properties of PECVD-grown a-C:H underlayer pre-deposited films on p-type $\langle 111 \rangle$ c-Si substrates were studied. The effects of the films properties on the subsequent growth ns-CN_x produced on these films are reported. This study shows that a-C:H pre-deposited underlayer films could be used as a template for the formation and modification of ns-CN_x. Indeed with the use of these a-C:H template the rigidity and shape of the ns-CN_x could be modified from the vertically aligned CN_x nanorods produced on bare c-Si. The formation of rigid and vertically aligned cylindrical ns-CN_x is produced on a-C:H underlayer prepared at t_D of 10 minutes. Though the structure and properties of these a-C:H films appear to have minimal variation with t_D , the a-C:H film produced at t_D of 10 minutes shows the highest surface roughness. Its surface morphology is made up of broad tip cone-like structures with highly ordered sp^2 clusters covered with H terminated bond. Nitrogen incorporation in ns-CN_x and the preference of isonitrile bonds in the film induce the formation of vertically aligned ns-CN_x.

4.3 Effects of RF Power on a-C:H Underlayer and Resulting $\text{CN}_x/\text{a-C:H}$ Formation

This section study the effects of different applied RF power, P_{UL} on the deposition of the a-C:H underlayer and the effects on the resulting ns- CN_x . P_{UL} were set at 30, 40, 50, 60, 80 and 100 W giving 6 sets of a-C:H underlayers and corresponding ns- $\text{CN}_x/\text{a-C:H}$ films. The deposition time was fixed at 10 minutes. The effects of applied RF power on the formation of a-C:H underlayers by RFPECVD have been investigated by other researchers working on this material (Choi et al. 2005; von Keudell, Meier and Hopf 2002). It is generally accepted that applied power significantly influences the structure of the deposited a-C:H films. Three aspects are usually taken into consideration when dealing with the studies of P_{UL} on the film deposition. These include (i) the dissociation of gas precursors through primary and secondary reactions in the plasma, (ii) absorption and desorption processes on the film surface, and (iii) ion bombardment on the growth surface. The first aspect is associated with gas phase reactions, while the second and third aspects are related to surface reactions. Each aspect has its influence on the resulting film.

4.3.1 Effects of RF Power on a-C:H Underlayer

4.3.1.1 *Growth rate of a-C:H underlayers*

Figure 4.16 shows the relationship between P_{UL} and the corresponding film growth rate of the a-C:H underlayers. It is also found that the increase in P_{UL} significantly increases the growth rate of the a-C:H underlayer films. The reason for the increase in growth rate is probably due to the increase in dissociation of the CH_4 . This will increase the number of reactive species in the plasma including hydrocarbon radical

and ion through primary reactions, and further enhancement through secondary reactions of these radicals with other available CH_4 molecules (von Keudell, Meier and Hopf 2002). However, a slight decrease in thickness and growth rate of a-C:H underlayer deposited at RF power of 60 W could be due to a more dominant ion bombardment effects compared to a-C:H underlayers prepared at RF power of 30, 40, 50, 80 and 100 W.

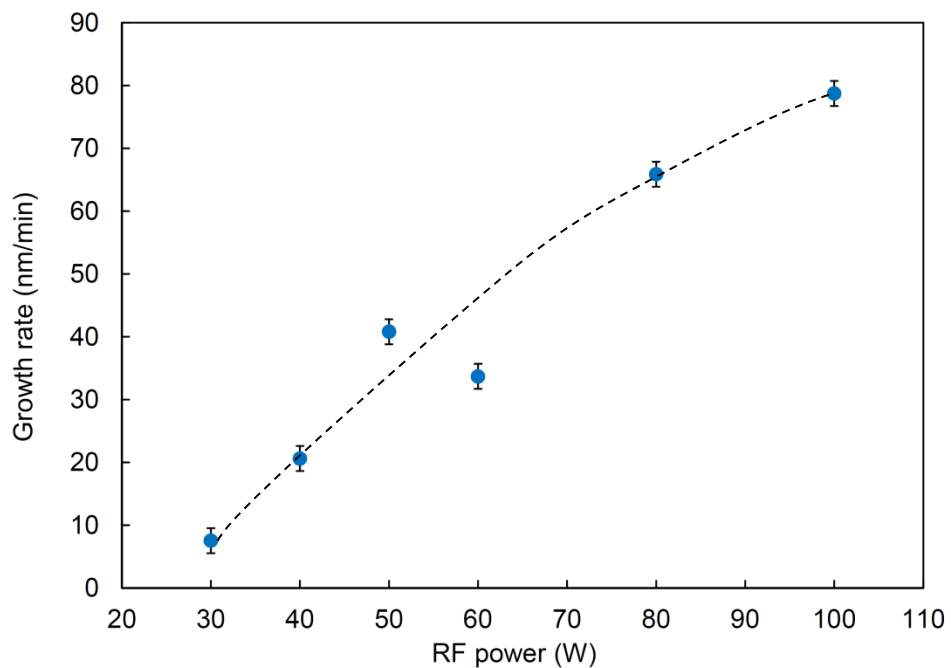


Figure 4.16: Growth rate of a-C:H underlayers deposited by RFPECVD at different RF power. The line is only an eye-guide.

4.3.1.2 *Surface roughness and surface morphology of a-C:H underlayers*

The surface morphology of the a-C:H underlayers was studied by AFM analysis. The surface morphologies of the a-C:H underlayers are shown in Figure 4.17. In contrast with the progressive increase in the growth rate with increasing P_{UL} , the surface morphology and its corresponding surface roughness of the a-C:H underlayer (R_{UL}) films show different trend.

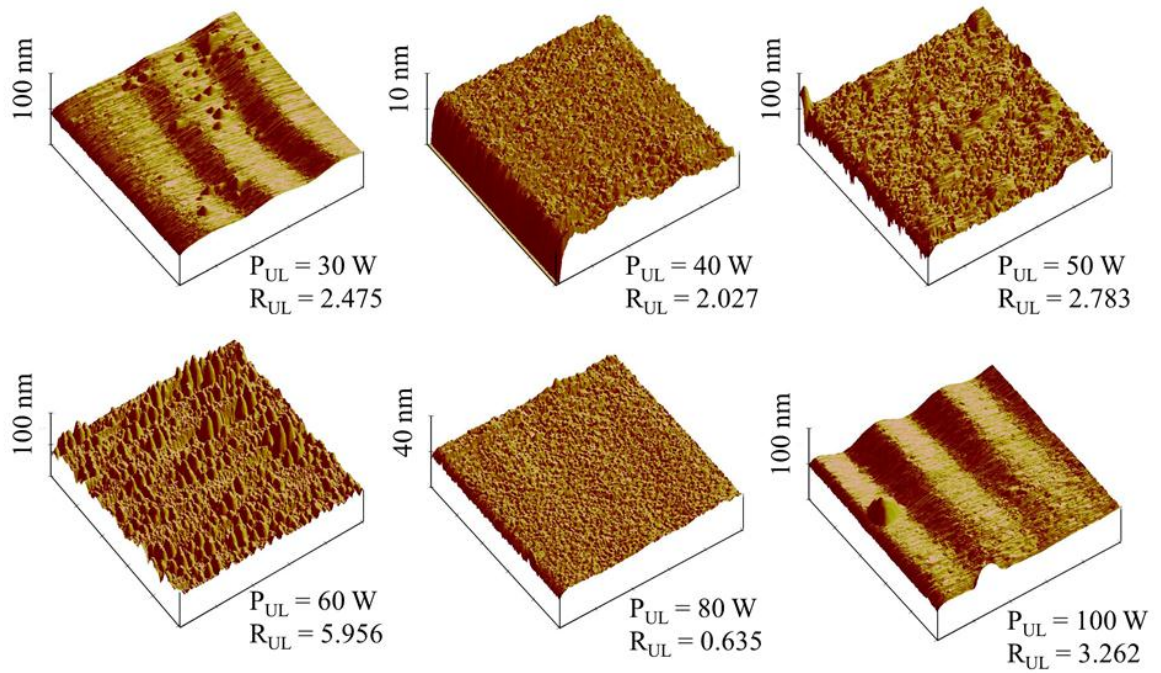


Figure 4.17: AFM surface morphology of a-C:H underlayers deposited for RF power of 30, 40, 50, 60, 80 and 100 W.

Figure 4.18 presents the variation of surface roughness R_{UL} of a-C:H underlayers as a function of P_{UL} . R_{UL} was almost constant when P_{UL} is varied from 30 to 50 W, then spikes to a maximum at P_{UL} of 60 W before decreasing to a minimum at P_{UL} of 80 W. With the current results, specific explanations could not be given for the variation in R_{UL} with P_{UL} particularly to the significant decrease in R_{UL} for film deposited at P_{UL} of 80 W. However, the changes in R_{UL} are believed to be attributed by various degree and contribution of the gas phase and surface reactions. Though the substrate is grounded throughout the deposition process, ion bombardment contributed by the plasma, is expected to play an important role in the structural formation of the films. This may be true considering the close proximity of the electrodes (1 cm). Ion bombardment would effectively remove weak hydrogen bonds from the surface allowing structural modifications to occur as P_{UL} is varied. Also when P_{UL} is increased, primary reactions would dominate the gas phase reactions allowing increase in

production of hydrocarbon radicals until all the precursor gas were completely dissociated.

This could lead to variation of surface modification of a-C:H underlayers. It is believed that the high R_{UL} of the film deposited at P_{UL} of 60 W is due to the enhancement of ion bombardment effect at this RF power. However, when P_{UL} is further increased, the gas phase reactions dominates, with the primary reactions determining the properties of the films and this leads to the suppression of the ion bombardment effects.

It is also noted that the rest of the films also shows some resemblance of nanostructures but different forms from that of the film deposited at P_{UL} of 60 W. These include the large elongated mounds in the films deposited at P_{UL} of 50 W, or the more scattered isolated cones present on the films grown at P_{UL} of 30 W and 100 W.

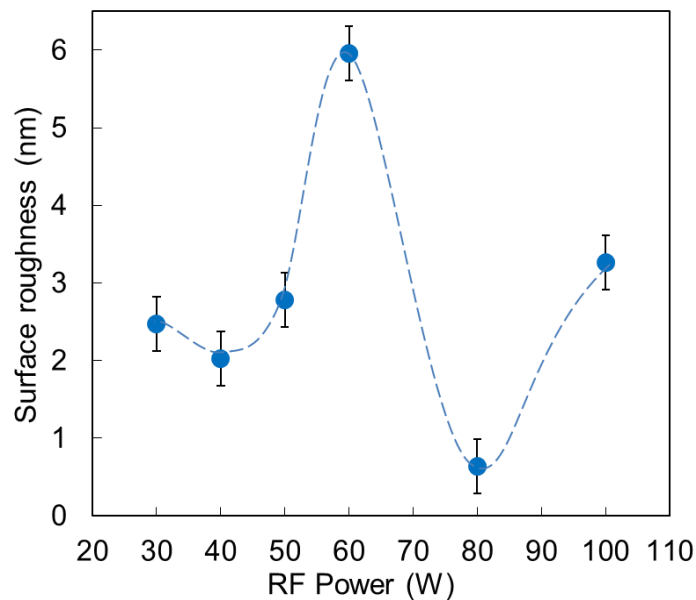


Figure 4.18: Variation of surface roughness of a-C:H underlayers deposited at RF power of 30, 40, 50, 60, 80 and 100 W.

4.3.1.3 FTIR spectra of a-C:H underlayers

The FTIR spectra of the C:H underlayer films prepared at different P_{UL} are shown in Figure 4.19. Included is also the corresponding surface roughness. These spectra also show the expected functional groups common for a-C:H films. These groups consist of various sp^2 C related bonds in the wave number range of 1300-1700 cm^{-1} . Among others, these bonds include those of C-C, the so called G and D bands and sp^2 C bonds at frequency range of, 1550-1570 cm^{-1} , 1360-1380 cm^{-1} and 1620-1650 cm^{-1} , respectively (Lazar et al. 2005). Also, the CH_n bands are clearly observed within the frequency range of 2800-3050 cm^{-1} which includes various overlapping sp^2 and sp^3 CH_n bonds (Ghodselahe and Vesaghi 2008). For clarification, the individual spectra for each region are presented in Figure 4.20.

A significant difference between the spectra of the film deposited at P_{UL} of 60 W and the rest of the films is clearly seen and this film shows the highest R_{UL} . While the rest of the films show a more dominant and stronger CH_n bands than the sp^2 C bands, the opposite is seen for film at P_{UL} of 60 W. The decrease in CH_n shows that there is a significant decrease in H content in the film. This is in line with the proposed decrease of H bonds due to their removal by ion bombardment. The sp^2 C bonds are observed to show a more dominant presence in these films compared to sp^3 C bonds. The clustering of sp^2 C species within the amorphous sp^3 C matrix is reflected by the surface morphology and high R_{UL} of the film deposited at RF power of 60 W. The smooth cone shaped structures seen on the film deposited at P_{UL} of 60 W, may very well be linked to these sp^2 clusters. On the other hand with further increase in P_{UL} to 80 W and 100 W, the increase in the H content supports the later explanation of decrease in surface roughness in AFM analysis attributed to the suppression of ion bombardment effect on the film during growth. Indeed in both extreme cases of the films deposited at P_{UL} of 60 W and 80 W, where the former show the highest R_{UL} but weakest CH_n bonds (high sp^2

absorption bands) and the latter shows the lowest R_{UL} but strong CH_n bonds (and lowest sp^2 absorption bands), the relationship between H content and R_{UL} is undeniable.

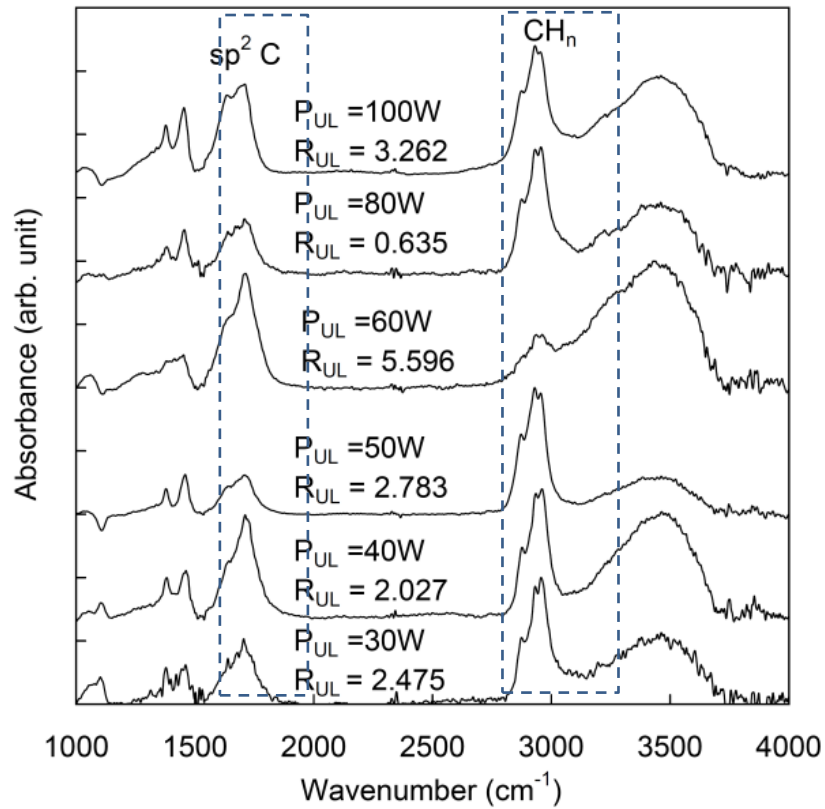


Figure 4.19: The FTIR spectra of a-C:H underlayer at different RF power of 30, 40, 50, 60, 80 and 100 W.

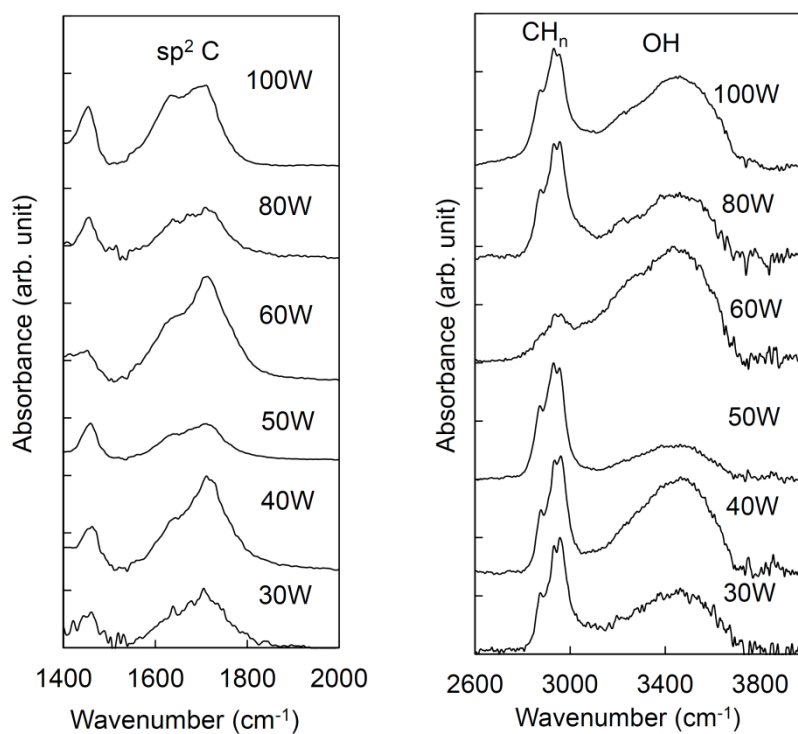


Figure 4.20: Variation of FTIR spectra for a-C:H underlayers deposited at different RF power in the range of 1400-2000 cm^{-1} and 2600-4000 cm^{-1} .

4.3.1.4 Raman scattering analysis

The structural properties of a-C:H underlayers was further studied by Raman scattering microscopy. The Raman spectra of a-C:H underlayers deposited at different P_{UL} are shown in Figure 4.21. Figure 4.21 (a) is plotted from the raw Raman data and exhibits strong photoluminescence (PL) background which causes the positive slope in the spectral baseline. The presence of this slope was also observed by Casiraghi et al. in their study of hydrogenated diamond-like carbon films (Casiraghi et al. 2005). According to Casiraghi et al., the increasing PL background is due to increasing H content in the films which contributes to hydrogen saturation of non-radiative recombination centers in the films (Escobar-Alarcón et al. 2005).

Coincidentally, the spectrum of a-C:H underlayer prepared at P_{UL} of 60 W almost do not show this characteristic slope which again supports the low H content in the film. It is also found that the PL background strengthens at low P_{UL} . For further analysis of these Raman spectra, the PL background was removed by subtracting the baseline. These corrected spectra are shown in Figure 4.21 (b). These spectra show two prominent peaks which are the D and G bands, and a background peak at Raman shift of approximately 1500 cm^{-1} assigned to amorphous hydrogenated carbon (Huang et al. 2003) commonly observed in PECVD using CH_4/H_2 discharge. The D and G bands lie at $1360\text{-}1380$ and $1580\text{-}1600\text{ cm}^{-1}$ respectively (Miyajima, Henley and Silva 2011).

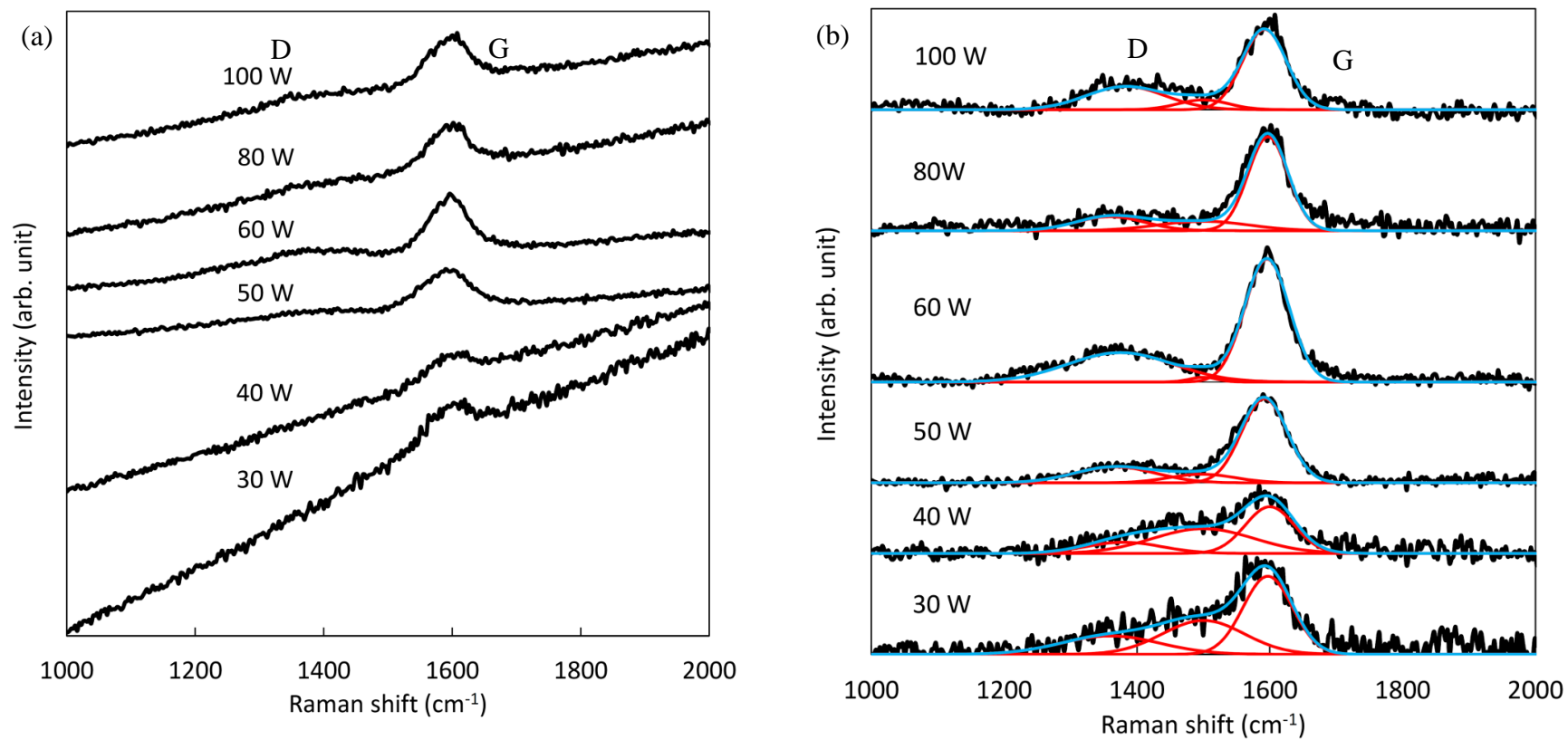


Figure 4.21: Raw Raman spectra (a) and corrected Raman spectra (b) of a-C:H underlayers as a function of RF power.

Figure 4.22 presents the Raman analysis of a-C:H underlayers including the variation in (a) G peak position, (b) D peak position, (c) FWHM_G , (d) FWHM_D and (e) I_D/I_G . In general the G peak positions of all these films were blue shifted towards 1600 cm^{-1} compared to deposition normally found for pure graphite at 1560 cm^{-1} . This indicates that these films are made up not only of nanocrystalline graphitic structure but also C=C sp^2 stretching vibrations of olefinic or conjugated carbon “chain” in the films (Schwan et al. 1996; Wang and Zhang 2007). As shown in Figure 4.22 (d), a-C:H underlayer films prepared at 30 and 60 W show higher FWHM_D compared to the rest of the films. This behavior indicates increase in the disorder in sp^2 C bonds. This is due to the presence of different order in the clusters distribution.

Among these films, the a-C:H underlayers deposited at 60 and 100 W shows high I_D/I_G ratio of 0.56 and 0.52, respectively. High in I_D/I_G indicates an increase in the number and/or size of graphitic cluster in the films (Ferrari and Robertson 2000). This suggests that the C atoms have high probability of forming C=C ring structures rather than the chain structure. In addition, a-C:H underlayer prepared at P_{UL} of 60 W has the highest I_D/I_G ratio which is ascribed to the conversion of sp^3 to sp^2 bonds and desorption of hydrogen. This is also in line with FTIR results which show more sp^2 C bonds. Thus, the a-C:H underlayer film prepared at P_{UL} of 60 W has dominant sp^2 C bonds. The Raman results suggest that the a-C:H underlayer deposited at P_{UL} of 60 W consists of dominant sp^2 clusters compared to the rest of the films. This supported the observation in both AFM and surface roughness results that these sp^2 clusters may contribute to highest surface roughness seen in the film.

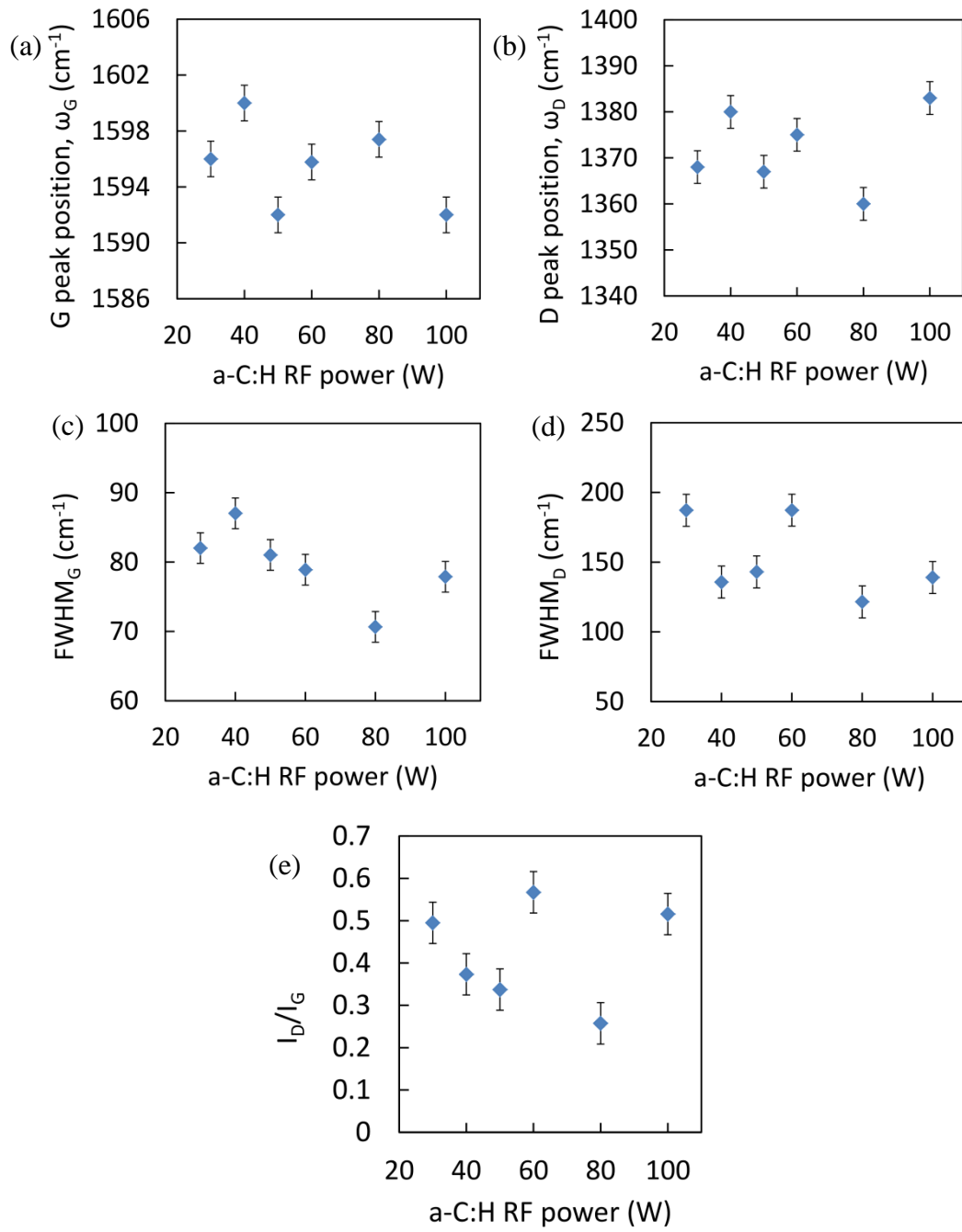


Figure 4.22: Raman analysis of a-C:H underlayers prepared at different RF power.

4.3.2 Effect of RF Power on Resulting $\text{CN}_x/\text{a-C:H}$ Formation

4.3.2.1 *Surface and cross-sectional images*

The next phase of this work is to study the morphology and structural properties of the ns- CN_x with respect to the properties of the a-C:H underlayer on which these nanostructures were grown. Here, R_{UL} of the a-C:H underlayer is used as the reference rather than P_{UL} so as to shift our focus towards the establishment of the a-C:H underlayer properties on these ns- CN_x films. The changes in the structure of the ns- CN_x films could be clearly seen from the FESEM surface and cross section images shown in Figure 4.23.

A remarkable and progressive transformation of these structures with the increase in R_{UL} of a-C:H underlayer is observed. At the lowest R_{UL} of 0.635, ns- CN_x are formed as vertical sheet-like structures that protrude from the surface of the a-C:H underlayer as evident from its cross section image. These structures are small but are well distributed over the surface of the film. As R_{UL} is increased to 2.027, its cross sectional image shows that the structures remain almost the same except for an obvious increase in height. These too protrude out on the surface of the a-C:H underlayer films. However, the surface image indicates that as they grew, there is a tendency to conglomerate to form solid-like centers. The ns- CN_x formed on the a-C:H underlayer with R_{UL} of 2.475 changes to more compact structures embedded in the a-C:H underlayer. These are shorter than those on the a-C:H underlayer with R_{UL} of 2.027 but, akin to the latter, are also formed randomly over the surface of the a-C:H underlayer film.

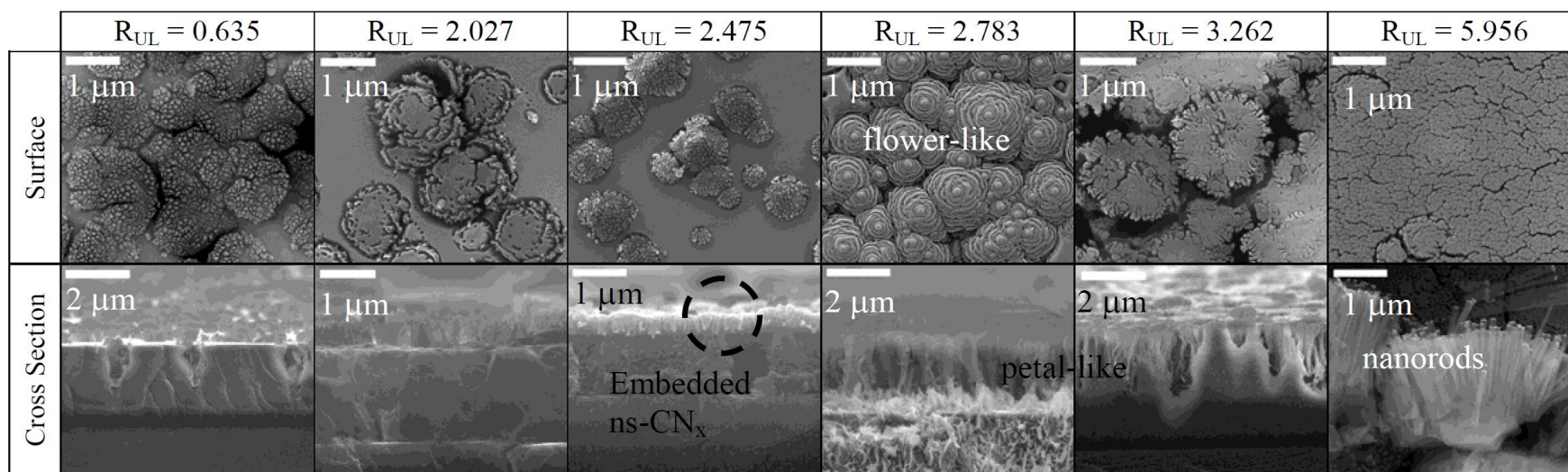


Figure 4.23: Surface and cross-section images of ns:CN_x deposited by RFPECVD at different RF power of a-C:H underlayer.

The ns-CN_x structures formed on the underlayers with R_{UL}, of 2.783, 3.262 and 5.956, all shows significantly different structures. There appears to be some common features; firstly these are formed as vertically aligned structures and secondly, they are formed uniformly over the underlayer film, especially for R_{UL} of 5.956 as shown in Figure 4.24. Nevertheless, each structure is unique. The ns-CN_x formed on the a-C:H underlayer with R_{UL} of 2.783 forms vertical petal-like features when viewed from the cross section image and are arranged into flower-like nanostructures as shown by the surface image clearly depicted in Figure 4.25. Upon enlarging the cross sectional image of the ns-CN_x formed on the underlayer with R_{UL} of 3.262, the structures show similar petal-like structures as seen earlier for the underlayer with R_{UL} of 2.783. However, these smaller petal-like structures conglomerate to form solid-like bulk structures as evident from both the surface and cross sectional images. Among all these ns-CN_x, the ns-CN_x formed on the a-C:H underlayer with R_{UL} of 5.956 remains the most interesting. These ns-CN_x are formed as vertical aligned rigid nano-rods, distributed uniformly in a large area over the substrate. These nano-rods have average lengths and diameters of $3.38 \pm 0.07 \mu\text{m}$ and $84 \pm 17 \text{ nm}$, respectively, giving an aspect ratio of approximately 40.

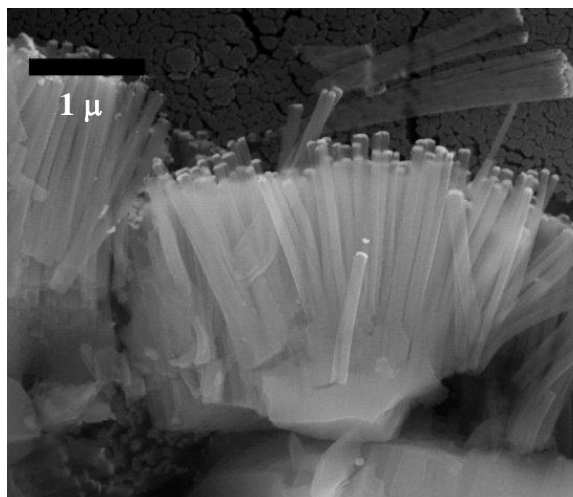


Figure 4.24: FESEM cross section image for ns-CN_x deposited on pre-deposited a-C:H underlayer with surface roughness of 5.956.

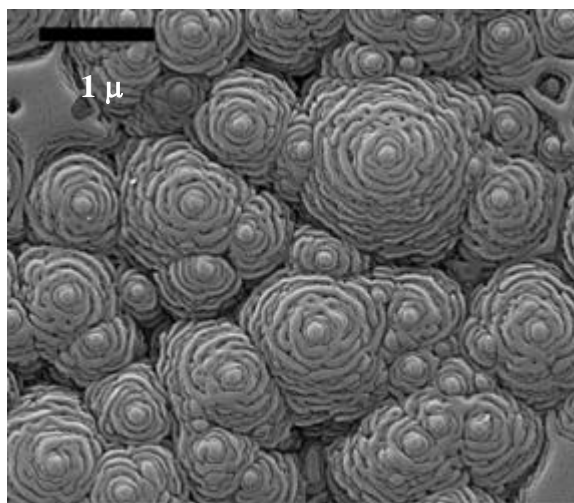


Figure 4.25: FESEM surface image for ns-CN_x deposited on pre-deposited a-C:H underlayer with surface roughness of 2.783.

4.3.2.2 Auger electron spectroscopy measurement of CN_x nanostructures

AES analysis was done to determine the chemical composition of C and N in these ns-CN_x. Figure 4.26 presents the variation of N/C ratio as a function of R_{UL}. This

effect is contributed by the incorporation of N atoms in the film structure. N incorporation increases with the increase in R_{UL} .

At lower R_{UL} , the N/C ratio is in the range of 0.0635-0.2475 may be due to less N_2 gas dissociation at corresponding RF power. Furthermore, the N incorporation is the highest in the ns- CN_x grown on the underlayer with the highest R_{UL} of 5.596 nm. These indicate that the isonitrile formation contributes significantly to the overall formation of the CN_x nanorods which are not formed on the other a-C:H underlayer with lower R_{UL} that will be described in next section.

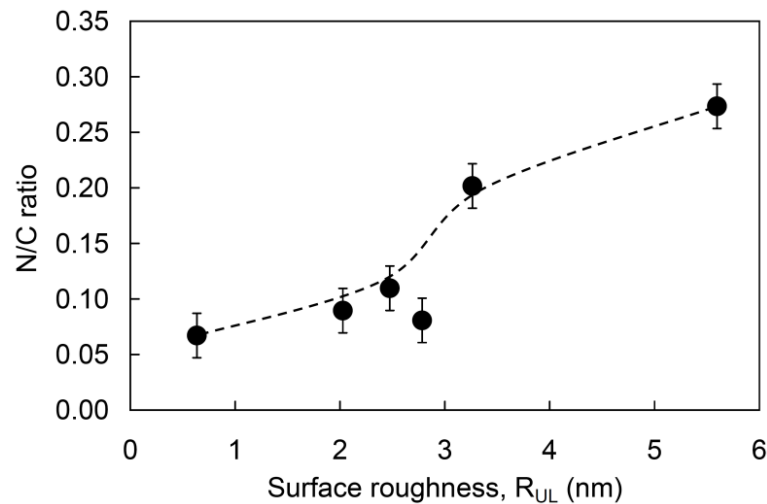


Figure 4.26: Variation of nitrogen to carbon N/C ratio of ns- CN_x films as a function of surface roughness of a-C:H underlayers.

There appears to be a strong relationship between the N/C ratio, R_{UL} and its corresponding structure. This also indicates that template effect of the surface morphology influence the N incorporation into the film. The N incorporation also appears to determine the structure of the ns- CN_x film. Thus, the R_{UL} and also its corresponding P_{UL} indirectly determine the ns- CN_x formed.

4.3.2.3 FTIR spectra of CN_x nanostructures

The chemical bonding in the ns- CN_x grown on the a-C:H underlayer is shown in the FTIR spectra depicted in Figure 4.27. The spectra can be divided into three main regions. These include sp^2 C peaks positioned in the frequency region of 1100-1700 cm^{-1} , the sp^1 phases related to $C\equiv N$ at wavenumber of 1900-2500 cm^{-1} and CH_n bands within the region of 2800-3050 cm^{-1} (Fanchini et al. 2005; Mutsukura 2001; Ritikos et al. 2009). For clarification, Figure 4.28 presents individual spectra for each region.

The spectra look similar to the FTIR spectra of the a-C:H underlayer except that these spectra produce a broadening and increase in the intensities of the sp^2 C peaks positioned in the frequency region of 1100-1700 cm^{-1} . This is attributed to the formation of various CN bonds particularly C=N band which overlaps the C=C and sp^2 C bands in the region of 1620-1650 cm^{-1} and 1300-1350 cm^{-1} , respectively, together with the C=N peak at 1220-1265 cm^{-1} (Motta & Pereyra, 2004).

Consequently the intensities of the CH_n bands within the region of 2800-3050 cm^{-1} appears relatively weaker. This represents the relative contribution of the CN layer (as the a-C:H underlayer should still contribute to these spectra). Thus, while the sp^2 C bands within the range of 1100-1700 cm^{-1} becomes stronger and broader due to the added contribution of the CN layer, the CH_n bonds which are contributed largely by the a-C:H underlayer appears relatively weaker.

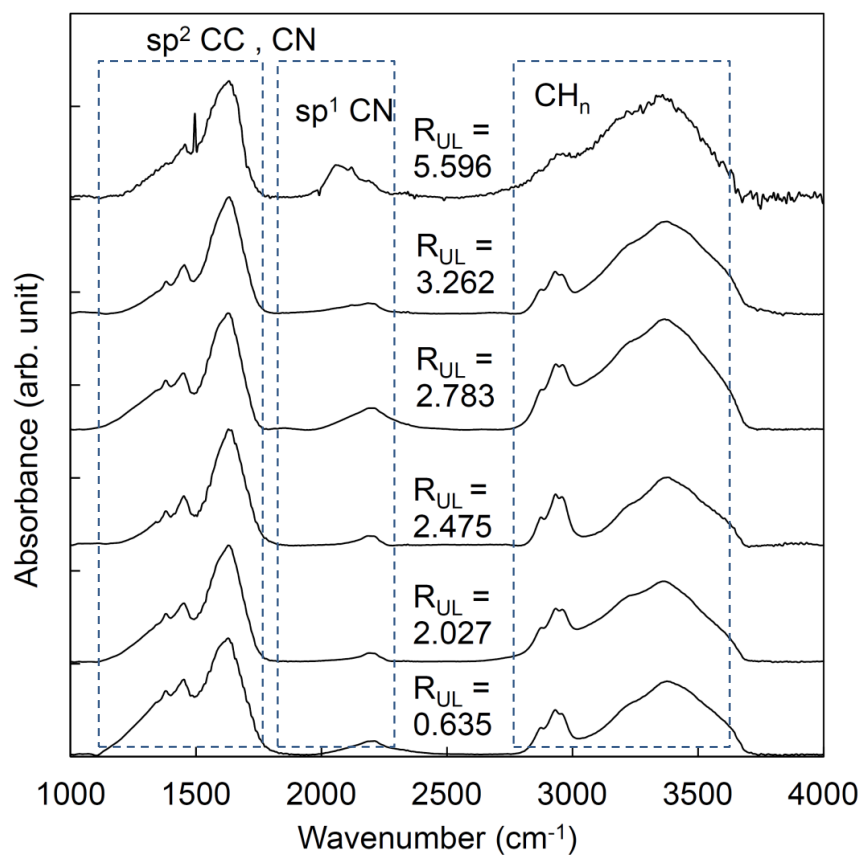


Figure 4.27: Variation in FTIR absorbance spectra as a function surface roughness of a-C:H underlayers.

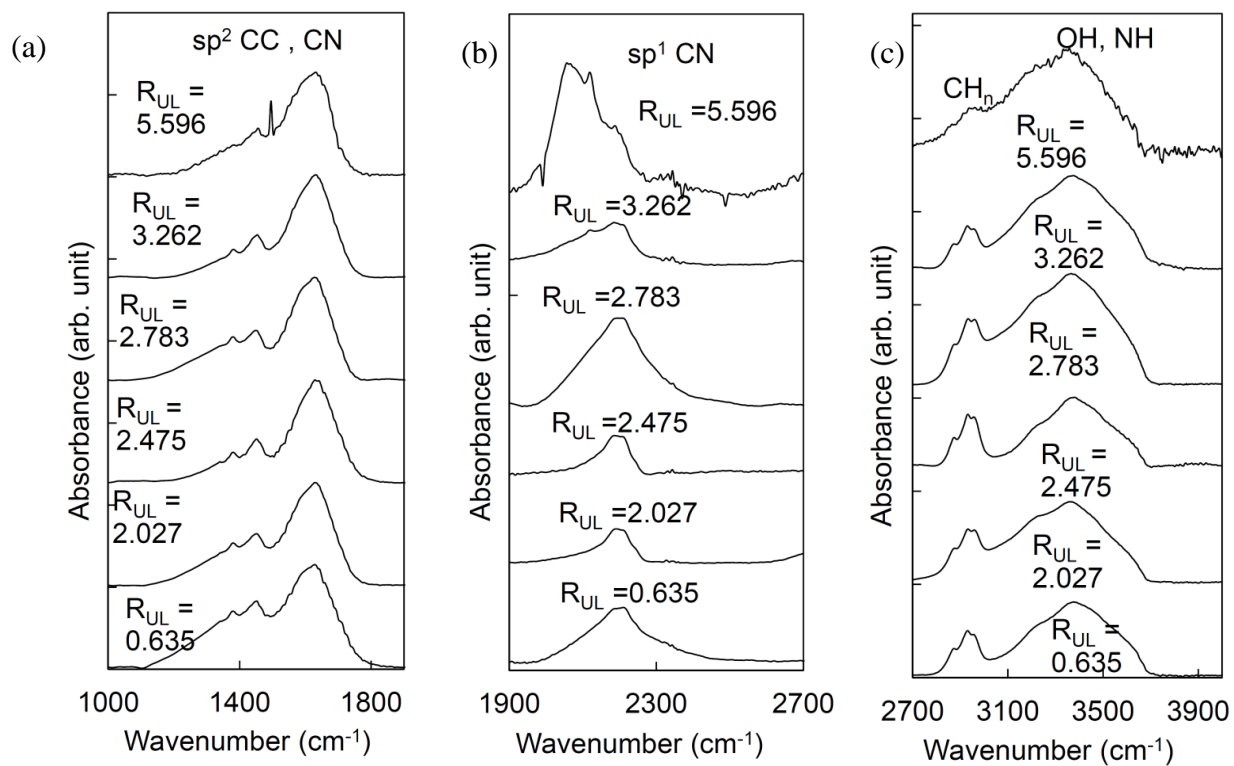


Figure 4.28: The FTIR spectra for CN_x nanostructures deposited on a-C:H underlayers with different roughness in the range of (a) sp^2 , (b) sp^1 and (c) sp^3 phases.

It was observed that the ns-CN_x deposited on the a-C:H underlayer with the highest R_{UL} of 5.596 shows the lowest intensity of the CH_n bonds and is consistent with the sp² C for the underlayer film (Figure 4.19). This indicates that the chemical bonding preference of this ns-CN_x film is induced by the bonding properties of their a-C:H underlayer film. In this sense the presence of the cone-like structures in the a-C:H underlayer films, believed to be formed by clustering of the sp² C species in the film, may act as the template on which the growth of the nano-rods are induced. Selective etching by N⁺ ions bombardments removes the softer polymeric C structures surrounding sp² C clusters thus forming the observed ns-CN_x (Ritikos et al. 2011). This is also true for the other films but the effect works at varying degrees. Another important aspect which could be deduced from these spectra is the appearance of the nitrile and/or isonitrile bonds in the frequency range of 1900-2500 cm⁻¹ for these ns-CN_x films as shown in Figure 4.29.

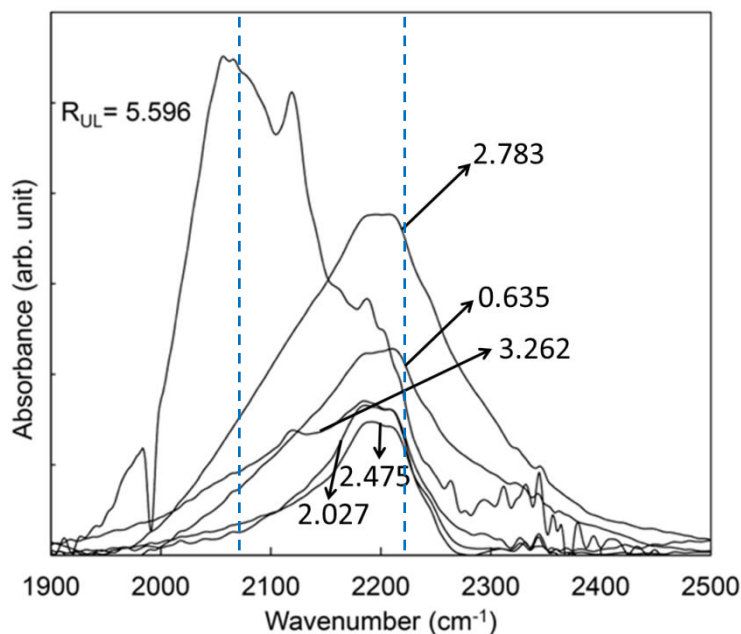


Figure 4.29: The FTIR spectra in the range of 1900-2300 cm^{-1} of ns-CN_x as a function of R_{UL} a-C:H underlayers.

The band superposes isolated and/or fused aromatic rings bonded either to isonitrile ($-\text{N}\equiv\text{C}$) at 2105 cm^{-1} or nitrile ($-\text{C}\equiv\text{N}$) at 2215 cm^{-1} , hydrocarbon molecules which includes C_2H_5 at 2160 cm^{-1} and CH_3 at 2190 cm^{-1} bonded to isonitrile ($\text{N}\equiv\text{C}$), and hydrocarbon groups (CH_3 , C_2H_5 , etc.) bonded to nitrile ($-\text{C}\equiv\text{N}$) located as a single peak at 2245 cm^{-1} (Mutsukura and Akita 1999). Generally, the CN_x films deposited on the a-C:H underlayer films with R_{UL} in the range of 0.63-3.26 nm show a dominant peak attributed to isonitrile bonded to aliphatic at approximately 2190 cm^{-1} . In contrast, the nanorods shows preferential formation of isonitriles bonded to aromatic rings at 2105 cm^{-1} . The differences is seen in the formation of aromatic rings attributed by the increase in sp^2 C bonds in the a-C:H films and CN_x nanorods. From our previous studies, we also deduce that isonitrile bonds induce a partial charge within these nanostructures, and together with the electric field imposed by the RF plasma results in the vertical alignment. Figure 4.30 shows the example of Gaussian fitting related to those

bonds in the region of $2000\text{--}2300\text{ cm}^{-1}$ for a-C:H underlayers with surface roughness of 5.596 and 3.262.

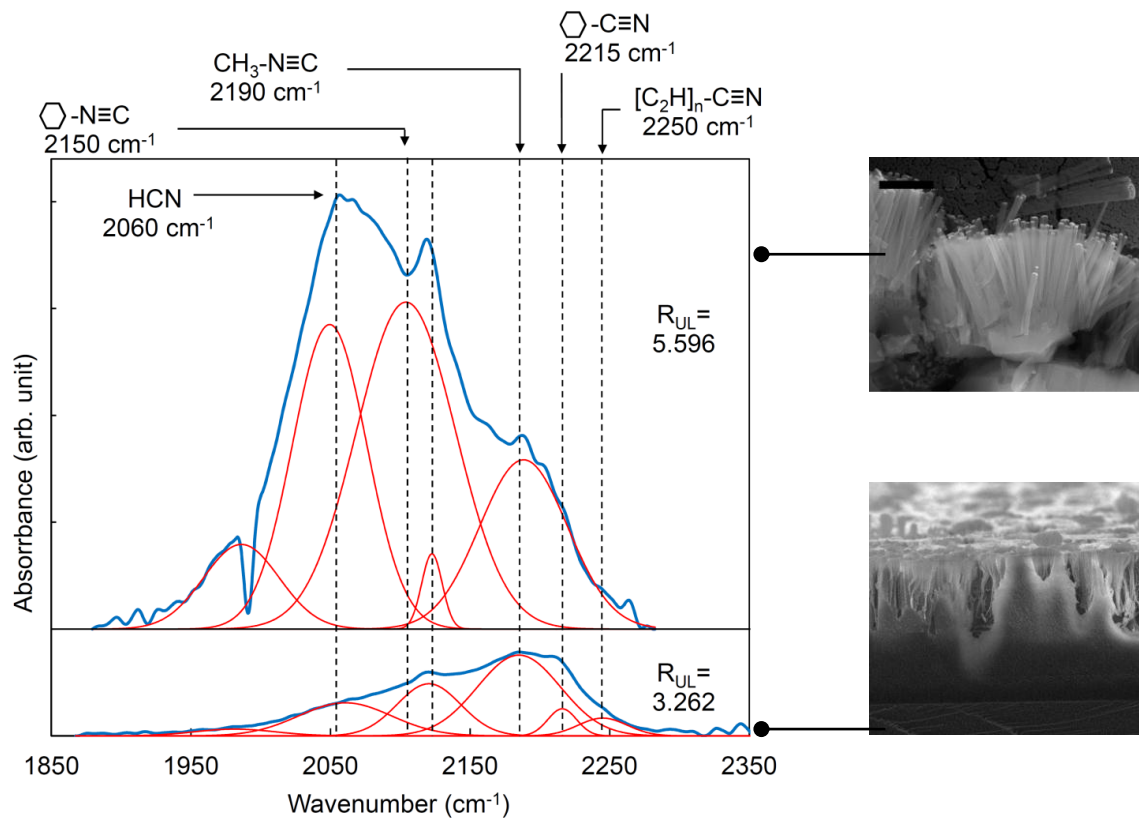


Figure 4.30: Gaussian fitting profiles for FTIR spectra in the region $2000\text{--}2300\text{ cm}^{-1}$ for a-C:H underlayers with surface roughness 5.596 and 3.262.

4.3.3 Summary

The effects of RF power on the growth rate, surface morphology and chemical bonding of the a-C:H underlayer film have been studied. Consequently, the morphology and structural properties of ns-CN_x film formed on these underlayer film were investigated. The RF power indirectly determines the formation of the sp² C clusters and surface morphology of the a-C:H underlayer. The variation in surface roughness and morphology of the a-C:H underlayer result in the formation of ns-CN_x with unique features such as flower-like structures and vertically aligned rigid nano-rods. The sp² C

clusters in the a-C:H underlayer acted as templates, where selective etching of the softer polymeric C structures surrounding or within the clusters by N^+ ion bombardment in the different ns-CN_x on the a-C:H underlayers occurred. High N incorporation and the preferential formation of isonitrile bonds is the condition that forms vertically aligned rigid carbon nitride nanostructures.

4.4 Effects of Hydrogen Treatment on the a-C:H Underlayer and the Resulting CN_x/ a-C:H Film

The third part of the study emphasize the effects of different time duration of H₂ plasma treatment on the a-C:H underlayers, deposited for 10 minutes and at RF power of 100 W, also on the properties of the resulting CN_x/a-C:H nanostructures. There are 4 sets of sample including the as-deposited a-C:H underlayer (without H₂ plasma treatment), 3, 5 and 10 minutes treated a-C:H underlayers and their corresponding CN_x films. The surface morphology, chemical, structural and elemental composition properties of the films were studied.

4.4.1 Effect of H₂ Treatment Time Duration on a-C:H Underlayers

4.4.1.1 Surface roughness and surface morphology of a-C:H underlayers

The surface morphology of the a-C:H underlayers were studied using AFM imaging. Figure 4.31 shows the AFM surface images of a-C:H underlayers, while the corresponding variation of surface roughness is presented in Figure 4.32. These were depicted as a function of the time duration of H₂ plasma treatment, t_H .

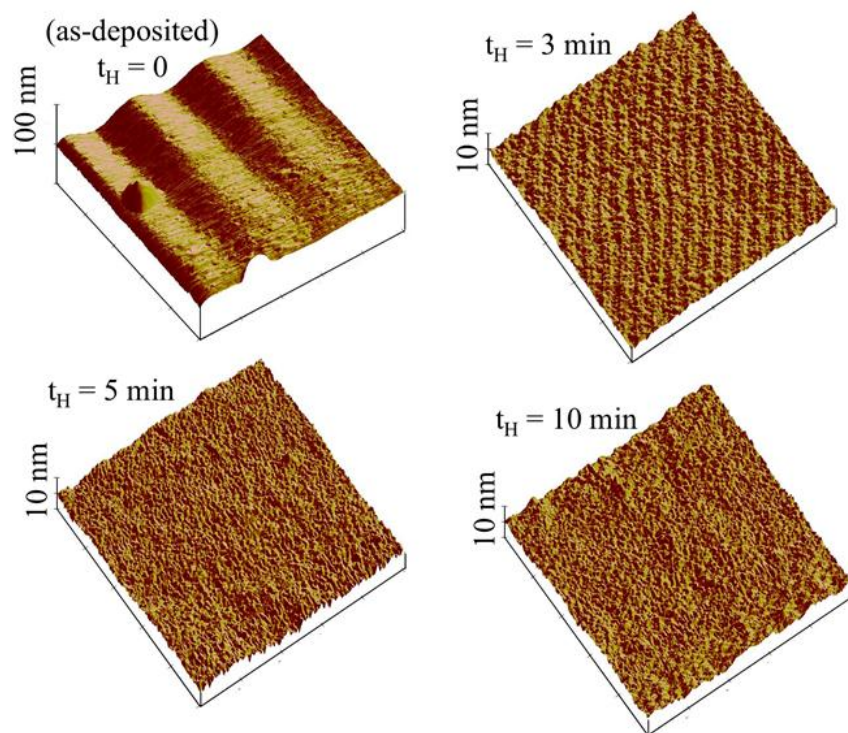


Figure 4.31: AFM surface morphology of a-C:H underlayers at various time duration of H₂ plasma treatment.

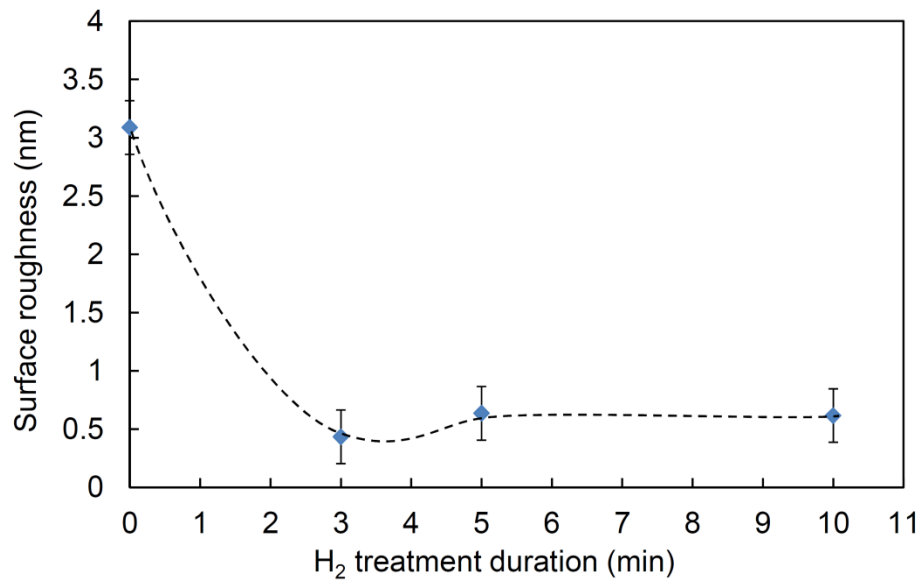


Figure 4.32: Variation of surface roughness of a-C:H underlayer as a function of t_H . Line is a guide to the eyes.

The surface morphology of the as-deposited a-C:H underlayer shows homogeneous grains with scattered cone-like structures perpendicular to the surface. This film shows the highest surface roughness at 3.087 nm. After t_H of 3 minutes, the surface structure becomes much smoother and the cone-like structures disappear. This is due to the effect of H₂ bombardment onto the surface of the film during the treatment. Hopf et. al. also reported that H ion bombardment on hydrocarbon films influence the significant reduction in film thickness due to ion-induced dangling bond formation of hydrogen atom at the surface of the film (Hopf, von Keudell and Jacob 2003). This explains the dramatic decrease in the surface roughness of this a-C:H underlayer to 0.433 nm at t_H of 3 minutes.

The surface image of a-C:H underlayer films treated at t_H of 5 and 10 minutes did not change significantly compared to the changes seen from the as-deposited to t_H of 3 minutes. However, the surface roughness increases slightly to 0.635 and 0.616 nm, respectively. The increase in the surface roughness indicates a subtle change in the H

ion bombardment on the surface. It is believed that the H plasma etching effect is time dependent, and becomes less dominant since weakly bonded sites would have been removed by this t_H . On the other hand, the atomic hydrogen density increases when the a-C:H underlayers experienced longer t_H . The energy of the impinging H ions is dependent on the amount of collision that occurs in the plasma. When their energies are larger than the critical value of atomic displacement in the a-C:H underlayer, the ions will be able to penetrate the outermost surface of a-C:H underlayer. This process is called subplantation (Robertson 2002). During this process, the ions will be integrated into the bulk volume of the subsurface thus contributing to the morphology of a-C:H underlayer at longer t_H . It appears that the subplantation of the H atoms and ions is dependent on t_H and increase with t_H after the initial 3 minutes.

4.4.1.2 *Chemical bonding properties of a-C:H underlayers*

The chemical bonding of the a-C:H underlayers as a function of t_H were studied using FTIR. These FTIR spectra are shown in Figure 4.33. The spectra can be divided into two main regions at wavenumber ranges of 1200-1900 cm^{-1} and 2700-3800 cm^{-1} . The absorption bands at 1200-1900 cm^{-1} are assigned to sp^2 phase CC bond; while the band in the region of 2700-3800 cm^{-1} are assigned to the bonds of CH_n groups and O-H (Mutsukura and Akita 1999).

These two major regions of the FTIR spectra were deconvoluted and presented in Figure 4.34. For the region within the range of 1200-1900 cm^{-1} , the spectra were fitted for band corresponding to sp^2 C, Raman D, sp^3 CH, Raman G, C=C and C=C stretching at 1350, 1380, 1450, 1580, 1650 and 1700 cm^{-1} , respectively as shown in Figure 4.34 (a). Figure 4.34 (b) shows the second region in the range of 2700-3200 cm^{-1} , whereby the spectra represent sym sp^3 CH_2 , sym sp^3 CH_3 , asym sp^3

CH_2 , asym $\text{sp}^3 \text{CH}_3$ and $\text{sp}^2 \text{CH}$ at 2835, 2875, 2930, 2960 and 3020 cm^{-1} , respectively (Fanchini et al. 2005; Pereira et al. 2006; Ritikos et al. 2009a).

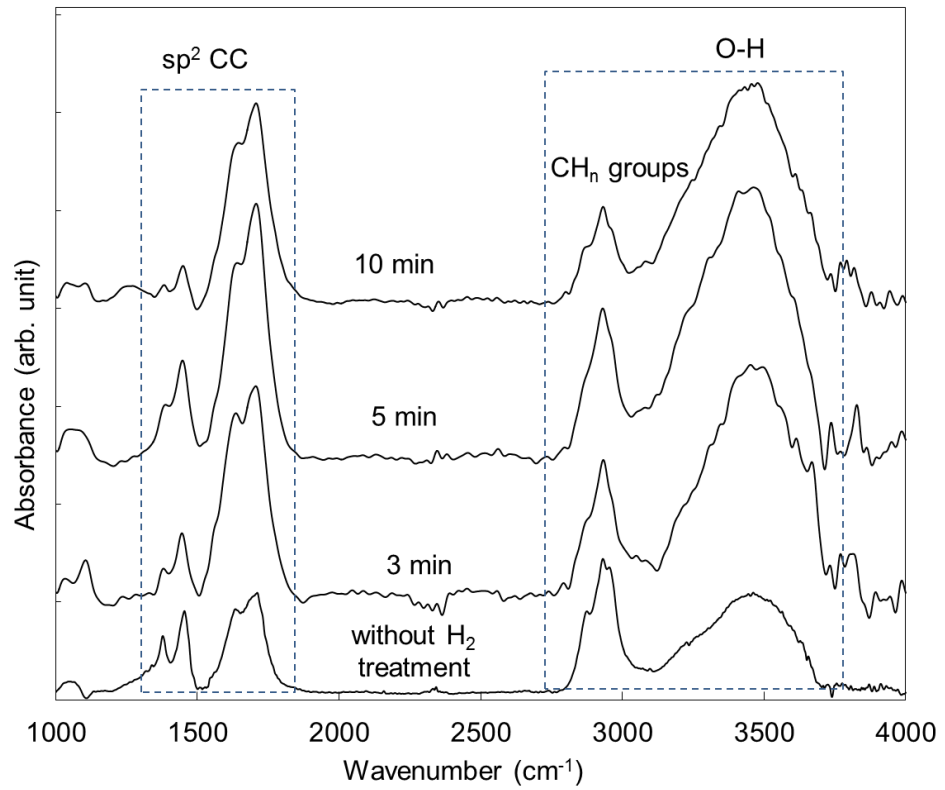


Figure 4.33: FTIR spectra of a-C:H underlayers as a function of t_{H} .

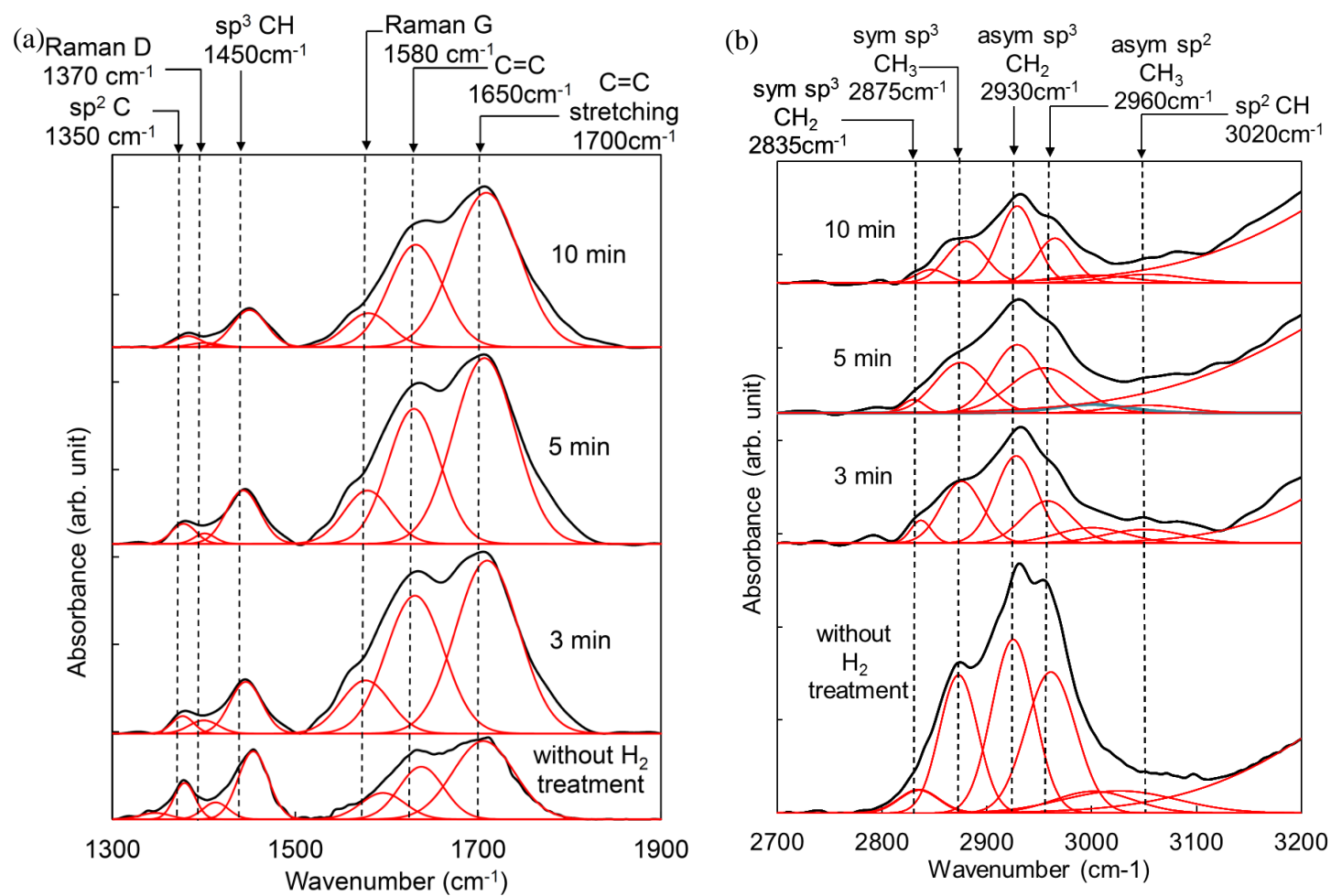


Figure 4.34: Variation of FTIR spectra for a-C:H underlayers prepared by RFPECVD as a function of t_H in regions of (a) 1300-1900 cm⁻¹ and (b) 2700-3200 cm⁻¹.

The deconvoluted FTIR spectra depicted in Figure 4.34 show that the functional groups remain intact even with the H₂ treatment on these a-CH underlayer films. In particular, the sp² phase region remains almost the same even after t_H of 10 minutes. A similar deduction could be made for the CH_n region although it is seen that there are slight changes in the relative peak intensities of the sp³ CH₂ and sp² CH₃ peaks at 2930 and 2960 cm⁻¹, respectively. However a more significant change is seen for the overall spectra as shown in Figure 4.33. While the sp² CC band does not change, a significant decrease is seen in the CH_n particularly when compared between the as deposited a-C:H and after t_H of 3 minutes.

The decrease in CH_n indicates a decrease in H bonds and this is in line with the proposed H ion bombardment effect on the film surface which creates dangling bonds (Hopf, von Keudell and Jacob 2003). It appears that the ion bombardment would preferentially reduce this CH_n bonds. With the increase in t_H, the CH_n bond intensities remain almost the same which support the saturation in the etching effect of the H bombardment that leads instead to the subplantation of these ions or atom.

4.4.1.3 Raman analysis

The Raman spectra of these a-C:H underlayers were obtained in the Raman shift range of 1000–2000 cm⁻¹ using UV excitation of 325 nm. The raw Raman spectra depicted in Figure 4.35 (a) shows two prominent peaks at around 1380 and 1600 cm⁻¹ assigned to their D and G band, respectively. The Raman spectrum of the as-deposited a-C:H underlayer has strong PL background resulting in a positive slope of the spectrum. This was also observed by Marchon et. al in hydrogenated carbon films prepared by DC-magnetron sputtering technique (Marchon et al. 1997). The PL background is due to hydrogen saturation of non-radiative recombination centers in the

film (Escobar-Alarcón et al. 2005) which promotes the PL emission in this material. The increase in H bond in a-C:H usually leads to an increase in PL emission. In contrast having undergone H treatment even as early as t_H of 3 minutes the PL background reduces significantly which completely eliminates the slope. This indicates a reduction in H bond in the film in line with the deduction in FTIR and AFM analysis.

The corrected and fitted Raman spectra for a-C:H underlayers as a function of t_H are shown in Figure 4.35 (b), while the corresponding fitting parameters including the variations in G and D peak positions, FWHM and I_D/I_G ratio are shown in Figure 4.36. In general, the G peak position lies at a constant wavenumber approximately 1597 cm^{-1} regardless of t_H . This value being higher than that of graphite (1550 cm^{-1}) though not exceeding the limit of graphitic carbon implies that these films have high degree of graphitization but also exhibit characteristic of olefinic (chain sp^2 group) with shorter bond length (Gilkes et al. 1998). However it is the D band which best explains the changes in the film with t_H . The D peak red-shifted drastically with t_H particularly from the as-deposited to the initial t_H of 3 minutes. The red-shift in D peak could be attributed to either a decrease in the number of ordered aromatic ring or a strained or curved graphitic plane (Ferrari and Robertson 2000; Yu et al. 2002). In contrast, the $FWHM_D$ increases drastically with t_H particularly from the as-deposited to the initial t_H of 3 minutes. This implies a broadening in the width of the D peak which is correlated to the increase in disorder due to a distribution of clusters with different orders and dimensions. The changes in the initial t_H of 3 minutes coincides with the proposed etching and reduction of H bonds on the film surface with H ion bombardment. Thus it can be deduced that in the initial t_H of 3 minutes, there appears to be an increase in disorder due to the breaking of the CH bonds, which in turns causes a change in the number of aromatic rings and a redistribution of the clusters containing these rings. It can also be stipulated that the redistribution of the clusters also causes the changes in

the surface morphology of the films seen in the AFM imaging whereby the surface was smoothen out and the roughness decreases significantly. It is deemed true that the clusters in the film consisting of sp^2 domains may be taken as ordered domains by Raman, these clusters are the cone-like structures on the surface which induce the high roughness in AFM analysis.

With the increase in t_H above 3 minutes, the D peak blue-shifted slightly, while the $FWHM_D$ decreases, implying an slight increase in ordering and an increase in the number or size of the ordered sp^2 aromatic ring clusters. Indeed this is in-line with the slight increase in the surface roughness (Figure 4.32) which further supports the deduction proposed concerning the effect of the H ion treatment.

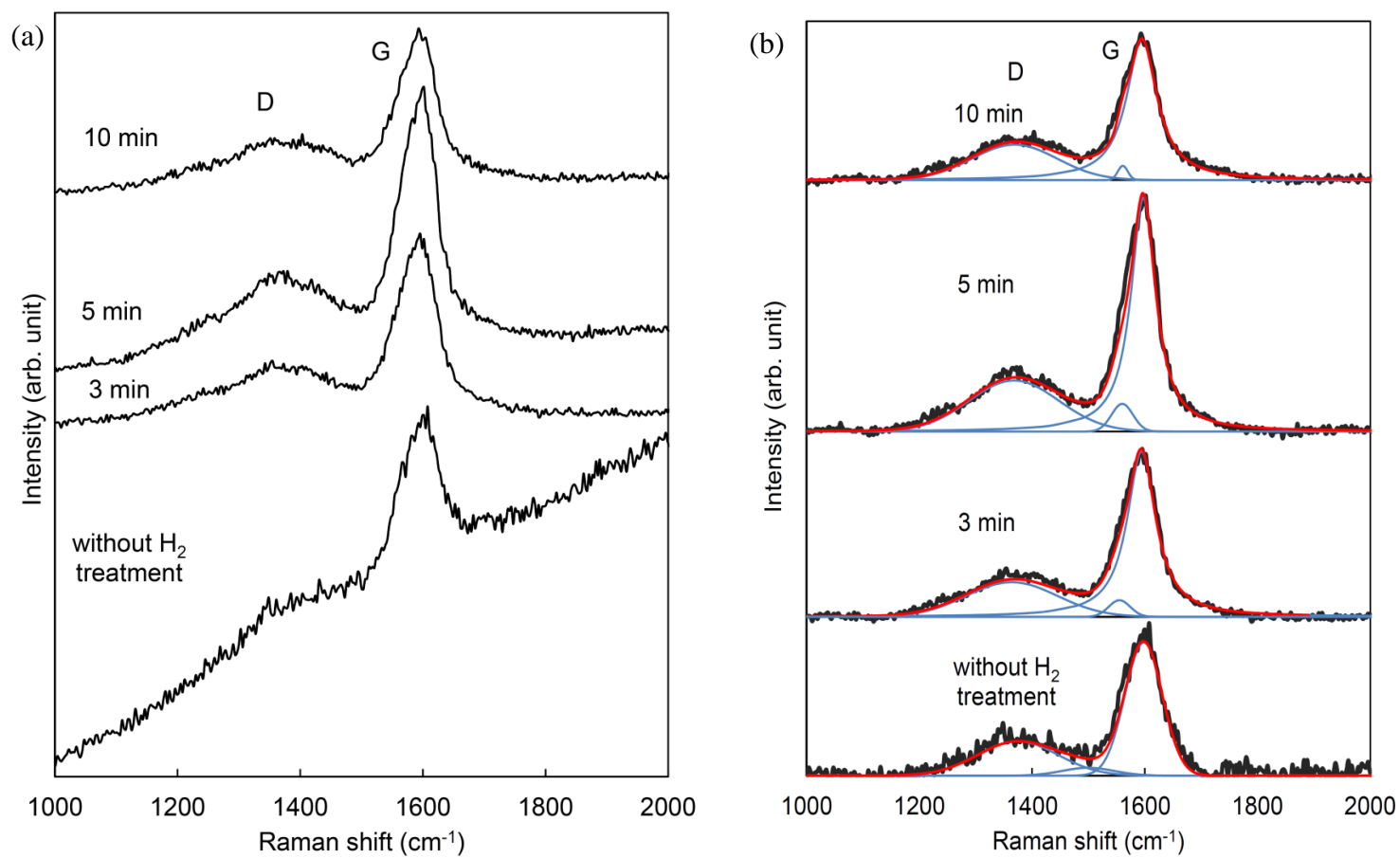


Figure 4.35: The raw Raman spectra with strong background (a) and the Raman spectra after the background extraction (b) for a-C:H underlayers as a function of t_H .

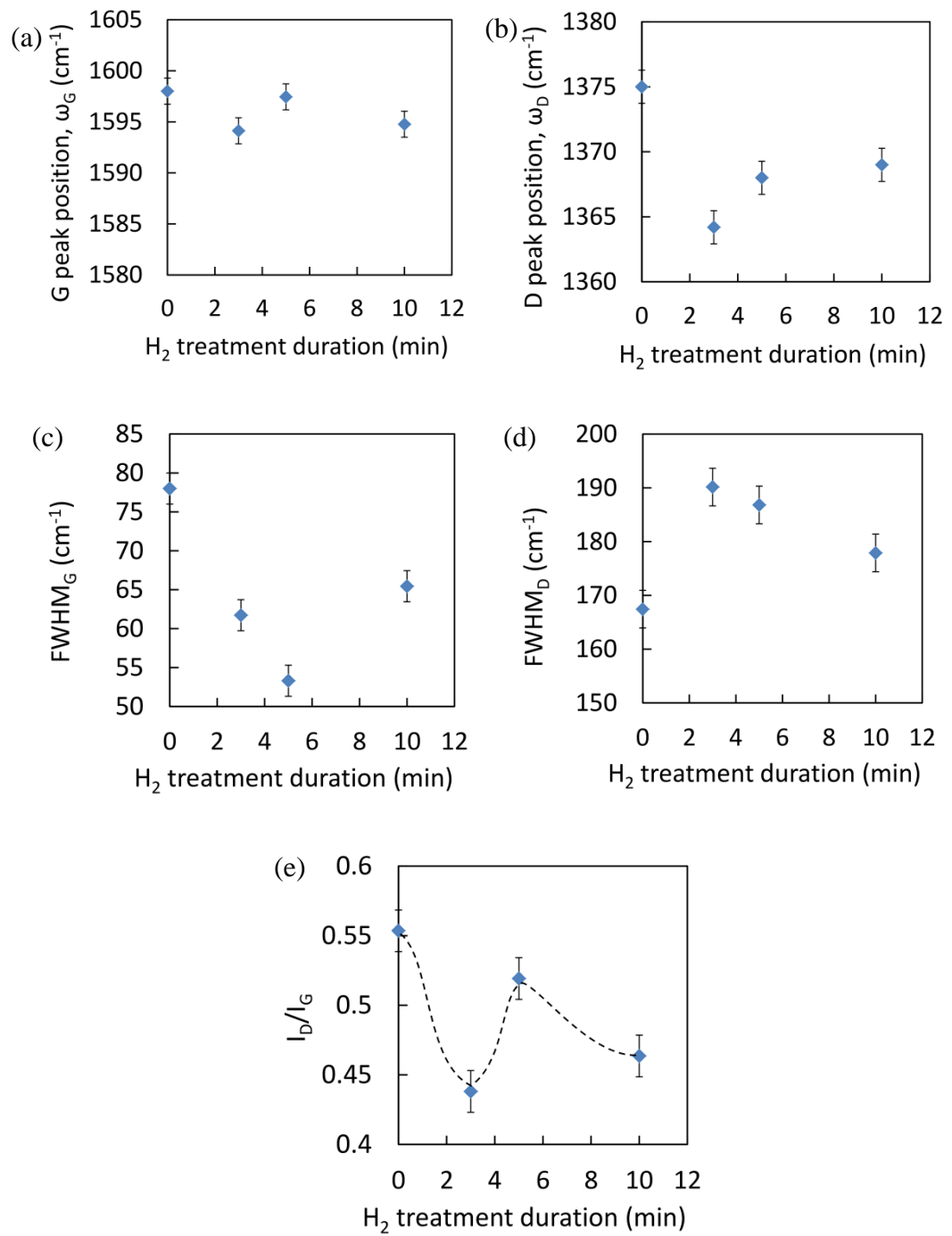


Figure 4.36: Raman analysis of a-C:H underlayers prepared as a function of hydrogen treatment duration. Line is guide to the eyes.

4.4.2 Effect on Resulting $\text{CN}_x/\text{a-C:H}$ Formation

4.4.2.1 *Surface and cross-sectional images*

The next step is to investigate the formation of ns- CN_x deposited onto these a-C:H underlayers treated at different t_H . The surface and cross-sectional FESEM images of these ns- $\text{CN}_x/\text{a-C:H}$ are presented in Figure 4.37 as a function of t_H . The ns- CN_x prepared on as-deposited a-C:H underlayer formed petal-like structure which conglomerate to form solid-like bulk structures. The ns- CN_x grown on a-C:H underlayer treated at 3 minutes shows similar structures as those deposited on the as-deposited a-C:H underlayer. However these are formed as distinct vertical fiber-like structures which are well separated as compared to the conglomeration of those mention for its predecessor. Conversely, the structures of the ns- CN_x evolved with the increase of t_H above 3 minutes. It is seen that the ns- $\text{CN}_x/\text{a-C:H}$ formed at t_H of 5 minutes were produced as well defined short nanotips. The length and distribution of these CN_x nanotips are quite uniform with the average length and diameter calculated from the cross-sectional image to be approximately 125 ± 1 nm and 78.0 ± 0.2 nm, respectively. With the increase in t_H to 10 minutes, the ns- $\text{CN}_x/\text{a-C:H}$ forms similar structure as those at t_H of 5 minutes but the length, diameter and distribution appears to change. The length and diameter of these nanotips appear to increase though the growth appears not to be so uniform with large disparities where the length varies between 20 to 211 nm and the diameter between 39 to 60 nm. It is also noted that the ns- CN_x produced on the as-deposited a-C:H and at t_H of 3 minutes appears to grow as part of the underlayer film. No clear distinction could be made to identify the boundary between the root of the ns- CN_x and the top layer of the a-C:H underlayer. In contrast, the boundary between the CN_x nanotips formed at t_H of 5 and 10 minutes is easily distinguish.

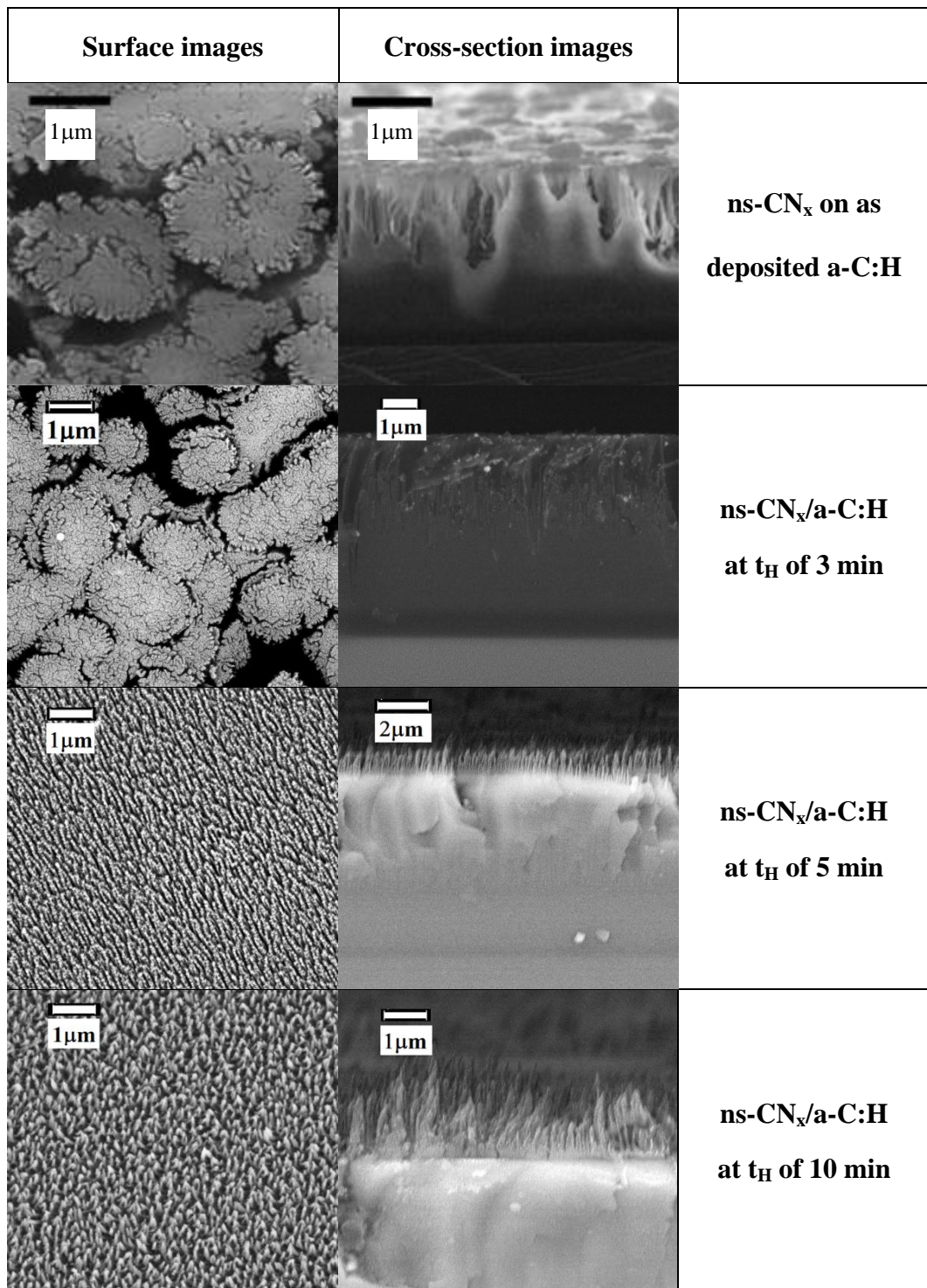


Figure 4.37: The surface and cross-section images of ns-CN_x subsequently deposited on different t_H a-C:H underlayers.

4.4.2.2 Auger electron spectroscopy measurement of ns-CN_x

The chemical composition of the ns-CN_x was determined as the relative concentration of N and C (N/C) calculated from AES measurement. Figure 4.38 shows the variation of N/C ratio of these ns-CN_x as a function of different t_H for the treatment of a-C:H underlayers. The ns-CN_x grown on the as-deposited a-C:H underlayer has the highest N/C ratio at 0.2. With the H₂ treatment of the a-C:H underlayer and increase in t_H the N/C ratio of the ns-CN_x formed reduces gradually after the initial t_H of 3 minutes. This indicates a significant decrease in N incorporation in the ns-CN_x with the H treatment of the a-C:H underlayer. From the previous sections on the study of rf power and deposition duration, it was seen that CN_x nanorods were produced at the high a-C:H surface roughness and highest N/C ratio of the ns-CN_x, which was correlated to presence and ordering of the sp² clusters. In contrast, with the H₂ treatment on the a-C:H underlayers, CN_x nanotips are formed at low surface roughness while having low N/C ratio. Indeed, other researcher has reported the formation of CN_x nanotips formed on a-C:H films at high deposition temperature, having also low N content (Wang et al. 2005). According to these researchers, the N₂ in the plasma not only acts as reactants but also as etching agents. These N etching ions help to form the nanostructure but do not get incorporated into the film, thus keep the N incorporation low. However in this work there is an obvious dependence of the change in ns-CN_x and the surface condition of the a-C:H films brought about by the H₂ plasma treatment. The earlier studies on the Raman scattering of these a-C:H underlayer as a function of t_H implies a redistribution and decrease in the size and/or number of sp² clusters. These clusters may act as the nucleation sites for the growth of the ns-CN_x (Wang et al. 2011) and with the changes in these sp² clusters, the sites may become smaller and thus decreases the size of the ns-CN_x and forms the nanotips. The redistribution of the cluster by the H₂ plasma also results on the uniform distribution of the nanotips.

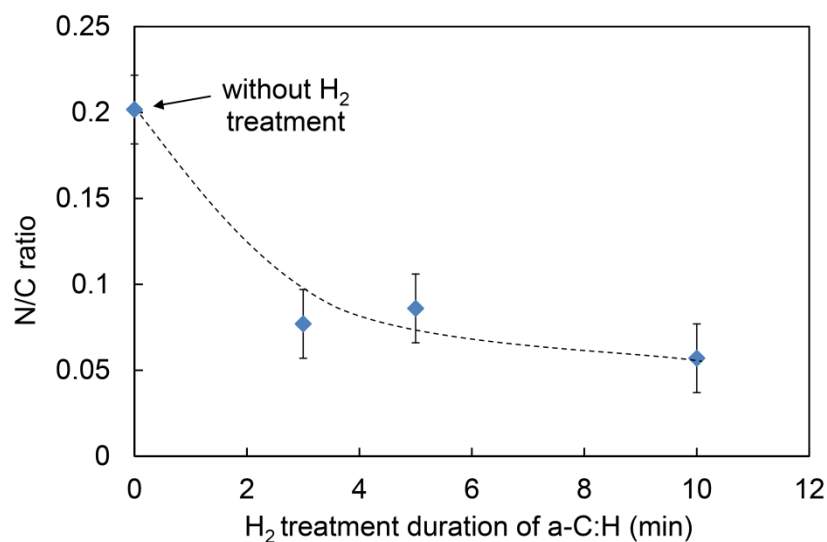


Figure 4.38: Variation of nitrogen to carbon, N/C ratio of ns-CN_x deposited on different t_H a-C:H underlayers.

4.4.2.3 FTIR spectra of ns-CN_x

FTIR analysis was carried out on the ns-CN_x grown on a-C:H underlayers as a function of t_H. The variation their spectra are shown in Figure 4.39 in the region of 1000–4000 cm⁻¹, while the three separated main regions within the range of 1100–1900, 2000–2300 and 2700–3800 cm⁻¹ are shown in Figure 4.40. Similar to the previous sections the first region within the range of 1100–1900 cm⁻¹ is attributed to sp²-C bonds including C-C, C-N, C=C and C=N. The second region in the range of 2000–2300 cm⁻¹ is assigned to the sp¹-C bonds including nitrile and isonitrile bonds. Lastly, the third region in the range of 2700–3800 cm⁻¹ represents sp³-C bonds, O-H and N-H groups (Motta and Pereyra 2004; Pereira et al. 2006; Ritikos et al. 2009b).

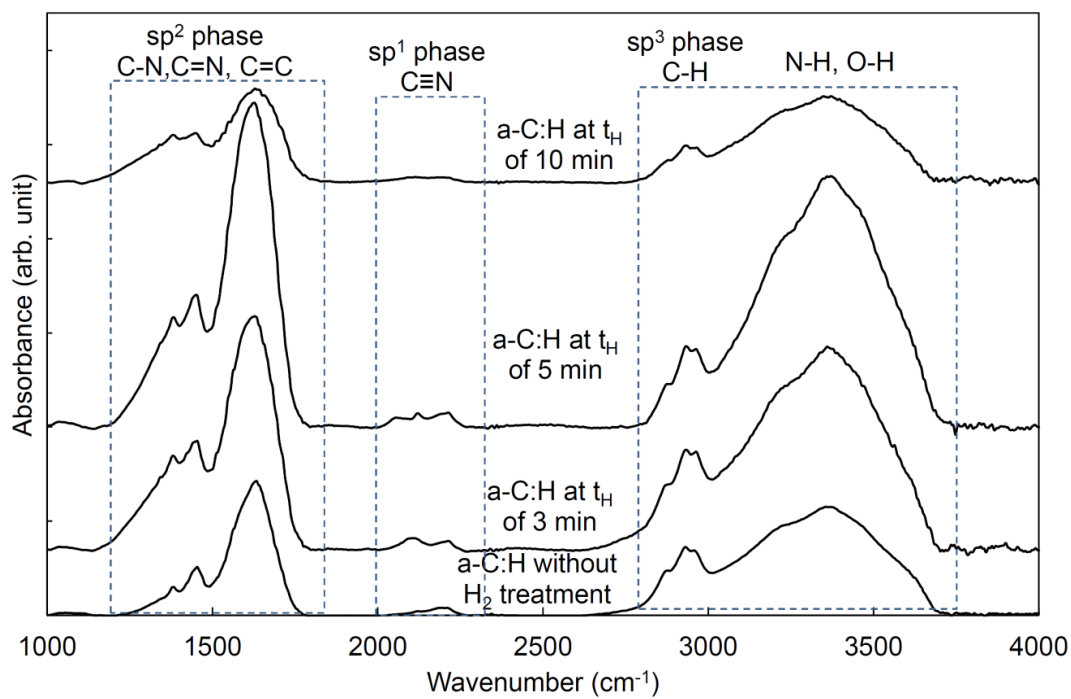


Figure 4.39: Variation in FTIR absorbance spectra of ns-CN_x as a function of H₂ treatment time of a-C:H underlayers.

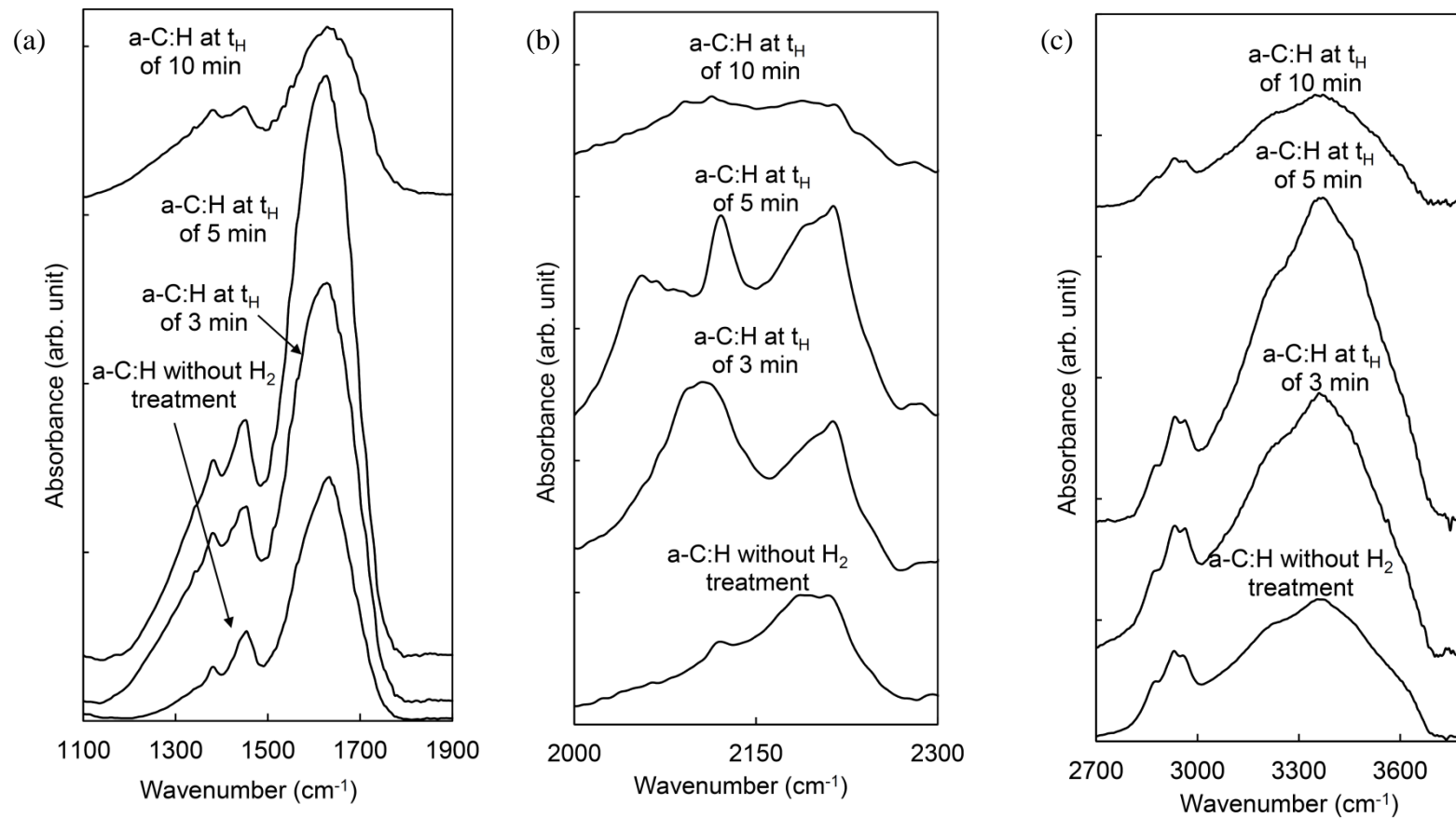


Figure 4.40: The FTIR spectra for ns-CN_x deposited on different t_H of a-C:H underlayers in the range of (a) sp², (b) sp¹ and (c) sp³ phases.

The sp^2 and sp^3 -C bonds within the ranges of 1100–1900 and 2700–3800 cm^{-1} , respectively, remains almost the same regardless of t_H . The remarkable difference was seen in the spectra range of 1900-2300 cm^{-1} as shown in the overlaid spectra shown in Figure 4.41 for this region. As mentioned before, this absorption band is related to nitrile and/or isonitrile ($C\equiv N$) bonds in the chemical structure of the material. The region consists of five overlapping bands associated to HCN at 2050 cm^{-1} , aromatic ring, C_2H_5 and CH_3 bonded to isonitrile ($-N\equiv C$) located at 2105, 2160 and 2190 cm^{-1} , respectively, together with the aromatic ring and hydrocarbon (CH_3 , C_2H_5 , etc.) bonded to nitrile ($-C\equiv N$) at 2215 and 2245 cm^{-1} , respectively (Mutsukura and Akita 1999). The deconvoluted peaks using standard Gaussian curve-fitting method are shown in Figure 4.42.

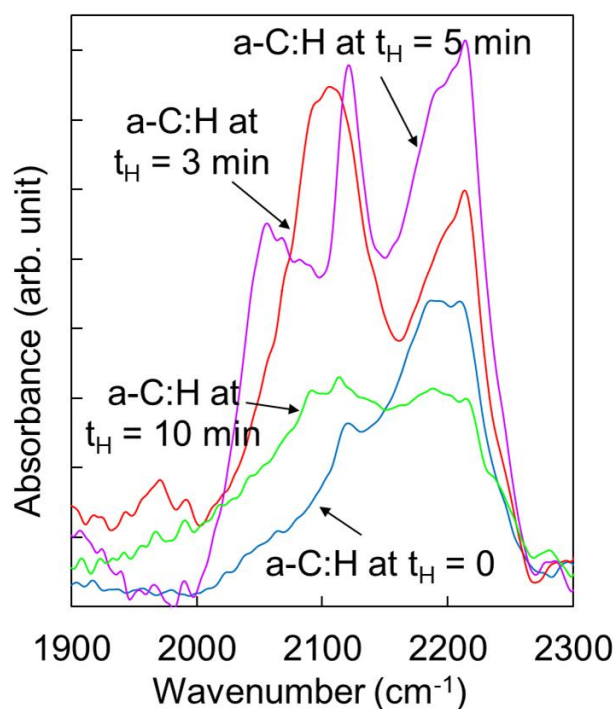


Figure 4.41: The FTIR spectra in the wavenumber range of 1900-2300 cm^{-1} of $ns-CN_x$ as a function of t_H a-C:H underlayers.

The deconvoluted spectra show a certain progression in the formation and preferential sp^1 -C bonds which makes up the ns-CN_x film. While isonitrile ($-N\equiv C$) bonds appear to be the preferential type compared to nitrile ($-C\equiv N$) for all these samples, the functional group which are attached to these bonds appears to be important. The ns-CN_x deposited onto the as-deposited a-C:H underlayer shows the preference of isonitrile bonded to aliphatic CH₃ ($CH_3-N\equiv C$), with the absorption peaks corresponding to isonitrile bonded to aliphatic C₂H₅ and nitrile bonded to aromatic rings being slightly less stronger.

In contrast, when these ns-CN_x were deposited onto the treated a-C:H underlayers, a significant shift in the preferential bonds to isonitrile bonded to aromatic rings is seen. Its absorption peaks strengthen considerably relative to the other bonding and indicates the increase in aromatic rings and thus the sp^2 clusters in the nanostructures. This signifies the importance of the aromatic rings in the formation of these vertically aligned nanostructures. This may also have led to the separation of the nanostructure strands which allows the nanofibers and nanotips to form apart rather than conglomerate like the ns-CN_x formed on the as-deposited a-C:H.

The variation in the spectra also shows a significant increase in the formation of HCN particularly for the ns-CN_x/a-C:H treated at t_H of 5 and 10 minutes. These elements could also be found in gaseous form and are normally volatile. Thus, it is probable that during the deposition, these elements may be a substantial part of the species in the plasma. Due to the volatile nature of this element, a large part of it may have been discarded as residual rather than being incorporated into the film. Thus this reduces the N incorporation in the film resulting in the low N/C ratio in the ns-CN_x/a-C:H with t_H .

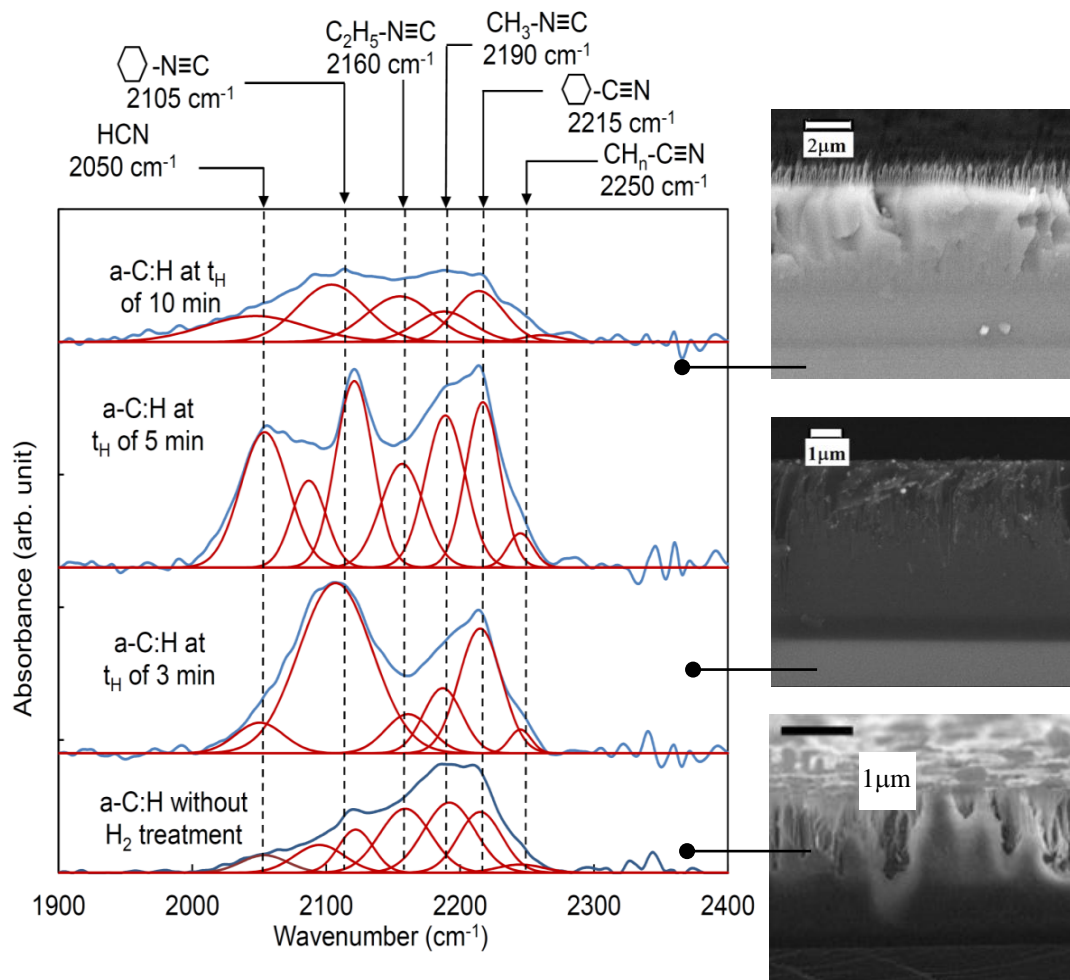


Figure 4.42 : Gaussian fitting profiles for FTIR spectra in wavenumber region of 1900-2400 cm^{-1} for a-C:H underlayer at t_H of 3, 5, 10 minutes and a-C:H underlayer without H_2 treatment.

4.4.3 Summary

The effects of H_2 treatment at various t_H on the structure and morphology of a-C:H underlayer were studied. H_2 treatment alters the surface morphologies of these films giving a smoother surface roughness with the increase in t_H . This was related to an increase in the disorder in the film due to the decrease in size and/or number of the sp^2 clusters and a redistribution of these clusters. This in turn was speculated to be due to the H etching and subplantation during H ion bombardment on the film surface. It was shown that by using this treatment method, the ns-CN_x deposited onto this underlayer

film could be manipulated. CN_x nanotips were successfully produced by RFPECVD at low temperature on a-C:H underlayers treated at t_H above 3 minutes. While all these ns- $CN_x/a-C:H$ films still shows the preferential formation of isonitrile bonds, the formation of distinct and separated strands were induce by the increase in aromatic rings in the film being bonded to these isonitrile. The decrease in the N incorporation with the formation of the nanotip may be due to production of volatile HCN in the plasma which did not contribute to the growth of the film.

CHAPTER 5 : CONCLUSION AND FUTURE WORKS

5.1 Conclusion

The deposition of various types of ns-CN_x through the modification of the structural properties of pre-deposited a-C:H underlayer has been studied. Both ns-CN_x and a-C:H underlayer films were successfully grown using RFPECVD technique without catalyst assistance at 100 °C. The ns-CN_x were fabricated at fixed deposition parameters including RF power, deposition duration, temperature, pressure and gases flow rate ratio while the deposition parameters of the a-C:H underlayer were varied using different preparation condition or post-deposition treatments. In the first two sets, ns-CN_x samples were deposited on a-C:H underlayers prepared using different deposition time duration (t_D) and RF power (P_{UL}) while in the third set, the ns-CN_x were deposited on a-C:H underlayers treated with H₂ plasma at different time duration (t_H). Under these conditions different types of ns-CN_x was formed including rigid and vertically aligned nanorods, fiber-like, flower-like nanostructures and nanotips.

The structural properties of the a-C:H underlayer influences the formation of ns-CN_x. In the study of deposition time duration of 5, 10, 15 and 30 minutes, it was found that high surface roughness of a-C:H underlayer induce the formation of rigid and vertically aligned CN_x nanorods. The a-C:H underlayer deposited for 10 minutes shows the highest surface roughness inducing the protrusion of broad-tipped cone-like features from the film surface. This was shown to be associated with the presence and ordering of sp² clusters in the a-C:H film.

The contribution of the surface roughness was further studied by varying the applied RF power. This effectively influences the ion bombardment effect on the

growing film surface and significantly changes the structural properties of the a-C:H underlayer. From the FTIR results, it was obtained that the film with highest surface roughness shows low CH_n band indicating low H content in the film attributed by the dominant sp^2 C bonds. This confirms the deduction made in the earlier study where the highest surface roughness of the a-C:H underlayer was due to the presence and ordering of sp^2 clusters in the a-C:H film. In this work, it was also established that by tuning the RF power, a unique flower-like CN_x nanostructures can be grown.

The study on the variation of H_2 plasma treatment time duration of 3, 5 and 10 minutes shows that H bombardment effects influenced the structural properties of the a-C:H underlayers. These results showed that the formation of dangling bonds as a results of bombardment of the surface with hydrogen atoms form a smooth surface of a-C:H underlayers as a consequent of the disorder in the film structure due to the decrease in size and/or number of sp^2 clusters and the redistribution on these clusters. The smooth a-C:H underlayers that were treated for a duration of 5 and 10 minutes led to the formation of CN_x nanotips.

Different structures of ns- CN_x were formed as a result of different a-C:H underlayer properties. The nanostructures formed included rigid vertically aligned nanorods and nanotips. Rigid, vertically aligned CN_x nanorods exhibit the highest N incorporation with N/C ratio of 0.2. This indicates that high N incorporation is crucial in the formation of this type of structure. CN_x nanotips show relatively lower N incorporation whereby N in the plasma act as etching agents in the growth process and do not get easily incorporated into the film structure. In general, the chemical bonding of these different ns- CN_x structures show preference of N bonding in the form of nitrile ($-\text{C}\equiv\text{N}$) and isonitrile ($-\text{N}\equiv\text{C}$). From this chemical bonding analysis, the preference of aromatic ring bonded to isonitrile bonds favours the formation of rigid, vertically aligned nanorods of CN_x . Throughout this work, it is proposed that a-C:H underlayer

acts as template or seed layer that helps the formation of nucleation site for ns-CN_x growth.

5.2 Future Works

Due to the introductory nature of this work and constraint in time and resources a number of different aspects in this study were not able to be carried out. Some of these aspects are listed here as suggestion for future works:

- (1) Material characterization particularly on the properties of these ns-CN_x, measurements such as high resolution transmission electron microscopy (HRTEM) and x-ray photo spectroscopy are needed to further identify the nature and crystallinity of these structures.
- (2) Growth progress and mechanism for both the a-C:H underlayer and ns-CN_x that could be done by studying the growth as a function of deposition duration for both layers.
- (3) Exploring different areas of application for the films.
 - (i) CN_x nanotips as scanning probe-tip and electron emitting devices seem high in view of its size and distribution of the growth.
 - (ii) CN_x nanorods as potential material for humidity or gas sensors and hydrogen storage material.

REFERENCES

- Apostol, I., Stefan, N., Luculescu, C. R., Birjega, R., Socol, M., Miroiu, M., & Mihailescu, I. N. (2011). Pulsed laser deposition of semiconducting crystalline double-doped barium titanate thin films on nickel substrates. *Applied Surface Science*, 257(8), 3570-3576.
- Ayala, P., Arenal, R., Rummeli, M., Rubio, A., & Pichler, T. (2010). The doping of carbon nanotubes with nitrogen and their potential applications. *Carbon*, 48(3), 575-586.
- Ayala, P., Grüneis, A., Gemming, T., Büchner, B., Rummeli, M., Grimm, D., Filho, H. D. F. (2007a). Influence of the catalyst hydrogen pretreatment on the growth of vertically aligned nitrogen-doped carbon nanotubes. *Chemistry of Materials*, 19(25), 6131-6137.
- Ayala, P., Grüneis, A., Kramberger, C., Rummeli, M., Solorzano, I., Freire Jr, F., & Pichler, T. (2007b). Effects of the reaction atmosphere composition on the synthesis of single and multiwalled nitrogen-doped nanotubes. *The Journal of Chemical Physics*, 127, 184709.
- Baehr, O., Thevenin, P., Bath, A., Koukab, A., Losson, E., & Lepley, B. (1997). Preparation of boron nitride thin films by microwave plasma enhanced CVD, for semiconductor applications. *Materials Science and Engineering: B*, 46(1), 101-104.
- Bai, X., Cao, C., & Xu, X. (2010). Formation and characterization of flower-like carbon nitride by pyrolysis of melamine. *Materials Science and Engineering: B*, 175(2), 95-99.
- Bai, X., Zhong, D., Zhang, G., Ma, X., Liu, S., Wang, E., Shaw, D. T. (2001). Hydrogen storage in carbon nitride nanobells. *Applied Physics Letters*, 79(10), 1552-1554.
- Banerjee, I., Kumari, N., Singh, A. K., Kumar, M., Laha, P., Panda, A., Mahapatra, S. (2010). Influence of RF power on the electrical and mechanical properties of nano-structured carbon nitride thin films deposited by RF magnetron sputtering. *Thin Solid Films*, 518(24), 7240-7244.
- Brown, B., Parker, C. B., Stoner, B. R., & Glass, J. T. (2011). Growth of vertically aligned bamboo-like carbon nanotubes from ammonia/methane precursors using a platinum catalyst. *Carbon*, 49(1), 266-274.
- Cao, P., Zhu, D., Liu, W., & Ma, X. (2007). The effect of substrate morphology on the diameter distribution of carbon nanotubes grown on silica and ceramic substrates. *Materials Letters*, 61(8), 1899-1903.
- Casiraghi, C., Piazza, F., Ferrari, A. C., Grambole, D., & Robertson, J. (2005). Bonding in hydrogenated diamond-like carbon by Raman spectroscopy. *Diamond and Related Materials*, 14(3-7), 1098-1102.
- Cespedes, J., Corbella, C., Bertran, E., Viera, G., & Galan, M. (2005). Characteristics of Carbon and Carbon-Nitride Nanostructures Produced by Plasma Deposition from Ammonia and Methane or Acetylene. *Fullerenes, Nanotubes, and Carbon Nanostructures*, 13(S1), 447-455.
- Chan, L., Hong, K., Xiao, D., Hsieh, W., Lai, S., Shih, H., Cheng, H. (2003). Role of extrinsic atoms on the morphology and field emission properties of carbon nanotubes. *Applied Physics Letters*, 82, 4334.
- Chan, L. H., Hong, K. H., Xiao, D. Q., Lin, T. C., Lai, S. H., Hsieh, W. J., & Shih, H. C. (2004). Resolution of the binding configuration in nitrogen-doped carbon nanotubes. *Physical Review B*, 70(12), 125408.

- Che, R., Peng, L. M., & Wang, M. (2004). Electron side-emission from corrugated CN nanotubes. *Applied Physics Letters*, 85, 4753.
- Choi, H. C., Bae, S. Y., Jang, W. S., Park, J., Song, H. J., Shin, H. J., Ahn, J. P. (2005). Release of N₂ from the carbon nanotubes via high-temperature annealing. *The Journal of Physical Chemistry B*, 109(5), 1683-1688.
- Choi, W. S., Heo, J., Chung, I., & Hong, B. (2005). The effect of RF power on tribological properties of the diamond-like carbon films. *Thin Solid Films*, 475(1-2), 287-290.
- Chu, P. K., & Li, L. (2006). Characterization of amorphous and nanocrystalline carbon films. *Materials Chemistry and Physics*, 96(2-3), 253-277.
- Cui, S., Scharff, P., Siegmund, C., Schneider, D., Risch, K., Klötzer, S., Schawohl, J. (2004). Investigation on preparation of multiwalled carbon nanotubes by DC arc discharge under N₂ atmosphere. *Carbon*, 42(5-6), 931-939.
- Cuomo, J., Leary, P., Yu, D., Reuter, W., & Frisch, M. (1979). Reactive sputtering of carbon and carbide targets in nitrogen. *Journal of Vacuum Science and Technology*, 16(2), 299-302.
- Dang, C., & Wang, B. (2012). Study on structures and photoluminescence of nitrogenated carbon nanotip arrays synthesized by plasma assisted hot filament chemical vapor deposition. *Applied Surface Science* 258(17), 6692-6698.
- Droppa Jr, R., Hammer, P., Carvalho, A. C. M., dos Santos, M. C., & Alvarez, F. (2002). Incorporation of nitrogen in carbon nanotubes. *Journal of Non-Crystalline Solids*, 299-302, Part 2(0), 874-879.
- Escobar-Alarcón, L., Arrieta, A., Camps, E., Romero, S., & Camacho-Lopez, M. (2005). Infrared and Raman characterization of amorphous carbon nitride thin films prepared by laser ablation. *Superficies y Vacío*, 9-12.
- Fanchini, G., Mandracci, P., Tagliaferro, A., Rodil, S. E., Vomiero, A., & Della Mea, G. (2005). Growth and characterisation of polymeric amorphous carbon and carbon nitride films from propane. *Diamond and Related Materials*, 14(3-7), 928-933.
- Ferrari, A., & Robertson, J. (2000). Interpretation of Raman spectra of disordered and amorphous carbon. *Physical Review B*, 61(20), 14095.
- Ferrari, A., Rodil, S., & Robertson, J. (2003). Interpretation of infrared and Raman spectra of amorphous carbon nitrides. *Physical Review B*, 67(15), 155306.
- Ferrari, A. C. (2007). Raman spectroscopy of graphene and graphite: Disorder, electron-phonon coupling, doping and nonadiabatic effects. *Solid State Communications*, 143(1), 47-57.
- Ganesan, Y., Peng, C., Lu, Y., Ci, L., Srivastava, A., Ajayan, P. M., & Lou, J. (2010). Effect of nitrogen doping on the mechanical properties of carbon nanotubes. *ACS Nano* 4(12), 7637-7643.
- Gielen, J., Kessels, W., Van de Sanden, M., & Schram, D. (1997). Effect of substrate conditions on the plasma beam deposition of amorphous hydrogenated carbon. *Journal of Applied Physics*, 82, 2643.
- Gilkes, K. W. R., Sands, H. S., Batchelder, D. N., Milne, W. I., & Robertson, J. (1998). Direct observation of sp³ bonding in tetrahedral amorphous carbon UV Raman spectroscopy. *Journal of Non-Crystalline Solids*, 227-230, Part 1(0), 612-616.
- Glerup, M., Steinmetz, J., Samaille, D., Stéphan, O., Enouz, S., Loiseau, A., Bernier, P. (2004). Synthesis of N-doped SWNT using the arc-discharge procedure. *Chemical Physics Letters*, 387(1-3), 193-197.
- Gong, K., Du, F., Xia, Z., Durstock, M., & Dai, L. (2009). Nitrogen-doped carbon nanotube arrays with high electrocatalytic activity for oxygen reduction. *Science*, 323(5915), 760.

- He, M., Zhou, S., Zhang, J., Liu, Z., & Robinson, C. (2005). CVD growth of N-doped carbon nanotubes on silicon substrates and its mechanism. *The Journal of Physical Chemistry B*, *109*(19), 9275-9279.
- Honda, S., Lee, K. Y., Fujimoto, K., Tsuji, K., Ohkura, S., Katayama, M., Oura, K. (2002). Formation of carbon nanofiber films by RF magnetron sputtering method. *Physica B: Condensed Matter*, *323*(1-4), 347-349.
- Hopf, C., von Keudell, A., & Jacob, W. (2003). The influence of hydrogen ion bombardment on plasma-assisted hydrocarbon film growth. *Diamond and Related Materials*, *12*(2), 85-89.
- Hu, J., Yang, P., & Lieber, C. M. (1998). Nitrogen driven structural transformation in carbon nitride materials. *Applied Surface Science*, *127*, 569-573.
- Huang, C. J., Chih, Y. K., Hwang, J., Lee, A. P., & Kou, C. S. (2003). Field emission from amorphous-carbon nanotips on copper. *Journal of Applied Physics*, *94*(10), 6796-6799.
- Hung, J.-M., Lin, L.-H., Shih, Y.-H., Liu, C.-M., Cheng, H.-C., & Ou, K.-L. (2011). Research of microstructural characteristics on nanocrystalline diamond by microwave plasma CVD. *Applied Surface Science*, *257*(13), 5508-5512.
- Iijima, S. (1991). Helical microtubules of graphitic carbon. *Nature*, *354*(6348), 56-58.
- Inaba, H., Fujimaki, S., Furusawa, K., & Todoroki, S. (2002). ECR-plasma parameters and properties of thin DLC films. *Vacuum*, *66*(3-4), 487-493.
- Iseki, T. (2009). Target utilization of planar magnetron sputtering using a rotating tilted unbalanced yoke magnet. *Vacuum*, *84*(2), 339-347.
- Ito, H., Nozaki, T., Saikubo, A., Yamada, N., Kanda, K., Niibe, M., & Saitoh, H. (2008). Hydrogen-storage characteristics of hydrogenated amorphous carbon nitrides. *Thin Solid Films*, *516*(19), 6575-6579.
- Jawhari, T., Roid, A., & Casado, J. (1995). Raman spectroscopic characterization of some commercially available carbon black materials. *Carbon*, *33*(11), 1561-1565.
- Jayatissa, A. H., Sato, F., Saito, N., Ohnishi, H., Takizawa, K., Nakanishi, Y., & Yamaguchi, T. (1998). Structural properties of carbon films deposited by pulsed ArF laser ablation: effects of substrate temperature, bias and H₂ pressure. *Materials Science and Engineering: B*, *55*(1), 143-152.
- Jun, C., Ning-sheng, X., En-ge, W., Shao-zhi, D., Di-hu, C., & Ai-xiang, W. (1998). A Study of Field Electron Emission from Thin Amorphous-Carbon-Nitride Films. *Chinese Physics Letters*, *15*, 539.
- Kim, B. K., & Grotjohn, T. A. (2000). Comparison of a-C:H films deposited from methane-argon and acetylene-argon mixtures by electron cyclotron resonance-chemical vapor deposition discharges. *Diamond and Related Materials*, *9*(1), 37-47.
- Kim, J.-P., Noh, Y.-R., Kim, J.-U., & Park, J.-S. (2011). Electron-emission properties of carbon nanotube micro-tips coated by amorphous carbon nitride films. *Thin Solid Films*, *519*(22), 7899-7903.
- Koh, G., Zhang, Y.-W., & Pan, H. (2012). First-principles study on hydrogen storage by graphitic carbon nitride nanotubes. *International Journal of Hydrogen Energy*, *37*(5), 4170-4178.
- Koós, A. A., Dowling, M., Jurkschat, K., Crossley, A., & Grobert, N. (2009). Effect of the experimental parameters on the structure of nitrogen-doped carbon nanotubes produced by aerosol chemical vapour deposition. *Carbon*, *47*(1), 30-37.
- Krstić, V., Rikken, G., Bernier, P., Roth, S., & Glerup, M. (2007). Nitrogen doping of metallic single-walled carbon nanotubes: n-type conduction and dipole scattering. *EPL (Europhysics Letters)*, *77*, 37001.

- Kurt, R., Bonard, J. M., & Karimi, A. (2001a). Morphology and field emission properties of nano-structured nitrogenated carbon films produced by plasma enhanced hot filament CVD. *Carbon*, 39(11), 1723-1730.
- Kurt, R., Bonard, J. M., & Karimi, A. (2001b). Structure and field emission properties of decorated C/N nanotubes tuned by diameter variations. *Thin Solid Films*, 398-399(0), 193-198.
- Lai, S. H., Chen, Y. L., Chan, L. H., Pan, Y. M., Liu, X. W., & Shih, H. C. (2003). The crystalline properties of carbon nitride nanotubes synthesized by electron cyclotron resonance plasma. *Thin Solid Films*, 444(1-2), 38-43.
- Lazar, G., Zellama, K., Vascan, I., Stamate, M., Lazar, I., & Rusu, I. (2005). Infrared absorption properties of amorphous carbon films. *Journal of Optoelectronics and Advanced Materials*, 7(2), 647-652.
- Lee, S. P., Lee, J. G., & Chowdhury, S. (2008). CMOS humidity sensor system using carbon nitride film as sensing materials. *Sensors*, 8(4), 2662-2672.
- Li, J., Cao, C., Hao, J., Qiu, H., Xu, Y., & Zhu, H. (2006). Self-assembled one-dimensional carbon nitride architectures. *Diamond and Related Materials*, 15(10), 1593-1600.
- Lin, C. H., Chang, H. L., Hsu, C. M., Lo, A. Y., & Kuo, C. T. (2003). The role of nitrogen in carbon nanotube formation. *Diamond and Related Materials*, 12(10-11), 1851-1857.
- Liu, A. Y., & Cohen, M. L. (1989). Prediction of new low compressibility solids. *Science*, 245(4920), 841-842.
- Liu, H., Zhang, Y., Li, R., Sun, X., Désilets, S., Abou-Rachid, H., Lussier, L.-S. (2010). Structural and morphological control of aligned nitrogen-doped carbon nanotubes. *Carbon*, 48(5), 1498-1507.
- Liu, J., Webster, S., & Carroll, D. L. (2005). Temperature and flow rate of NH₃ effects on nitrogen content and doping environments of carbon nanotubes grown by injection CVD method. *The Journal of Physical Chemistry B*, 109(33), 15769-15774.
- Liu, X. W., Chan, L., Hong, K., & Shih, H. (2002a). Effect of bias voltage on the formation of aC: N nanostructures in ECR plasmas. *Thin Solid Films*, 420, 212-218.
- Liu, X. W., Lin, C. H., Chao, L. T., & Shih, H. C. (2000). Electron field emission from amorphous carbon nitride nanotips. *Materials Letters*, 44(5), 304-308.
- Liu, X. W., Lin, J. H., Hsieh, W. J., & Shih, H. C. (2002b). Morphology and characterization of highly nitrogenated, aligned, amorphous carbon nano-rods formed on an alumina template by ECR-CVD. *Diamond and Related Materials*, 11(3-6), 1193-1199.
- Lowther, J. (1998). Defective and amorphous structure of carbon nitride. *Physical Review B*, 57(10), 5724.
- Maldonado, S., Morin, S., & Stevenson, K. J. (2006). Structure, composition, and chemical reactivity of carbon nanotubes by selective nitrogen doping. *Carbon*, 44(8), 1429-1437.
- Maldonado, S., & Stevenson, K. J. (2005). Influence of nitrogen doping on oxygen reduction electrocatalysis at carbon nanofiber electrodes. *The Journal of Physical Chemistry B*, 109(10), 4707-4716.
- Marcelli, A., Cricenti, A., Kwiatak, W. M., & Petibois, C. (2012). Biological applications of synchrotron radiation infrared spectromicroscopy. *Biotechnology Advances* doi:/10.1016/j.biotechadv.2012.02.012.
- Marchon, B., Gui, J., Grannen, K., Rauch, G. C., Ager III, J. W., Silva, S., & Robertson, J. (1997). Photoluminescence and Raman spectroscopy in hydrogenated carbon films. *Magnetics, IEEE Transactions on*, 33(5), 3148-3150.

- Meng, X., Zhong, Y., Sun, Y., Banis, M. N., Li, R., & Sun, X. (2011). Nitrogen-doped carbon nanotubes coated by atomic layer deposited SnO₂ with controlled morphology and phase. *Carbon*, 49(4), 1133-1144.
- Meyyappan, M., Delzeit, L., Cassell, A., & Hash, D. (2003). Carbon nanotube growth by PECVD: a review. *Plasma Sources Science and Technology*, 12, 205.
- Miyajima, Y., Henley, S. J., & Silva, S. R. P. (2011). Hydrogenated amorphous carbon and carbon nitride films deposited at low pressure by plasma enhanced chemical vapor deposition. *Thin Solid Films*, 519(19), 6374-6380.
- Moradian, R., & Azadi, S. (2006). Boron and nitrogen-doped single-walled carbon nanotube. *Physica E: Low-dimensional Systems and Nanostructures*, 35(1), 157-160.
- Motta, E. F., & Pereyra, I. (2004). Amorphous hydrogenated carbon-nitride films prepared by RF-PECVD in methane–nitrogen atmospheres. *Journal of Non-Crystalline Solids*, 338-340(0), 525-529.
- Mutsukura, N. (2001). Photoluminescence and infra-red absorption of annealed a-CN_x:H films. *Diamond and Related Materials*, 10(3–7), 1152-1155.
- Mutsukura, N., & Akita, K.-i. (1999). Deposition of hydrogenated amorphous CN_x film in CH₄/N₂ RF discharge. *Diamond and Related Materials*, 8(8-9), 1720-1723.
- Nemanich, R., Glass, J., Lucovsky, G., & Shroder, R. (1988). Raman scattering characterization of carbon bonding in diamond and diamondlike thin films. *Journal of Vacuum Science & Technology A: Vacuum, Surfaces, and Films*, 6(3), 1783-1787.
- Pan, H., Zhang, Y. W., Shenoy, V. B., & Gao, H. (2011a). Ab Initio Study on a Novel Photocatalyst: Functionalized Graphitic Carbon Nitride Nanotube. *ACS Catalysis*, 1, 99-104.
- Pan, H., Zhang, Y. W., Shenoy, V. B., & Gao, H. (2011b). Metal-functionalized single-walled graphitic carbon nitride nanotubes: a first-principles study on magnetic property. *Nanoscale research letters*, 6(1), 1-7.
- Park, Y. S., Myung, H. S., Han, J. G., & Hong, B. (2005). Characterization of CN_x thin films prepared by close field unbalanced magnetron sputtering. *Thin Solid Films*, 475(1), 298-302.
- Pereira, J., Géraud-Grenier, I., Massereau-Guilbaud, V., Plain, A., & Fernandez, V. (2006). Characterization of a-CN_x:H particles and coatings prepared in a CH₄/N₂ r.f. plasma. *Surface and Coatings Technology*, 200(22–23), 6414-6419.
- Pradeep, T., Vijayakrishnan, V., Santra, A., & Rao, C. (1991). Interaction of nitrogen with fullerenes: nitrogen derivatives of C₆₀ and C₇₀. *The Journal of Physical Chemistry*, 95(26), 10564-10565.
- Qu, L., Liu, Y., Baek, J. B., & Dai, L. (2010). Nitrogen-doped graphene as efficient metal-free electrocatalyst for oxygen reduction in fuel cells. *ACS Nano*, 4(3), 1321-1326.
- Ren, Z.-M., Du, Y.-C., Qiu, Y., Wu, J.-D., Ying, Z.-F., Xiong, X.-X., & Li, F.-M. (1995). Carbon nitride films synthesized by combined ion-beam and laser-ablation processing. *Physical Review B*, 51(8), 5274-5277.
- Ritikos, R., Rahman, S. A., Gani, S. M. A., Muhamad, M. R., & Yap, Y. K. (2011). Catalyst-free formation of vertically-aligned carbon nanorods as induced by nitrogen incorporation. *Carbon*, 49(6), 1842-1848.
- Ritikos, R., Siong, C. C., Gani, S. M. A., Muhamad, M. R., & Rahman, S. A. (2009). Effect of annealing on the optical and chemical bonding properties of hydrogenated amorphous carbon and hydrogenated amorphous carbon nitride thin films. *Jpn J Appl Phys*, 48(10), 101301-101301-101304.
- Robertson, J. (2002). Diamond-like amorphous carbon. *Materials Science and Engineering: R: Reports*, 37(4-6), 129-281.

- Rodil, S. (2005). Infrared spectra of amorphous carbon based materials. *Diamond and Related Materials*, 14(8), 1262-1269.
- Sakata, T., Kodama, H., Hayashi, H., Shimo, T., & Suzuki, T. (2010). Effects of substrate temperature on physical properties of amorphous carbon film synthesized under atmospheric pressure. *Surface and Coatings Technology*, 205, Supplement 1(0), S414-S417.
- Sasaki, T., Terauchi, S., Koshizaki, N., & Umehara, H. (1998). The preparation of iron complex oxide nanoparticles by pulsed-laser ablation. *Applied Surface Science*, 127-129(0), 398-402.
- Schwan, J., Ulrich, S., Batori, V., Ehrhardt, H., & Silva, S. (1996). Raman spectroscopy on amorphous carbon films. *Journal of Applied Physics*, 80(1), 440-447.
- Sen, R., Satishkumar, B., Govindaraj, A., Harikumar, K., Renganathan, M., & Rao, C. (1997). Nitrogen-containing carbon nanotubes. *J. Mater. Chem.*, 7(12), 2335-2337.
- Shao, Y., Zhang, S., Engelhard, M. H., Li, G., Shao, G., Wang, Y., Lin, Y. (2010). Nitrogen-doped graphene and its electrochemical applications. *J. Mater. Chem.*, 20(35), 7491-7496.
- Shimoyama, I., Wu, G., Sekiguchi, T., & Baba, Y. (2001). Study of electronic structure of graphite-like carbon nitride. *Journal of Electron Spectroscopy and Related Phenomena*, 114, 841-848.
- Singh, C., Quested, T., Boothroyd, C. B., Thomas, P., Kinloch, I. A., Abou-Kandil, A. I., & Windle, A. H. (2002). Synthesis and characterization of carbon nanofibers produced by the floating catalyst method. *The Journal of Physical Chemistry B*, 106(42), 10915-10922.
- Smietana, M., Bock, W. J., Szmids, J., & Grabarczyk, J. (2010). Substrate effect on the optical properties and thickness of diamond-like carbon films deposited by the RF PACVD method. *Diamond and Related Materials*, 19(12), 1461-1465.
- Srivastava, S. K., Vankar, V., Sridhar Rao, D., & Kumar, V. (2006). Enhanced field emission characteristics of nitrogen-doped carbon nanotube films grown by microwave plasma enhanced chemical vapor deposition process. *Thin Solid Films*, 515(4), 1851-1856.
- Suenaga, K., Johansson, M. P., Hellgren, N., Broitman, E., Wallenberg, L. R., Colliex, C., Hultman, L. (1999). Carbon nitride nanotubulite – densely-packed and well-aligned tubular nanostructures. *Chemical Physics Letters*, 300(5-6), 695-700.
- Suenaga, K., Yudasaka, M., Colliex, C., & Iijima, S. (2000). Radially modulated nitrogen distribution in CN_x nanotubular structures prepared by CVD using Ni phthalocyanine. *Chemical Physics Letters*, 316(5-6), 365-372.
- Sung, C. M., & Sung, M. (1996). Carbon nitride and other speculative superhard materials. *Materials Chemistry and Physics*, 43(1), 1-18.
- Sung, S., Tsai, S., Tseng, C., Chiang, F., Liu, X., & Shih, H. (1999). Well-aligned carbon nitride nanotubes synthesized in anodic alumina by electron cyclotron resonance chemical vapor deposition. *Applied Physics Letters*, 74, 197.
- Tao, X., Zhang, X., Sun, F., Cheng, J., Liu, F., & Luo, Z. (2007). Large-scale CVD synthesis of nitrogen-doped multi-walled carbon nanotubes with controllable nitrogen content on a Co_xMg_{1-x}MoO₄ catalyst. *Diamond and Related Materials*, 16(3), 425-430.
- Theye, M. L., Paret, V., & Sadki, A. (2001). Relations between the deposition conditions, the microstructure and the defects in PECVD hydrogenated amorphous carbon films; influence on the electronic density of states. *Diamond and Related Materials*, 10(2), 182-190.

- Tu, Z., & Ou-Yang, Z. (2002). Single-walled and multiwalled carbon nanotubes viewed as elastic tubes with the effective Young's moduli dependent on layer number. *Physical Review B*, 65(23), 233407.
- von Keudell, A., Meier, M., & Hopf, C. (2002). Growth mechanism of amorphous hydrogenated carbon. *Diamond and Related Materials*, 11(3-6), 969-975.
- Wang, B., Cheng, Q., Wang, L., Zheng, K., & Ostrikov, K. (2012a). The effect of temperature on the mechanism of photoluminescence from plasma-nucleated, nitrogenated carbon nanotips. *Carbon* 50(10), 3561-3571.
- Wang, B., Cheng, Q., Zhong, X., Wang, Y., Chen, Y., & Ostrikov, K. (2012b). Enhanced electron field emission from plasma-nitrogenated carbon nanotips. *Journal of Applied Physics*, 111(4), 044317-044317-044318.
- Wang, B., Dong, G., & Xu, X. (2011). Carbon fractals grown from carbon nanotips by plasma-enhanced hot filament chemical vapor deposition. *Applied Surface Science* 258(5), 1677-1681.
- Wang, B., Lee, S., Yan, H., Gu, C., & Wang, B. (2005). Study on the mechanism of self-organized carbon nanotips without catalyst by plasma-enhanced hot filament chemical vapor deposition. *Applied Surface Science*, 245(1), 21-25.
- Wang, B., & Ostrikov, K. (2009). Tailoring carbon nanotips in the plasma-assisted chemical vapor deposition: Effect of the process parameters. *Journal of Applied Physics*, 105(8), 083303-083303-083309.
- Wang, B., & Zhang, B. (2006). Effects of carbon film roughness on growth of carbon nanotip arrays by plasma-enhanced hot filament chemical vapor deposition. *Carbon*, 44(10), 1949-1953.
- Wang, B., & Zhang, B. (2007). Study on formation model of carbon nanotips by ion bombardment. *Diamond and Related Materials*, 16(11), 1982-1987.
- Wang, C., Yang, S., & Zhang, J. (2008). Correlation between nitrogen incorporation and structural modification of hydrogenated carbon nitride films. *Journal of Non-Crystalline Solids*, 354(15-16), 1608-1614.
- Wang, E. (2002). Carbon nitride-related nanomaterials from chemical vapor deposition: structure and properties. *Journal of the American Ceramic Society*, 85(1), 105-108.
- Wang, E. (2006). Nitrogen-induced carbon nanobells and their properties. *Journal Of Materials Research-Pittsburgh Then Warrendale-*, 21(11), 2767.
- Wang, Y., Shao, Y., Matson, D. W., Li, J., & Lin, Y. (2010). Nitrogen-doped graphene and its application in electrochemical biosensing. *ACS Nano*, 4(4), 1790-1798.
- Yang, L., May, P. W., Huang, Y. Z., & Yin, L. (2007). Hierarchical architecture of self-assembled carbon nitride nanocrystals. *Journal of Materials Chemistry*, 17(13), 1255-1257.
- Yang, L., May, P. W., Yin, L., Brown, R., & Scott, T. B. (2006a). Direct growth of highly organized crystalline carbon nitride from liquid-phase pulsed laser ablation. *Chemistry of Materials*, 18(21), 5058-5064.
- Yang, L., May, P. W., Yin, L., Scott, T. B., Smith, J. A., & Rosser, K. N. (2006b). Growth and characterization of self-assembled carbon nitride leaf-like nanostructures. *Nanotechnology*, 17, 5798.
- Yang, L., May, P. W., Yin, L., Smith, J. A., & Rosser, K. N. (2007). Ultra fine carbon nitride nanocrystals synthesized by laser ablation in liquid solution. *Journal of Nanoparticle Research*, 9(6), 1181-1185.
- Yi, J.-Y., & Bernholc, J. (1993). Atomic structure and doping of microtubules. *Physical Review B*, 47(3), 1708-1711.
- Yu, G.-Q., Lee, S.-H., & Lee, J.-J. (2002). Effects of thermal annealing on amorphous carbon nitride films by r.f. PECVD. *Diamond and Related Materials*, 11(9), 1633-1637.

- Yu, R., Zhan, M., Cheng, D., Yang, S., Liu, Z., & Zheng, L. (1995). Simultaneous Synthesis of Carbon Nanotubes and Nitrogen-Doped Fullerenes in Nitrogen Atmosphere. *The Journal of Physical Chemistry*, 99(7), 1818-1819.
- Zambov, L., Popov, C., Abedinov, N., Plass, M., Kulisch, W., Gotszalk, T., Kassing, R. (2000). Gas-Sensitive Properties of Nitrogen-Rich Carbon Nitride Films. *Advanced Materials*, 12(9), 656-660.
- Zhang, G., Ma, X., Zhong, D., & Wang, E. (2002). Polymerized carbon nitride nanobells. *Journal of Applied Physics*, 91, 9324.
- Zhao, G. M., Yang, Y. Q., Zhang, W., Luo, X., Zhang, R. J., & Chen, Y. (2011). Raman scattering characterization of a carbon coating after low-energy argon ion bombardment. *Physica B: Condensed Matter*, 406(20), 3876-3884.
- Zhong, D., Liu, S., Zhang, G., & Wang, E. (2001). Large-scale well aligned carbon nitride nanotube films: Low temperature growth and electron field emission. *Journal of Applied Physics*, 89, 5939.
- Zhong, D., Zhang, G., Liu, S., Wang, E., Wang, Q., Li, H., & Huang, X. (2001). Lithium storage in polymerized carbon nitride nanobells. *Applied Physics Letters*, 79, 3500.
- Zimmerman, J. L., Williams, R., Khabashesku, V. N., & Margrave, J. L. (2001). Synthesis of spherical carbon nitride nanostructures. *Nano Letters*, 1(12), 731-734.